A 2.4% Determination of the Local Value of the Hubble Constant[1]

Adam G. Riess[2,3], Lucas M. Macri[4], Samantha L. Hoffmann[4], Dan Scolnic[2,5], Stefano Casertano[3], Alexei V. Filippenko[6], Brad E. Tucker[6,7], Mark J. Reid[8], David O. Jones[2], Jeffrey M. Silverman[9], Ryan Chornock[10], Peter Challis[8], Wenlong Yuan[4], and Ryan J. Foley[11,12]

ABSTRACT

We use the Wide Field Camera 3 (WFC3) on the *Hubble Space Telescope (HST)* to reduce the uncertainty in the local value of the Hubble constant from 3.3% to 2.4%. The bulk of this improvement comes from observations of Cepheid variables in 10 new host galaxies of recent type Ia supernovae (SNe Ia), more than doubling the sample of SNe Ia having a Cepheid-calibrated distance to a total of 18; these in turn leverage the magnitude-redshift relation based on 300 SNe Ia at $z < 0.15$. All 18 hosts as well as the megamaser system NGC 4258 have been observed with WFC3 in the optical and near-infrared, thus nullifying cross-instrument zeropoint errors in the relative distance estimates from Cepheids. Other noteworthy improvements include a 33% reduction in the systematic uncertainty in the maser distance to NGC 4258, a larger sample of Cepheids in the Large Magellanic Cloud (LMC), a more robust distance to the LMC

based on late-type detached eclipsing binaries (DEBs), *HST* observations of Cepheids in M31, and new *HST*-based trigonometric parallaxes for Milky Way (MW) Cepheids.

We consider four geometric distance calibrations of Cepheids: (i) megamasers in NGC 4258, (ii) 8 DEBs in the LMC, (iii) 15 MW Cepheids with parallaxes measured with *HST*/FGS, *HST*/WFC3 spatial scanning and/or *Hipparcos*, and (iv) 2 DEBs in M31. The Hubble constant from each is 72.39±2.56, 71.93±2.70, 76.09±2.41, and 74.45±3.34 km s^{-1} Mpc^{-1}, respectively. Our best estimate of H$_0$ = 73.02±1.79 km s^{-1} Mpc^{-1} combines the anchors NGC 4258, MW, and LMC, and includes systematic errors for a final uncertainty of 2.4%. This value is 3.0σ higher than 67.3 ± 0.7 km s^{-1} Mpc^{-1} predicted by ΛCDM with 3 neutrino flavors having a mass of 0.06 eV and the *Planck* data, but the discrepancy reduces to 2.0σ relative to the prediction of 69.3 ± 0.7 km s^{-1} Mpc^{-1} based on the comparably precise combination of *WMAP*+ACT+SPT+BAO observations, suggesting that systematic uncertainties in cosmic microwave background radiation measurements may play a role in the tension.

If we take the conflict between *Planck* high-redshift measurements and our local determination of H$_0$ at face value, one plausible explanation could involve an additional source of dark radiation in the early Universe in the range of $\Delta N_{\text{eff}} \approx 0.4 - 1$. We anticipate further significant improvements in H$_0$ from upcoming parallax measurements of long-period MW Cepheids.

Subject headings: galaxies: distances and redshifts — cosmology: observations — cosmology: distance scale — supernovae: general — stars: variables: Cepheids

1. Introduction

The Hubble constant (H$_0$) measured locally and the sound horizon observed from the cosmic microwave background radiation (CMB) provide two absolute scales at opposite ends of the visible expansion history of the Universe. Comparing the two gives a stringent test of the standard cosmological model. A significant disagreement would provide evidence for fundamental physics beyond the standard model, such as time-dependent or early dark energy, gravitational physics beyond General Relativity, additional relativistic particles, or nonzero curvature. Indeed, none of these features has been excluded by anything more compelling than a theoretical preference for simplicity over complexity. In the case of dark energy, there is no simple explanation at present, leaving direct measurements as the only guide among numerous complex or highly tuned explanations.

Recent progress in measuring the CMB from *WMAP* (Hinshaw et al. 2013; Bennett et al. 2013) and *Planck* (Planck Collaboration et al. 2015) have reduced the uncertainty in the distance to the surface of last scattering ($z \sim 1000$) to below 0.5% in the context of ΛCDM, motivating complementary efforts to improve the local determination of H$_0$ to percent-level precision (Suyu et al. 2012; Hu 2005). Hints of mild tension at the $\sim 2-2.5\sigma$ level with the 3−5% measurements of H$_0$ by

Riess et al. (2011), Sorce et al. (2012), Freedman et al. (2012), and Suyu et al. (2013) have been widely considered and in some cases revisited in great detail (Efstathiou 2014; Dvorkin et al. 2014; Bennett et al. 2014; Spergel et al. 2015; Becker et al. 2015), with no definitive conclusion except for highlighting the value of improvements in the local observational determination of H_0.

1.1. Past Endeavors

Considerable progress in the local determination of H_0 has been made in the last 25 years, assisted by observations of water masers, strong-lensing systems, SNe, the Cepheid period-luminosity (P–L) relation (also known as the Leavitt law; Leavitt & Pickering 1912), and other sources used independently or in concert to construct distance ladders (see Freedman & Madore 2010; Livio & Riess 2013, for recent reviews).

A leading approach utilizes *Hubble Space Telescope (HST)* observations of Cepheids in the hosts of recent, nearby SNe Ia to link geometric distance measurements to other SNe Ia in the expanding Universe. The SN Ia *HST* Calibration Program (Sandage et al. 2006) and the *HST* Key Project (Freedman et al. 2001) both made use of *HST* observations with WFPC2 to resolve Cepheids in SN Ia hosts. However, the useful range of that camera for measuring Cepheids, $\lesssim 25$ Mpc, placed severe limits on the number and choice of SNe Ia which could be used to calibrate their luminosity (e.g., SNe 1937C, 1960F, 1974G). A dominant systematic uncertainty resulted from the unreliability of those nearby SNe Ia which were *photographically* observed, highly reddened, spectroscopically abnormal, or discovered after peak brightness. Only three objects (SNe 1990N, 1981B, and 1998aq) used by Freedman et al. (2001, 2012) and four by Sandage et al. (2006) (the above plus SN 1994ae) were free from these shortcomings, leaving a very small set of reliable calibrators relative to the many hundreds of similarly reliable SNe Ia observed in the Hubble flow. The resulting ladders were further limited by the need to flux-calibrate WFPC2 to the ground-based systems used to measure Cepheids in a single anchor, the Large Magellanic Cloud (LMC). The use of LMC Cepheids introduces additional systematic uncertainties because of their shorter mean period ($\Delta \langle \log P \rangle \approx 0.7$ dex) and lower metallicity ($\Delta \log(\mathrm{O/H}) = -0.25$ dex, Romaniello et al. 2008) than those found with *HST* in the large spiral galaxies that host nearby SNe Ia. Despite careful work, the estimates of H_0 by the two teams (each with 10% uncertainty) differed by 20%, owing in part to the aforementioned systematic errors.

More recently, the SH0ES (Supernovae, H_0, for the Equation of State of dark energy) team used a number of advancements to refine this approach to determining H_0. Upgrades to the instrumentation of *HST* doubled its useful range for resolving Cepheids (leading to an eight-fold improvement in volume and in the expected number of useful SN Ia hosts), first with the Advanced Camera for Surveys (ACS; Riess et al. 2005, 2009b) and later with the Wide Field Camera 3 (WFC3; Riess et al. 2011, hereafter R11) owing to the greater area, higher sensitivity, and smaller pixels of these cameras. WFC3 has other superior features for Cepheid reconnaissance, including a white-light filter (*F350LP*) that more than doubles the speed for discovering Cepheids and measur-

ing their periods relative to the traditional $F555W$ filter, and a 5 square arcmin near-infrared (NIR) detector that can be used to reduce the impact of differential extinction and metallicity differences across the Cepheid sample. A precise geometric distance to NGC 4258 measured to 3% using water masers (Humphreys et al. 2013, hereafter H13) has provided a new anchor galaxy whose Cepheids can be observed *with the same instrument and filters* as those in SN Ia hosts to effectively cancel the effect of photometric zeropoint uncertainties in this step along the distance ladder. Tied to the Hubble diagram of 240 SNe Ia (now > 300 SNe Ia (Scolnic et al. 2015; Scolnic & Kessler 2016)), the new ladder was used to initially determine H_0 with a total uncertainty of 4.7% (Riess et al. 2009a, hereafter R09). R11 subsequently improved this measurement to 3.3% by increasing to 8 the number of Cepheid distances to SN Ia hosts, and formally including HST/FGS trigonometric parallaxes of 10 Milky Way (MW) Cepheids with distance $D < 0.5$ kpc and individual precision of 8% (Benedict et al. 2007). The evolution of the error budget in these measurements is shown in Figure 1.

Here we present a broad set of improvements to the SH0ES team distance ladder including HST observations of Cepheids in 10 new SN Ia hosts (bringing the total to 18), a refined computation of the distance to NGC 4258 from maser data, additional Cepheid parallax measurements, larger Cepheid samples in the anchor galaxies, and additional SNe Ia to constrain the Hubble flow. We present the new Cepheid data in §2 and in Hoffmann et al. (in prep.; hereafter H16). Other improvements are described throughout §3, and a consideration of analysis variants and systematic uncertainties is given in §4. We end with a discussion in §5.

2. HST Observations of Cepheids in the SH0ES Program

Discovering and measuring Cepheid variables in SN Ia host galaxies requires a significant investment of observing time on HST, a facility that has long been heavily oversubscribed. It is thus important to select SN Ia hosts likely to produce a set of calibrators that is a good facsimile of the much larger sample defining the modern SN Ia magnitude-redshift relation at $0.01 < z < 0.15$ (e.g., Scolnic et al. 2015; Scolnic & Kessler 2016). Poor-quality light curves, large reddening, atypical SN explosions, or hosts unlikely to yield a significant number of Cepheids would all limit contributions to this effort. Therefore, the SH0ES program has been selecting SNe Ia with the following qualities to ensure a reliable calibration of their fiducial luminosity: (1) modern photometric data (i.e., photoelectric or CCD), (2) observed before maximum brightness and well thereafter, (3) low reddening (implying $A_V < 0.5$ mag), (4) spectroscopically typical, and (5) a strong likelihood of being able to detect Cepheids in its host galaxy with HST. This last quality translates into any late-type host (with features consistent with the morphological classification of Sa to Sd) having an expectation of $D \lesssim 40$ Mpc, inclination $< 75°$, and apparent size $> 1'$. To avoid a possible selection bias in SN Ia luminosities, the probable distance of the host is estimated via the Tully-Fisher relation or

flow-corrected redshifts as reported in NED[1]. We will consider the impact of these selections in §4.

The occurrence of SNe Ia with these characteristics is unfortunately quite rare, leading to a fairly complete sample of 18 objects observed between 1993 and 2013 (see Table 1). Excluding supernovae from the 1980s, a period when modern detectors were rare and when suitable SNe Ia may have appeared and gone unnoticed, the average rate of production is $\sim 0.5 - 1$/year. Regrettably, it will be difficult to increase this sample substantially (by a factor of ~ 2) over the remaining lifetime of *HST*. We estimate that a modest augmentation of the sample (at best) would occur by removing one or more of the above selection criteria, but the consequent increase in systematic uncertainty would more than offset the statistical gain.

Reliable SNe Ia from early-type hosts could augment the sample, with distance estimates based on RR Lyrae stars or the tip of the red-giant branch (TRGB) for their calibration. Unfortunately, the reduced distance range of these distance indicators for *HST* compared to Cepheids (2.5 mag or $D < 13$ Mpc for TRGB, 5 mag or $D < 4$ Mpc for RR Lyrae stars) and the factor of ~ 5 smaller sample of SNe Ia in early-type hosts limits the sample increase to just a few additional objects (SN 1992A, SN 1994D, and SN 1980N), a small fraction of the current sample of 18 SNe Ia calibrated by Cepheids.

Figure 2 shows the sources of the *HST* data obtained on every host we use, gathered from different cameras, filters, and time periods. All of these publicly available data can be readily obtained from the Mikulski Archive for Space Telescopes (MAST; see Table 1). The utility of the imaging data can be divided into two basic functions: Cepheid discovery and flux measurement. For the former, a campaign using a filter with central wavelength in the visual band and ~ 12 epochs with nonredundant spacings spanning ~ 60–90 days will suffice to identify Cepheid variables by their unique light curves and accurately measure their periods (Madore & Freedman 1991; Saha et al. 1996; Stetson 1996). Revisits on a year timescale, although not required, will yield increased phasing accuracy for the longest-period Cepheids. Image subtraction can be very effective for finding larger samples of variables (Bonanos & Stanek 2003), but the additional objects will be subject to greater photometric biases owing to blends which suppress their amplitudes and chances of discovery in time-series data (Ferrarese et al. 2000).

Flux measurements are required in order to use Cepheids as standard candles for distance measurement and are commonly done with *HST* filters at known phases in optical ($F555W$, $F814W$) and NIR ($F160W$) bands to correct for the effects of interstellar dust and the nonzero width in temperature of the Cepheid instability strip. We rely primarily on NIR "Wesenheit" magnitudes (Madore 1982), defined as

$$m_H^W = m_H - R\,(V - I), \tag{1}$$

where $H = F160W$, $V = F555W$, $I = F814W$ in the *HST* system, and $R \equiv A_H/(A_V - A_I)$. We

---

note that the value of R due to the correlation between Cepheid intrinsic color and luminosity is very similar to that due to extinction (Macri et al. 2015), so the value of R derived for the latter effectively also reduces the intrinsic scatter caused by the breadth of the instability strip. However, to avoid a distance bias, we include only Cepheids with periods above the completeness limit of detection in our primary fit. (In future work we will use simulations to account for the bias of Cepheids below this limit to provide an extension of the Cepheid sample.)

In *HST* observations, Cepheid distances based on NIR measurements have somewhat higher statistical uncertainties than those solely based on optical photometry owing to the smaller field of view, lower spatial resolution, and greater blending from red giants. However, as characterized in §4.2, this is more than offset by increased robustness to systematic uncertainties (such as metallicity effects and possible breaks in the slope of the P–L relation) as well as the reduced impact of extinction and a lower sensitivity to uncertainties in the reddening law. The latter is quantified by the value of R in Equation 1, ranging from 0.3 to 0.5 at H depending on the reddening law, a factor of ~ 4 lower than the value at I. At the high end, the Cardelli et al. (1989) formulation with $R_V = 3.3$ yields $R = 0.47$. The Fitzpatrick (1999) formulation with $R_V = 3.3$ and 2.5 yields $R = 0.39$ and $R = 0.35$, respectively. At the low end, a formulation appropriate for the inner Milky Way (Nataf et al. 2015) yields $R = 0.31$. We analyze the sensitivity of H_0 to variations in R in §4.

2.1. Cepheid Photometry

The procedure for identifying Cepheids from time-series optical data (see Table 1 and Figure 2) has been described extensively (Saha et al. 1996; Stetson 1996; Riess et al. 2005; Macri et al. 2006); details of the procedures followed for this sample are presented by H16, utilize the DAO suite of software tools for crowded-field PSF photometry, and are similar to those used previously by the SH0ES team. The complete sample of Cepheids discovered or reanalyzed by H16 in these galaxies (NGC 4258 and the 18 SN Ia hosts) contains > 2400 variables, of which ~ 2000 are above the periods for optical completeness across the instability strip (with limits estimated using the *HST* exposure-time calculators and empirical tests). There are > 1300 such Cepheids in the 18 SN Ia hosts and in the smaller WFC3-IR fields alone. The positions of the Cepheids within each target galaxy are shown in Figure 3. For hosts in which we used $F350LP$ to identify Cepheid light curves, additional photometry was obtained over a few epochs in $F555W$ and $F814W$. These data were phase-corrected to mean-light values using empirical relations based on light curves in both $F555W$ and $F350LP$ from Cepheids in NGC 5584. Figure 4 shows composite Cepheid light curves in $F350LP/F555W$ for each galaxy. Despite limited sampling of the individual light curves, the composites clearly display the characteristic "saw-toothed" light curves of Population I fundamental-mode Cepheids, with a rise twice as fast as the decline and similar mean amplitudes across all hosts.

For every host, optical data in $F555W$ and $F814W$ from WFC3 were uniformly calibrated using the latest reference files from STScI and aperture corrections derived from isolated stars in

Table 1. Cepheid Hosts Observed with *HST*/WFC3

Galaxy	SN Ia	Exp. time (s) NIR[a]	Opt.[b]	Prop IDs	UT Date
M101[c]	2011fe	4847	3776	12880	2013-03-03
N1015	2009ig	14364	39336	12880	2013-06-30
N1309[c]	2002fk	6991	3002	11570,12880	2010-07-24
N1365[c]	2012fr	3618	3180	12880	2013-08-06
N1448	2001el	6035	17562	12880	2013-09-01
N3021[c]	1995al	4426	2962	11570,12880	2010-06-03
N3370[c]	1994ae	4376	2982	11570,12880	2010-04-04
N3447	2012ht	4529	19114	12880	2013-11-30
N3972	2011by	6635	19932	13647	2015-04-19
N3982[c]	1998aq	4018	1400	11570	2009-08-04
N4038[c]	2007sr	6795	2064	11577	2010-01-22
N4258[c]	Anchor	34199	6120	11570	2009-12-20
N4424	2012cg	3623	17782	12880	2013-12-24
N4536[c]	1981B	2565	2600	11570	2010-07-19
N4639[c]	1990N	5379	1600	11570	2009-08-07
N5584	2007af	4929	59940	11570	2010-03-30
N5917	2005cf	7235	23469	12880	2013-05-20
N7250	2013dy	5435	18158	12880	2013-11-08
U9391	2003du	13711	39336	12880	2012-12-14

Note. — (a) Data obtained with WFC3/IR and $F160W$. (b) Data obtained with WFC3/UVIS and $F555W$, $F814W$, or $F350LP$ used to find and measure the flux of Cepheids. (c) Includes time-series data from an earlier program and a different camera — see Fig. 2.

deep images to provide uniform flux measurements for all Cepheids. In a few cases, $F555W$ and $F814W$ data from ACS and WFC3 were used in concert with their well-defined cross-calibration to obtain photometry with a higher signal-to-noise ratio (S/N). The cross-calibration between these two cameras has been stable to < 0.01 mag over their respective lifetimes.

As in R11, we calculated the positions of Cepheids in the WFC3 $F160W$ images using a geometric transformation derived from the optical images using bright and isolated stars, with resulting mean position uncertainties for the variables < 0.03 pix. We used the same scene-modeling approach to $F160W$ NIR photometry developed in R09 and R11. The procedure is to build a model of the Cepheid and sources in its vicinity using the superposition of point-spread functions (PSFs). *The position of the Cepheid is fixed at its predicted location to avoid measurement bias.* We model and subtract a single PSF at that location and then produce a list of all unresolved sources within 50 pixels. A scene model is constructed with three parameters per source (x, y, and flux), one for the preliminary Cepheid (flux) and a local sky level in the absence of blending; the best-fit parameters are determined simultaneously using a Levenberg-Marquardt-based algorithm. Example NIR scene models for each of the 18 SN Ia hosts are shown in Figure 5.

Care must be taken when measuring photometry of visible stellar sources in crowded regions as source blending can alter the statistics of the Cepheid background (Stetson 1987). Typically the mean flux of pixels in an annulus around the Cepheid is subtracted from the measured flux at the position of the Cepheid to produce unbiased photometry of the Cepheid. This mean background or sky would include unresolved sources and diffuse background. However, we can improve the precision of Cepheid photometry by correctly attributing some flux to the other sources in the scene especially those visibly overlapping with the Cepheid. The consequence of differentiating the mean sky into individual source contributions plus a lower constant sky level is that the new sky level will underestimate the true mix of unresolved sources and diffuse background superimposed with the Cepheid flux (in sparse regions without blending, the original and new sky levels would approach the same value). This effect may usefully be called the sky bias or the photometric difference due to blending and is statistically easily rectified. To retrieve the unbiased Cepheid photometry from the result of the scene model we could either recalculate the Cepheid photometry using the original mean sky or correct the overestimate of Cepheid flux based on the measured photometry of artificial stars added to the scenes. The advantage of the artificial star approach is that the same analysis also produces an empirical error estimate and can provide an estimate of outlier frequency.

Following this approach, we measure the mean difference between input and recovered photometry of artificial Cepheids added to the local scenes in the $F160W$ images and fit with the same algorithms. As in R09 and R11, we added and fitted 100 artificial stars placed at random positions within 5 arcseconds of (but not coincident with) each Cepheid to measure and account for this difference. To avoid a bias in this procedure, we initially estimate the input flux for the artificial stars from the Cepheid period and an assumed P–L relation (iteratively determined), measure the difference caused by blending, refine the P–L relation, and iterate until convergence. Additionally,

we use the offset in the predicted and measured location of the Cepheid, a visible consequence of blending, to select similarly affected artificial stars to customize the difference measurements for each Cepheid. The median difference for the Cepheids in all hosts observed with HST is 0.17 mag, mostly due to red-giant blends, and it approaches zero for Cepheids in lower-density regions such as the outskirts of hosts. The Cepheid photometry presented in this paper already includes blending corrections. We also estimate the uncertainty in the Cepheid flux from the dispersion of the measured artificial-star photometry around the 2.7σ-clipped mean. The NIR Cepheid P–L relations for all hosts and anchors are shown in Figure 6.

Likewise, in the optical images, we used as many as 200 measurements of randomly placed stars in the vicinity of each Cepheid in $F555W$ and $F814W$ images to measure and account for the photometric difference due to the process of estimating the sky in the presence of blending. Only 10 stars were added to each simulated image to avoid increasing the stellar density. These tests show that similarly to the NIR measurements, uncertainty in the Cepheid background are the leading source of scatter in the observed P–L relations of the SN hosts. The mean dispersions at $F555W$ and $F814W$ are 0.19 and 0.17 mag, respectively. All SN hosts and NGC 4258 display some difference in their optical magnitudes due to blending, with mean values of 0.07 and 0.06 mag (bright) in $F555W$ and $F814W$, respectively. The most crowded case (0.32 and 0.26 mag) is NGC 4424, a galaxy whose Cepheids are located in a circumnuclear starburst region with prominent dust lanes. We tabulate the mean photometric differences due to blending for each host in Table 2. However, the effect of blending largely cancels when determining the color $F555W - F814W$ used to measure Cepheid distances via equation (1) since the blending is highly correlated across these bands. Indeed, the estimated change in color across all hosts has a mean of only 0.005 mag (blue) and a scatter of 0.01 mag, implying no statistically significant difference from the initial measurement and thus we have not applied these to the optical magnitudes in Table 4. Even the additional scatter in the m_H^W P–L relation owing to blending in the optical color measurement is a relatively minor contribution of 0.07 mag. The small correction due to blending in the optical bands does need to be accounted for when using a conventional *optical* Wesenheit magnitude, $m_I^W = F814W - R_I(F555W - F814W)$, because (unlike the color) the cancellation in m_I^W is not complete. We find a small mean difference for m_I^W in our SN hosts of 0.025 mag (bright) with a host-to-host dispersion in this quantity of 0.03 mag. If uncorrected, this would lead to a 1% underestimate of distances and an overestimate of H_0 for studies that rely exclusively on m_I^W. The more symmetric effect of blending on m_I^W than m_H^W magnitudes results from the mixture of blue blends (which make m_I^W faint) and red blends (which make m_I^W bright). These results are consistent with those found from simulations by Ferrarese et al. (2000), who drew similar conclusions. We will make use of these results for m_I^W in §4.2. Although the net effect of blending for m_I^W is typically small, the uncertainty it produces is the dominant source of dispersion with a mean of 0.36 mag for the SN hosts, similar in impact and scatter to what was found for m_H^W.

Although we quantify and propagate the individual measurement uncertainty for each Cepheid, we conservatively discard the lowest-quality measurements. As in R11, scene models of Cepheids

Table 2.   Artificial Cepheid Tests in Optical Images

Host	ΔV	ΔI	Δct	Δm_I^W	$\sigma(V)$	$\sigma(I)$	$\sigma(ct)$	$\sigma(m_I^W)$
			[mmag]				[mag]	
M101	6	3	1	-2	0.09	0.09	0.03	0.16
N1015	41	40	1	27	0.13	0.13	0.06	0.31
N1309	105	63	12	-1	0.35	0.26	0.10	0.48
N1365	15	19	0	7	0.13	0.13	0.06	0.29
N1448	31	24	1	6	0.14	0.13	0.06	0.29
N3021	106	134	0	75	0.23	0.22	0.09	0.46
N3370	69	55	5	26	0.23	0.19	0.07	0.37
N3447	34	23	4	-1	0.14	0.12	0.06	0.29
N3972	79	68	7	25	0.18	0.17	0.07	0.38
N3982	82	69	0	22	0.22	0.19	0.09	0.44
N4038	38	28	2	12	0.19	0.15	0.07	0.34
N4258I	5	7	-1	10	0.20	0.23	0.05	0.36
N4258O	-2	1	0	0	0.08	0.07	0.02	0.10
N4424	318	262	-2	111	0.31	0.28	0.11	0.58
N4536	12	16	-1	10	0.11	0.10	0.05	0.24
N4639	56	85	-5	89	0.21	0.22	0.09	0.51
N5584	26	23	2	7	0.15	0.13	0.05	0.26
N5917	54	51	-2	32	0.20	0.19	0.08	0.42
N7250	152	91	13	-1	0.24	0.20	0.08	0.42
U9391	36	42	-3	38	0.15	0.15	0.06	0.34

Note. — $V = F555W$; $I = F814W$; $ct = 0.4 \times (F555W - F814W)$.

Table 3.   Properties of NIR P–L Relations

Galaxy	Number in FoV	Number meas.[b]	Number Fit[a]	$\langle P \rangle$ (days)	ΔT (days)
LMC	. . .	798	785	6.6	100
MW	. . .	15	15	8.5	100
M31	. . .	375	372	11.5	0
M101	392	295	274	17.0	0
N1015	27	14	14	59.8	100
N1309	64	45	44	55.2	0
N1365	73	38	32	33.6	12
N1448	85	60	54	30.9	54
N3021	36	18	18	32.8	0
N3370	86	65	63	42.1	0
N3447	120	86	80	34.5	59
N3972	71	42	41	31.5	38
N3982	22	16	16	40.6	0
N4038	28	13	12	63.4	0
N4258	228	141	139	18.8	0
N4424	8	4	3	28.9	33
N4536	47	35	34	36.5	0
N4639	35	26	25	40.4	0
N5584	128	85	83	42.6	11
N5917	21	14	13	39.8	100
N7250	39	22	22	31.3	60
U9391	36	29	28	42.2	100
Total SN	1318	907	856	31.9	. . .
Total All	. . .	2223	2180	. . .	. . .

Note. — (a) After outlier rejection.

Note. — (b) Good quality measurement, within allowed color range, period above completeness limit

Table 4.   WFC3-IR Cepheids

Field	α	δ	ID	P	$V-I$	H	$\sigma_{\rm tot}$	Z	Note
	(deg, J2000)		(mag)	(days)		(mag)		(dex)	
N3021	147.75000	33.547100	64252	16.17	0.92	25.71	0.576	8.831	
N3021	147.74200	33.558399	97590	18.23	1.00	25.05	0.535	8.972	
N3021	147.73700	33.560101	114118	20.60	1.13	26.79	0.581	8.929	
N3021	147.74699	33.556599	80760	21.01	1.16	25.79	0.595	8.914	
N3021	147.72099	33.555099	155661	22.98	0.98	25.64	0.285	8.665	
N3021	147.72701	33.556099	143080	23.94	1.22	25.30	0.457	8.968	
N3021	147.73199	33.548801	124526	26.78	1.19	25.48	0.364	8.875	
N3021	147.73300	33.552299	122365	31.09	0.93	25.57	0.524	9.196	
N3021	147.74800	33.550301	74434	31.67	0.86	24.54	0.495	9.044	
N3021	147.74600	33.556000	85103	33.25	1.54	25.27	0.761	9.022	
N3021	147.73700	33.559299	114576	33.17	1.06	24.82	0.307	9.006	
N3021	147.73300	33.560200	127220	35.31	1.50	25.64	0.307	8.944	
N3021	147.72800	33.558899	141178	36.37	1.27	25.34	0.296	8.936	
N3021	147.73399	33.551498	120418	35.33	0.84	25.23	0.431	9.165	
N3021	147.73199	33.548901	123439	39.41	1.19	25.02	0.309	8.895	
N3021	147.75000	33.550499	67964	39.83	1.24	26.07	0.430	8.963	
N3021	147.75200	33.549599	59565	44.28	0.58	25.06	0.235	8.869	
N3021	147.73900	33.558102	107249	56.24	1.31	24.64	0.528	9.088	
N3021	147.75101	33.554100	65081	58.07	0.90	24.30	0.242	8.842	
N3370	161.76199	17.287600	42916	24.06	1.38	24.83	0.428	8.776	
N3370	161.75900	17.280100	40625	24.07	1.12	25.67	0.564	8.929	
N3370	161.78700	17.260000	170179	24.62	1.04	25.44	0.244	8.446	
N3370	161.76100	17.260500	77247	24.88	1.04	25.39	0.223	8.596	
N3370	161.77000	17.278500	2053060	25.37	0.83	25.10	0.661	8.959	
N3370	161.77600	17.259600	140127	25.40	1.40	24.53	0.382	8.781	
N3370	161.76100	17.262300	75776	26.39	1.25	25.19	0.270	8.673	
N3370	161.76801	17.287201	65151	26.62	1.19	25.69	0.318	8.709	
N3370	161.75999	17.268101	60692	26.66	1.20	25.22	0.452	8.798	
N3370	161.78200	17.272699	144079	26.81	1.20	25.46	0.294	8.565	
N3370	161.78101	17.257200	157064	28.48	1.23	25.04	0.279	8.630	
N3370	161.76601	17.285801	58859	28.98	1.31	25.08	0.334	8.808	
N3370	161.78101	17.273701	138531	29.51	1.03	25.65	0.242	8.606	
N3370	161.76801	17.280800	77712	30.03	1.09	24.54	0.530	8.943	
N3370	161.75800	17.280199	36935	30.13	0.98	25.28	0.548	8.894	
N3370	161.78300	17.271900	147636	30.31	1.42	24.98	0.213	8.542	
N3370	161.75600	17.280500	30963	30.38	1.25	25.34	0.377	8.837	
N3370	161.75200	17.285801	10141	31.20	1.34	24.73	0.333	8.635	
N3370	161.76700	17.282400	71353	31.31	1.18	25.04	0.541	8.905	
N3370	161.75800	17.288900	26623	31.37	1.04	25.47	0.242	8.720	
N3370	161.77200	17.284000	85290	31.46	1.15	25.34	0.255	8.713	
N3370	161.76100	17.268600	66128	32.79	1.25	24.56	0.364	8.887	
N3370	161.76801	17.281000	74164	34.06	1.19	24.16	0.590	8.956	
N3370	161.76199	17.278700	54733	34.34	0.90	24.59	0.694	9.048	

Note. — $V-I$ stands for $F555W-F814W$ and H stands for $F160W$. $Z = 12 + log(O/H)$

were considered to be useful if our software reported a fitted magnitude for the source with an uncertainty < 0.7 mag, a set of model residual pixels with root-mean square (rms) better than 3σ from the other Cepheid scenes, and a measured difference from the artificial star analyses of < 1.5 mag. In addition, we used a broad (1.2 mag) allowed range of $F814W{-}F160W$ colors centered around the median for each host, similar to the $V{-}I$ color selection common to optical studies (see H16), to remove any Cepheids strongly blended with redder or bluer stars of comparable brightness. As simulations in §4.1 show, most of these result from red giants but also occasionally from blue supergiants.

Of the more than 1300 Cepheids in the SN Ia hosts with periods above the completeness limit, just over 900 yielded a good quality photometric measurement and in the allowed color range in the $F160W$ images, with excessive blending in the vicinity of a Cepheid in lower-resolution and lower-contrast NIR images as the leading cause for the failure to derive a useful measurement for the others. The number of Cepheids available at each step in the measurement process is given in Table 3.

2.2. Statistical Uncertainties in Cepheid Distances

We now quantify the statistical uncertainties that apply to Cepheid-based distance estimates. As described in the previous section, the largest source of measurement uncertainty arises from fluctuations in the sky background due to variations in blending, and it is measured from artificial star tests; we refer to this as $\sigma_{\rm sky}$. For SN Ia hosts at 20–40 Mpc and for NGC 4258, the mean $\sigma_{\rm sky}$ is 0.28 mag, but it may be higher or lower depending on the local stellar density. The uncertainties resulting from the use of optical colors in m_H^W, $R\sigma_{\rm col}$, are given in Table 2 and as discussed are quite small with a mean of 0.07 mag. There is also an *intrinsic dispersion*, $\sigma_{\rm int}$, resulting from the nonzero temperature width of the Cepheid instability strip. It can be determined empirically using nearby Cepheid samples which have negligible background errors. We find $\sigma_{\rm int} = 0.08$ mag for m_H^W (0.12 mag for m_I^W) using the LMC Cepheids from Macri et al. (2015) over a comparable period range (see Figure 6). This agrees well with expectations from the Geneva stellar models (Anderson et al., in prep.). We use this value as the intrinsic dispersion of mean m_H^W magnitudes. The last contribution comes from our use of random- or limited-phase (rather than mean-phase) $F160W$ magnitudes. Monte Carlo sampling of complete H-band light curves from Persson et al. (2004) shows that the use of a single random phase adds an error of 0.12 mag[2]. The relevant fractional contribution of the random-phase uncertainty for a given Cepheid with period P depends on the number of imaging epochs and the temporal interval between optical and NIR epochs, a fraction we approximate as $f_{\rm ph} = 1 - (\Delta T/P)$ for $\Delta T < P$ and $f_{\rm ph} = 1$ for $\Delta T > P$; the values of ΔT

---

[2]The sum of these terms, 0.14 mag, is smaller than the 0.21 mag assumed by R11; the overestimate of this uncertainty explains why the χ^2 of the P–L fits in that paper were low and resulted in the need to rescale parameter errors.

are given in Table 3. The value of this fraction ranges from ~ 1 (NIR observations at every optical epoch) to zero (a single NIR follow-up observation).

Thus, we assign a total statistical uncertainty arising from the quadrature sum of the intrinsic, random-phase, and photometric error (as determined empirically from the artificial-star simulations):

$$\sigma_{\rm tot} = (\sigma_{\rm sky}^2 + \sigma_{\rm int}^2 + (R\sigma_{\rm col})^2 + (f_{\rm ph}\sigma_{\rm ph})^2)^{\frac{1}{2}}.$$

We give the values of $\sigma_{\rm tot}$ for each Cepheid in Table 4. These have a median of 0.30 mag (mean of 0.32 mag) across all fields; mean values for each field range from 0.23 mag (NGC 3447) to 0.47 mag (NGC 4424). The mean for NGC 4258 is 0.39 mag.

3. Measuring the Hubble Constant

The determination of H_0 follows the formalism described in §3 of R09. To summarize, we perform a single, simultaneous fit to all Cepheid and SN Ia data to minimize the χ^2 statistic and measure the parameters of the distance ladder. We use the conventional definition of the distance modulus, $\mu = 5\log D + 25$, with D a luminosity distance in Mpc and measured as the difference in magnitudes of an apparent and absolute flux, $\mu = m - M$. We express the jth Cepheid magnitude in the ith host as

$$m_{H,i,j}^W = (\mu_{0,i} - \mu_{0,\rm N4258}) + {\rm zp}_{W,\rm N4258} + b_W \log P_{i,j} + Z_W\ \Delta\log\,[{\rm O/H}]_{i,j}, \tag{2}$$

where the individual Cepheid parameters are given in Table 4 and $m_{H,i,j}^W$ was defined in Equation 1. We determine the values of the nuisance parameters b_W and Z_W — which define the relation between Cepheid period, metallicity, and luminosity — by minimizing the χ^2 for the global fit to all Cepheid data. The reddening-free distances for the hosts relative to NGC 4258 are given by the fit parameters $\mu_{0,i} - \mu_{0,\rm N4258}$, while ${\rm zp}_{W,\rm N4258}$ is the intercept of the P–L relation simultaneously fit to the Cepheids of NGC 4258.

Uncertainties in the nuisance parameters are due to measurement errors and the limited period and metallicity range spanned by the variables. In R11 we used a prior inferred from external Cepheid datasets to help constrain these parameters. In the present analysis, instead, we explicitly use external data as described below to augment the constraints.

Recent *HST* observations of Cepheids in M31 provide a powerful ancillary set of Cepheids at a fixed distance to help characterize NIR P–L relations. Analyses of the *HST* PHAT Treasury data (Dalcanton et al. 2012) by Riess et al. (2012), Kodric et al. (2015), and Wagner-Kaiser et al. (2015) used samples of Cepheids discovered from the ground with NIR and optical magnitudes from *HST* to derive low-dispersion P–L relations. We used the union set of these samples and their WFC3 photometry in $F160W$ measured with the same algorithms as the previous hosts to produce a set of 375 Cepheids with $3 < P < 78$ d as shown in Figure 6. We add Equation 2 (actually, a set of equations) for these data to those from the other hosts, requiring the addition of

one nuisance parameter, the distance to M31, but providing a large range of $\log P$ (~ 1.4 dex) for the determination of the P–L relation slopes. These M31 Cepheids alone constrain the slope to an uncertainty of 0.03 mag dex^{-1}, a factor of 3 better than the prior used by R11. They also hint at the possible evidence of a break in the m_H^W P–L relation at the 2σ confidence level (Kodric et al. 2015) if the location of a putative break is assumed *a priori* to be at 10 days as indicated by optical P–L relations (Ngeow & Kanbur 2005). To allow for a possible break, we include two different slope parameters in Equation 2 in the primary analysis, one for Cepheids with $P > 10$ days and another for $P < 10$ days. We will consider alternative approaches for dealing with nonlinear P–L relations in §4.1.

The SN Ia magnitudes in the calibrator sample are simultaneously expressed as

$$m_{x,i}^0 = (\mu_{0,i} - \mu_{0,\mathrm{N4258}}) + m_{x,\mathrm{N4258}}^0, \tag{3}$$

where the value $m_{x,i}^0$ is the maximum-light apparent x-band brightness of a SN Ia in the ith host at the time of B-band peak, corrected to the fiducial color and luminosity. This quantity is determined for each SN Ia from its multiband light curves and a light-curve fitting algorithm. For the primary fits we use SALT-II (Guy et al. 2005; Guy et al. 2010). For consistency with the most recent cosmological fits we use version 2.4 of SALT II as used by Betoule et al. (2014) and more recently from Scolnic & Kessler (2016) [3] and for which $x = B$. The fit parameters are discussed in more detail in §4.2. In order to compare with R11 and to explore systematics in light-curve fits, we also use MLCS2k2 (Jha et al. 2007) for which $x = V$ (see §4.2 for further discussion).

The simultaneous fit to all Cepheid and SN Ia data via Equations 2 and 3 results in the determination of $m_{x,\mathrm{N4258}}^0$, which is the expected reddening-free, fiducial, peak magnitude of a SN Ia appearing in NGC 4258. The individual Cepheid P–L relations are shown in Figure 6. Lastly, H_0 is determined from

$$\log H_0 = \frac{(m_{x,\mathrm{N4258}}^0 - \mu_{0,\mathrm{N4258}}) + 5a_x + 25}{5}, \tag{4}$$

where $\mu_{0,4258}$ is the independent, geometric distance modulus estimate to NGC 4258 obtained through VLBI observations of water megamasers orbiting its central supermassive black hole (Herrnstein et al. 1999; Humphreys et al. 2005; Argon et al. 2007; Humphreys et al. 2008, 2013).

Here we make use of an *improved* distance estimate to NGC 4258 utilizing the same VLBI data and model from H13 but now with a 100-fold increase in the number of Monte Carlo Markov Chain (MCMC) trial values from 10^7 in that publication to 10^9 for each of three independent "strands" of trials initialized near and at $\pm 10\%$ of the H13 distance. The result is a reduction in the leading systematic error of 1.5% from H13 caused by "different initial conditions" for strands with only 10^7 MCMC samples to 0.3% for the differences in strands with 10^9 MCMC samples. The smoother probability density function (PDF) for the distance to NGC 4258 can be seen in Figure 7. The

---

[3]http://kicp.uchicago.edu/~dscolnic/Supercal/supercal_vH0.fitres

complete uncertainty (statistical and systematic) for the maser distance to NGC 4258 is reduced from 3.0% to 2.6%, and the better fit also produces a slight 0.8% decrease in the distance, yielding

$$D(\text{NGC}\,4258) = 7.54 \pm 0.17(\text{random}) \pm 0.10(\text{systematic})\ \text{Mpc},$$

equivalent to $\mu_{0,\text{N4258}} = 29.387 \pm 0.0568$ mag.

The term a_x in Equation 4 is the intercept of the SN Ia magnitude-redshift relation, approximately $\log cz - 0.2 m_x^0$ in the low-redshift limit but given for an arbitrary expansion history and for $z > 0$ as

$$a_x = \log\, cz \left\{ 1 + \frac{1}{2} \left[1 - q_0 \right] z - \frac{1}{6} \left[1 - q_0 - 3q_0^2 + j_0 \right] z^2 + O(z^3) \right\} - 0.2 m_x^0, \qquad (5)$$

measured from the set of SN Ia (z, m_x^0) independent of any absolute (i.e., luminosity or distance) scale. We determine a_x from a Hubble diagram of up to 299 SNe Ia with a light-curve fitter used to find the individual m_x^0 as shown in Figure 8. Limiting the sample to $0.023 < z < 0.15$ (to avoid the possibility of a coherent flow in the more local volume; z is the redshift in the rest frame of the CMB corrected for coherent flows) leaves 233 SNe Ia (in the next section we consider a lower cut of $z > 0.01$). Together with the present acceleration $q_0 = -0.55$ and prior deceleration $j_0 = 1$ which can be measured via high-redshift SNe Ia (Riess et al. 2007; Betoule et al. 2014) independently of the CMB or BAO, we find for the primary fit $a_B = 0.7127 \pm 0.0017$. Combining the peak SN magnitudes to the intercept of their Hubble diagram as $m_{x,i}^0 + 5a_x$ provides a measure of distance independent of the choice of light-curve fitter, fiducial source, and measurement filter. These values are provided in Table 5.

We use matrix algebra to simultaneously express the over 1400 model equations in Equations 2 and 3, along with a diagonal correlation matrix containing the uncertainties. We invert the matrices to derive the maximum-likelihood parameters, as in R09 and R11. Individual Cepheids may appear as outliers in the m_H^W P–L relations owing to (1) a complete blend with a star of comparable brightness and color, (2) a poor model reconstruction of a crowded group when the Cepheid is a small component of the total flux, (3) objects misidentified as classical Cepheids in the optical (e.g., blended Type II Cepheids), or (4) Cepheids with the wrong period (caused by aliasing or incomplete sampling of a single cycle). For our best fit we identify and remove outliers from the global model fit which exceed 2.7σ (see §4.1 for details), comprising ~2% of all Cepheids (or ~5% from all SN hosts). We consider alternative approaches for dealing with these outliers and include their impact into our systematic uncertainty in §4.1.

Our best fit using only the maser distance to NGC 4258 in Equation 4 to calibrate the Cepheids yields a Hubble constant of 72.39 ± 2.41 km s^{-1} Mpc^{-1}, a statistical uncertainty of 3.3% compared to 4.0% in R11. The statistical uncertainty is the quadrature sum of the uncertainties in the three independent terms in Equation 4. We address systematic errors associated with this measurement in §4.

3.1. Additional Anchors

We now make use of additional sources for the calibration of Cepheid luminosities, focusing on those which (i) are fundamentally geometric, (ii) have Cepheid photometry available in the V, I, and H bands, and (iii) offer precision comparable to that of NGC 4258, i.e., less than 5%. For convenience, the resulting values of H_0 are summarized in Table 6.

3.1.1. Milky Way Parallaxes

Trigonometric parallaxes to Milky Way Cepheids offer one of the most direct sources of geometric calibration of the luminosity of these variables. As in R11, we use the compilation from van Leeuwen et al. (2007), who combined 10 Cepheid parallax measurements with HST/FGS from Benedict et al. (2007) with those measured at lower precision with $Hipparcos$, plus another three measured only with significance by $Hipparcos$. We exclude Polaris because it is an overtone pulsator whose "fundamentalized" period is an outlier among fundamental-mode Cepheids. In their analysis, Freedman et al. (2012) further reduced the parallax uncertainties provided by Benedict et al. (2007), attributing the lower-than-expected dispersion of the P–L relation of the 10 Cepheids from Benedict et al. (2007) as evidence for lower-than-reported measurements errors. However, we think it more likely that this lower scatter is caused by chance ($\sim 2\sigma$) than overestimated parallax uncertainty, as the latter is dominated by the propagation of astrometry errors which were stable and well-characterized through extensive calibration of the HST FGS. As the sample of parallax measurements expands, we expect that this issue will be resolved, and for now we retain the uncertainties as determined by Benedict et al. (2007).

We add to this sample two more Cepheids with parallaxes measured by Riess et al. (2014) and Casertano et al. (2015) using the WFC3 spatial scanning technique. These measurements have similar fractional distance precision as those obtained with FGS despite their factor of 10 greater distance and provide two of only three measured parallaxes for Cepheids with $P > 10$ d. The resulting parallax sample provides an independent anchor of our distance ladder with an uncertainty of 1.6%, though this effectively increases to 2.2% after the addition of a conservatively estimated 0.03 mag zeropoint uncertainty between the ground and HST photometric systems (but see discussion in §5).

We use the parallaxes and the H, V, and I-band photometry of the MW Cepheids by replacing Equation 2 for the Cepheids in SN hosts and in M31 with

$$m_{H,i,j}^W = \mu_{0,i} + M_{H,1}^W + b_W \log P_{i,j} + Z_W \ \Delta \log \ [\mathrm{O/H}]_{i,j}, \tag{6}$$

where $M_{H,1}^W$ is the absolute m_H^W magnitude for a Cepheid with $P = 1$ d, and simultaneously fitting the MW Cepheids with the relation

$$M_{H,i,j}^W = M_{H,1}^W + b_W \ \log P_{i,j} + Z_W \ \Delta \log \ [\mathrm{O/H}]_{i,j}, \tag{7}$$

where $M_{H,i,j}^W = m_{H,i,j}^W - \mu_\pi$ and μ_π is the distance modulus derived from parallaxes, including standard corrections for bias (often referred to as Lutz-Kelker bias) arising from the finite S/N of parallax measurements (Hanson 1979). The H, V, and I-band photometry, measured from the ground, are transformed to match the WFC3 $F160W$, $F555W$, and $F814W$ as discussed in the next subsection. Equation 3 for the SNe Ia is replaced with

$$m_{x,i}^0 = \mu_{0,i} - M_x^0. \tag{8}$$

The determination of M_x^0 for SNe Ia together with the previous term a_x then determines H$_0$,

$$\log \mathrm{H}_0 = \frac{M_x^0 + 5a_x + 25}{5}. \tag{9}$$

For Cepheid photometry not derived directly from HST WFC3, we assume a fully-correlated uncertainty of 0.03 mag included as an additional, simultaneous constraint equation, $0 = \Delta\mathrm{zp} \pm \sigma_{\mathrm{zp}}$, to the global constraints with $\sigma_{\mathrm{zp}} = 0.03$. The free parameter, $\Delta\mathrm{zp}$, which expresses the zeropoint difference between HST WFC3 and ground-based data, is now added to Equation 7 for all of the MW Cepheids. In future work we intend to eliminate $\Delta\mathrm{zp}$ by replacing the ground-based photometry with measurements from HST WFC3 enabled by spatial scanning (Riess et al. 2014).

Using these 15 MW parallaxes as the only anchor, we find H$_0 = 76.09 \pm 2.41$ km s^{-1} Mpc^{-1}. In order to use the parallaxes together with the maser distance to NGC 4258, we recast the equations for the Cepheids in NGC 4258 in the form of Equation 7 with $\mu_{0,\mathrm{N4258}}$ in place of μ_π and the addition of the nuisance parameter $\Delta\mu_{\mathrm{N4258}}$. We then add the simultaneous constraint equation $0 = \Delta\mu_{\mathrm{N4258}} \pm \sigma_{\mu0,\mathrm{N4258}}$ with $\sigma_{\mu0,\mathrm{N4258}} = 0.0568$ mag. Compared to the use of the maser-based distance in §3, $\sigma_{\mu0,\mathrm{N4258}}$ has moved from Equation 4 to the *a priori* constraint on $\Delta\mu_{\mathrm{N4258}}$. This combination gives H$_0 = 73.85 \pm 1.97$ km s^{-1} Mpc^{-1}, an uncertainty of 2.3% and consistent with the value from NGC 4258 to within 1.2σ considering only the distance uncertainty in the geometric anchors.

3.1.2. LMC Detached Eclipsing Binaries

In R11 we also used photometry of Cepheids in the LMC and estimates of the distance to this galaxy based on detached eclipsing binaries (DEBs) to augment the set of calibrators of Cepheid luminosities. DEBs provide the means to measure geometric distances (Paczynski & Sasselov 1997) through the ability to determine the physical sizes of the member stars via their photometric light curves and radial velocities. The distance to the LMC has been measured with both early-type and late-type stars in DEBs. Guinan et al. (1998), Fitzpatrick et al. (2002), and Ribas et al. (2002) studied three B-type systems (HV 2274, HV 982, EROS 1044) which lie close to the bar of the LMC and therefore provide a good match to the Cepheid sample of Macri et al. (2015). In R11 we used

an average distance modulus for these of 18.486 ± 0.065 mag[4]. However, for early-type stars it is necessary to estimate their surface brightness via non-LTE (local thermodynamic equilibrium) model atmospheres, introducing an uncertainty that is difficult to quantify.

The approach using DEBs composed of late-type stars is more reliable and fully empirical because their surface brightness can be estimated from empirical relations between this quantity and color, using interferometric measurements of stellar angular sizes to derive surface brightnesses (Di Benedetto 2005). Pietrzyński et al. (2013) estimated the distance to the center of the LMC to 2% precision using 8 DEBs composed of late-type giants in a quiet evolutionary phase on the helium burning loop, located near the center of the galaxy and along its line of nodes. The individual measurements are internally consistent and yield $\mu_{\mathrm{LMC}} = 18.493 \pm 0.008$ (stat.) ± 0.047 (sys.) mag, with the uncertainty dominated by the accuracy of the surface brightness vs. color relation.

Recently, Macri et al. (2015) presented NIR photometry for LMC Cepheids discovered by the OGLE-III project (Soszynski et al. 2008), greatly expanding the sample size relative to that of Persson et al. (2004) from 92 to 785, although the number of Cepheids with $P > 10$ d increased more modestly from 39 to 110. Similarly to the M31 Cepheids, the LMC Cepheids provide greater precision for characterizing the P–L relations than those in the SN Ia hosts, and independently hint at a change in slope at $P \approx 10$ days (Bhardwaj et al. 2016).

We transform the ground-based V, I and H-band Vega-system photometry of Macri et al. (2015) into the Vega-based HST/WFC3 photometric system in $F555W$, $F814W$ and $F160W$, respectively, using the following equations:

$$
\begin{align}
m_{555} &= V + 0.034 + 0.11(V - I) \tag{10}\\
m_{814} &= I + 0.02 - 0.018(V - I) \tag{11}\\
m_{160} &= H + 0.16(J - H) \tag{12}
\end{align}
$$

where the color terms were derived from synthetic stellar photometry for the two systems using SYNPHOT (Laidler 2005). To determine any zeropoint offsets (aside from the potentially different definitions of Vega) for the optical bands we compared photometry of 97 stars in the LMC observed in V and I by OGLE-III and in WFC3/F555W and F814W as part of HST-GO program #13010 (P.I.: Bresolin). The latter was calibrated following the exact same procedures as H16, which uses the UVIS 2.0 WFC3 Vegamag zeropoints. The uncertainties of the zeropoints in the optical transformations were found to be only 4 mmag, far smaller than the assumed ground-to-HST zeropoint uncertainty. The change in color, $V - I$ is quite small, at 0.014 mag or a change (decrease) in H_0 of 0.3 % for a value determined solely from an anchor with ground-based Cepheid photometry (LMC or MW). For H-band transformed to $F160W$, the net offset besides the aforementioned color term is zero after cancellation of an 0.02 mag offset measured between HST and 2MASS NIR

---

[4]A fourth system (HV 5936; Fitzpatrick et al. 2003) is located several degrees away from the bar and yields a distance that is closer by 3σ. Additional lines of evidence presented in that paper suggest this system lies above the disk of the LMC, closer to the Galaxy.

photometry (Riess 2011) and the same in the reverse direction from the very small count-rate non-linearity of WFC3 at the brightness level of extragalactic Cepheids (Riess 2010). The mean metallicity of the LMC Cepheids is taken from their spectra by (Romaniello et al. 2008) to be $[O/H] = -0.25$ dex.

Using the late-type DEB distance to the LMC as the sole anchor and the Cepheid sample of Macri et al. (2015) for a set of constraints in the form of Equation 7 yields $H_0 = 71.93 \pm 2.58$ km s^{-1} Mpc^{-1}. As in the prior section, these fits include free parameters $\Delta\mu_{LMC}$ and Δzp, with additional constraint $0 = \Delta\mu_{LMC} \pm \sigma_{\mu,LMC}$, Using all three anchors, the same set used by R11 and by Efstathiou (2014), results in $H_0 = 73.02 \pm 1.62$ km s^{-1} Mpc^{-1}, a 2.2% statistical uncertainty. The fitted parameters which would indicate consistency within the anchor sample are $\Delta\mu_{N4258} = -0.044$, within the range of its 0.0568 mag prior, and $\Delta\mu_{LMC} = -0.041$, within range of its 0.0452 mag prior. The metallicity term for the NIR-based Wesenheit is small and not well-detected with $Z_W = -0.14 \pm 0.08$ including systematic uncertainties. The Appendix shows how the system of equations is arranged for the primary fit.

3.1.3. DEBs in M31

As discussed in §3, we make use of a sample of 375 Cepheids in M31 in order to help characterize the Cepheid P–L relations. In principle, we can also use M31 as an anchor in the determination of H_0 by taking advantage of the two DEB-based distance estimates to the galaxy (Ribas et al. 2005; Vilardell et al. 2010) which have a mean of $\mu_0 = 24.36 \pm 0.08$ mag.

Yet, there are several obstacles with the use of M31 as an anchor. The PHAT *HST* program (Dalcanton et al. 2012), which obtained the *HST* data, did not use the $F555W$ filter, nor did it include time-series data, so we cannot use the same individual, mean-light $F555W-F814W$ colors to deredden the Cepheids in $F160W$ as for other SH0ES galaxies (or the individual mean $V-I$ colors to deredden H-band data with a 0.03 mag uncertainty as for LMC and MW Cepheids as individual ground-based colors are too noisy). The best available color for measuring the individual reddenings of the M31 Cepheids is $F110W-F160W$ so we must recalibrate these colors to match the reddening in the $V-I$ data. Following Riess et al. (2012), we add a constant to these colors so that their mean measured $F160W$ extinction is the same as derived from the mean $V-I$ Cepheid colors in M31 based on data from the ground-based DIRECT program (Kaluzny 1998)[5]. The advantage of the latter approach is that it can account for *differential* reddening along the line of sight while providing a reddening correction which is consistent with that used for Cepheids in all other targets. We adopt an 0.02 mag systematic uncertainty, $\sigma_{zp,opt}$, between the ground-based

---

[5]By equating the mean $V-I$ dereddening with that for $F110W-F160W$, we can solve for a color offset to ensure they yield the same result. That is, $0.40\langle V-I \rangle = 1.49\langle F110W - F160W - X \rangle$, where $\langle V-I \rangle = 1.23$ mag from DIRECT gives $X = 0.22$ mag. Note that the reddening parameters (now adopted from Fitzpatrick 1999) and the Cepheid samples differ from those used by Riess et al. (2012), leading to a different value of X.

optical colors of Cepheids and those measured from space. With the same formalism used for the LMC but with M31 as the sole anchor we find $H_0 = 74.45 \pm 3.34$ km s^{-1} Mpc^{-1}, consistent with the value of 73.02 ± 1.79 km s^{-1} Mpc^{-1} derived from the other three anchors.

On the other hand, as previously discussed, DEB distances for early-type stars (the only ones currently measured in M31) include significant inputs from non-LTE stellar model atmospheres with systematic uncertainties that are hard to assess. It is somewhat reassuring to note that in the LMC, where both types of DEBs have been measured, the difference in the distance moduli obtained from either type is only 0.007 ± 0.08 mag, a test with the same precision as the early-type DEB distance to M31. Future measurements of late-type DEBs or water masers in M31 (Darling 2011) would place M31 as an anchor on equal footing with the others.

To be conservative, we use as our primary determination of H_0 the result from the combination of NGC 4258 masers, MW parallaxes, and LMC late-type DEBs (the same set of anchors used by R11): $H_0 = 73.02 \pm 1.79$ km s^{-1} Mpc^{-1}. Note, however, the consistency of our primary result with the result of $H_0 = 74.45 \pm 3.34$ km s^{-1} Mpc^{-1} using M31 alone. If M31 were included together with the other anchors, the resulting value of H_0 would be 73.24 ± 1.75 km s^{-1} Mpc^{-1}.

While the global model accounts for the covariance between all distances and model parameters, we can explore the internal agreement of the Cepheid and SN distance estimates by deriving *approximate* Cepheid-only distances for the 18 hosts. For each host, we remove only its SN distance from the global fit and derive its Cepheid distance, $\mu_{0,i}$ based on the full set of equations. The result is a set of Cepheid distances to each host which are independent of their SN distances (although these distances are slightly correlated with each other and thus do not provide a substitute for the full analysis which accounts for such covariance). The results are listed in Table 5, column 5 as approximate Cepheid distances (ignoring the covariance) and Figure 9 shows the SN distances versus those from Cepheid optical and NIR magnitudes. Figure 10 shows an *approximation* to the full distance-ladder fit to provide a sense of the sampling using the previously described approximations. These approximations should be good to ~ 0.01–0.02 mag. The resulting relation between the SN and Cepheid-based distances will be considered in the next subsections.

4. Analysis Systematics

The statistical uncertainties quoted thus far include the full propagation of all known contributions as well as the degeneracies resulting from simultaneous modeling and characterization of the whole dataset of > 2200 Cepheids, 18 SNe Ia, 15 MW parallaxes, the DEB-based distance to the LMC, and the maser distance to NGC 4258. Our model formally contains parameters used to propagate what were considered sources of systematic uncertainties in other analyses (Freedman et al. 2001, 2012; Sandage et al. 2006) such as zeropoint errors, metallicity dependences, and the slopes and breaks in the P–L relation, therefore our statistical uncertainties incorporate many effects that others consider among systematics (see Appendix).

Table 5.   Approximations for Distance Parameters

Host	SN	$m^0_{B,i}$ $+5a_B$	σ^a	μ^b_{Ceph}	σ	$M^0_{B,i}$	σ
				(mag)			
M101	2011fe	13.310	0.117	29.139	0.0459	-19.392	0.1256
N1015	2009ig	17.013	0.123	32.503	0.0815	-19.053	0.1475
N1309	2002fk	16.755	0.116	32.524	0.0558	-19.332	0.1287
N1365	2012fr	15.480	0.125	31.306	0.0576	-19.389	0.1376
N1448	2001el	15.763	0.116	31.310	0.0461	-19.110	0.1248
N3021	1995al	16.526	0.117	32.498	0.0908	-19.535	0.1481
N3370	1994ae	16.474	0.115	32.071	0.0501	-19.160	0.1254
N3447	2012ht	16.264	0.124	31.910	0.0435	-19.209	0.1314
N3972	2011by	16.047	0.116	31.588	0.0721	-19.104	0.1365
N3982	1998aq	15.793	0.115	31.735	0.0703	-19.505	0.1348
N4038	2007sr	15.795	0.114	31.378	0.1183	-19.146	0.1643
N4424	2012cg	15.109	0.109	31.080	0.2958	-19.534	0.3153
N4536	1981B	15.176	0.124	30.923	0.0533	-19.310	0.1349
N4639	1990N	15.982	0.115	31.533	0.0723	-19.114	0.1358
N5584	2007af	16.264	0.115	31.773	0.0470	-19.072	0.1242
N5917	2005cf	16.571	0.115	32.261	0.1040	-19.253	0.1551
N7250	2013dy	15.866	0.115	31.497	0.0795	-19.194	0.1398
U9391	2003du	17.033	0.114	32.919	0.0636	-19.449	0.1305

Note. — (a) For SALT-II, 0.1 mag added in quadrature to fitting error. (b) Approximate, SN-independent Cepheid-based distances as described at the end of §3.

Following the approach of R09 and R11, we therefore explore reasonable alternatives to the global determination of H_0 which are not easily parameterized for inclusion in the framework of §3, and we use these to determine an additional systematic error component. While unknown systematic errors can never be ruled out, we address this possibility in §4 by comparing our measurement to independent measurements of H_0 which do not utilize SN-based distance measurements.

4.1. Cepheid Systematics

The Cepheid outlier fraction in §3 is $\sim 2\%$ for all hosts (or $\sim 5\%$ across all SN hosts), smaller than the 15%–20% in R11. This reduction in the outlier fraction results largely from the use of a color selection in $F814W - F160W$ around the median color in each host to remove blends with unresolved sources of comparable luminosity and different color (e.g., red giants, blue supergiants, unresolved star clusters). This is a useful criterion as it is distance- and period-independent, insensitive to reddening, and anchored to the physical properties of Cepheids (i.e., stars with spectral types F–K). The well-characterized LMC Cepheids from Macri et al. (2015) have a mean $I - H$ of 0.96 mag with a dispersion of just 0.10 mag, much smaller than the allowed 1.2 mag breadth which alone would exclude only stars hotter than early-F or cooler than late-K (i.e., colors which cannot result from Cepheids). Because measurement errors owing to blending are correlated across bands, the uncertainty in this color is smaller than either band and a factor of ~ 6 smaller than the allowed range, so colors outside the range primarily result from color blends rather than noise. Doubling the breadth of the color cut decreased H_0 by $0.9 \ \mathrm{km \, s^{-1} \, Mpc^{-1}}$ and removing a color cut altogether lowered H_0 by an additional $0.2 \ \mathrm{km \, s^{-1} \, Mpc^{-1}}$, both well below the statistical uncertainty.

We further tested the use of our color cut by simulating the appearance of a distribution of Cepheids in a galaxy at $D \approx 30$ Mpc using star catalogues of the LMC. Cepheids with low optical blending (to allow their identification by amplitude and allowed range in $F555W - F814W$; see H16 and Ferrarese et al. 2000) but with significant NIR blending are most often blended with red giants. This shifts their colors redward in $F814W - F160W$ to a degree, on average, that is proportional to their local surface brightness. While we account for this mean, blended sky level in our photometry, the occasional "direct hits" by red or blue sources are removed by the color cut. However, blending may *still* occur with stars of a similar color, such as the (less common) yellow supergiants, or the sample may include a small number of objects erroneously identified as Cepheids. For these reasons we still identify and remove a small number of objects, $\sim 2\%$ of the sample, as outliers from the P–L relations.

A number of reasonable approaches would likely suffice for identifying these outliers as demonstrated for the R11 sample (Becker et al. 2015; Efstathiou 2014; Kodric et al. 2015). R11 used a 2.5σ threshold to identify outliers from the *individual H*-band P–L relations for their primary H_0 analysis, while evaluating the impact of no outlier rejection to determine the sensitivity of H_0 to this step. Efstathiou (2014) used a similar threshold but applied to outliers of the final, *global* fit.

Kodric et al. (2015) used a global rejection as well but recalculated the global fit after removing the single most deviant point until none remained above the threshold. Becker et al. (2015) applied a Bayesian characterization of outliers, attributing them to a second, contaminating distribution with uniform properties. However, the artificial-star tests and LMC analysis indicate that the outliers are well described by the tails of the blending distribution. For our primary fit we use a *global* rejection of 2.7σ, the threshold where the $\chi^2_\nu = 0.95$ of our global fit matches that of a normal distribution with the same rejection applied. Following Kodric et al. (2015) we recalculated the global fit after removing the single most deviant point until none remain above the 2.7σ threshold. We also performed as variants a single-pass, global rejection and a rejection from individual P–L relations, both applied at the aforementioned threshold and a larger 3.5σ threshold, as well as *no outlier rejection*. The results of these are all given in Table 8. These variants of outlier rejection changed H_0 by less than $0.5 \ \mathrm{km\,s^{-1}\,Mpc^{-1}}$. Because the outlier fraction of 2% is quite small here and the Cepheid slope is better constrained relative to that of R11, we conclude that the outlier analysis does not warrant further consideration. The Cepheids in Table 4 are those that passed the best-fit, global 2.7σ outlier rejection.

We consider a number of variants related to the Cepheid reddening law. Besides the primary fits, which use a Fitzpatrick (1999) law with $R_V = 3.3$, we also use $R_V = 2.5$ and alternative formulations of the reddening law from Cardelli et al. (1989) and Nataf et al. (2015). We also explore variants related to a possible break in the Cepheid P–L relation near 10 days. Our primary fit allows for a break or discontinuity (while not requiring one) by providing two independent slope parameters: one for Cepheids at $P > 10$ days and one for $P < 10$ days. The allowance for a break only increases the uncertainty in H_0 by $0.01 \ \mathrm{km\,s^{-1}\,Mpc^{-1}}$ which is negligible. We also evaluate changes in H_0 arising from a single-slope formulation for all periods, as well as from removing all Cepheids with $P < 10$ days, or removing those with $P > 60$ days as shown in Table 8. Interestingly, we see no evidence of a change in slope at $P = 10$ days in the M_H^W P–L relation to a precision of $0.02 \ \mathrm{mag\,dex^{-1}}$ in the global fit to all Cepheids. Hints of an increasing (LMC) or decreasing (M31) slope with period are not confirmed in this broader analysis with many more hosts. We further included variants that ignored the possibility of a Cepheid metallicity dependence and another based on a T_e recalibration of nebular oxygen abundances (Bresolin 2011). We also included a variant foregoing the use of optical colors to correct for NIR reddening as it tends to be low. The results of all these variants are presented in Table 8.

Comparing the individual SN distances to the previously discussed approximate, independent Cepheid distances, we find none of the hosts to be an outlier. There is also no evidence ($< 1\sigma$) for a trend between SN and Cepheid NIR distances over a 3.8 mag range in distance modulus (equivalent to a factor of 5.8 in distance). This suggests that Cepheids are not associated with significant unresolved luminosity overdensities across the range of 7–38 Mpc spanned by our sample of SN hosts and one of our anchors (NGC 4258). This agrees well with Senchyna et al. (2015), who used *HST* to determine that only $\sim 3\%$ of Cepheids in M31 are in parsec-scale clusters. Further, only a small fraction of these would alter Cepheid photometry at the resolution available from the ground

or the similar resolution of *HST* at the distance of the SN hosts.

Lastly, we test for a dependence of the measured Cepheid distance with the level of blending by comparing the five hosts with blending higher than the inner region of NGC 4258 to the remaining 13. The difference in the mean model residual distances of these two subsamples is 0.02 ± 0.07 mag, providing no evidence of such a dependence.

4.2. Optical Wesenheit Period-Luminosity Relation

The SH0ES program was designed to identify Cepheids from optical images and to observe them in the NIR with $F160W$ to reduce systematic uncertainties related to the reddening law, its free parameters, sensitivity to metallicity, and breaks in the P–L relation. However, some insights into these systematics may be garnered by replacing the NIR-based Wesenheit magnitude, m_H^W, with the optical version used in past studies (Freedman et al. 2001), $m_I^W = I - R(V - I)$, where $R \equiv A_I/(A_V - A_I)$ and the value of R here is ~ 4 times larger than in the NIR. The advantage of this change is the increase in the sample by a little over 500 Cepheids in *HST* hosts owing to the greater field of view (FoV) of WFC3/UVIS. Of these additional Cepheids, 250 come from M101, 140 from NGC 4258, and the rest from the other SN hosts. In Table 8 we give results based on Cepheid measurements of m_I^W instead of m_H^W for the primary fit variant with all 4 anchors, the primary fit anchor set of NGC 4258, MW and LMC and for NGC 4258 as the sole anchor.

The fits for all Cepheids with m_I^W data generally show a significantly steeper slope for $P < 10$ days than for $P > 10$ days, with our preferred variant giving a highly significant slope change of 0.15 ± 0.03 mag dex^{-1}. We also see strong evidence of a metallicity term with a value of -0.27 ± 0.05 mag dex^{-1} for our preferred fit, also highly significant and consistent with the value from Sakai et al. (2004) of -0.24 ± 0.05 mag dex^{-1}. The constraint on the metallicity term is nearly unchanged when using NGC 4258 as the sole anchor, -0.30 ± 0.06 mag dex^{-1}, demonstrating that the metallicity constraint comes from the metallicity gradients and SN host-to-host distance variations and *not* from improving the consistency in the distance scale of different anchors.

The dispersion between the individual SN and Cepheid distances (see Figure 9 and the next subsection) is $\sigma = 0.12$ mag for m_I^W, somewhat smaller than $\sigma = 0.15$ mag from m_H^W. Some reduction may be expected because a larger number of Cepheids are available in the optical relative to the NIR. However, the SNe have a mean distance uncertainty of 0.12 mag and the sets of m_H^W magnitudes in each host have a typical mean uncertainty of 0.06 mag, indicating that the dispersion between SN and Cepheid distances is already dominated by the SN error and leaving little room for improvement with additional Cepheids. The one exception is NGC 4424, where the paucity of variables with valid NIR measurements results in a Cepheid-dominated calibration error which is reduced by a third by adding Cepheids only available in the optical. Based on the good agreement between the relative SN and Cepheid distances and uncertainties, we conclude that the intrinsic SN dispersion of 0.1 mag from SALT-II is reasonable.

Using the three primary anchors and the optical Wesenheit P–L relation, we find $H_0 = 71.19 \pm 1.53$ km s^{-1} Mpc^{-1} (statistical uncertainty only), extremely similar to the NIR-based result and with an error just 0.08 km s^{-1} Mpc^{-1} smaller. We determined the systematic error for the optical Wesenheit from the dispersion of its variants after eliminating those expected to perform especially poorly in the optical: no allowance for reddening, no metallicity term, and no lower-period cutoff. Even without these variants, the systematic error in the optical of 2.8% is still considerably worse than its NIR counterpart and is also larger than the statistical error. The reason is that changes to the treatment of reddening, metallicity, P–L relation breaks, and outlier rejection cause larger changes in H_0 for the optical Wesenheit magnitudes than for the NIR counterparts. This is a fairly uniform result, not driven by any one or two variants. For example, changing from the preferred Fitzpatrick (1999) reddening law to the alternative formulations by Cardelli et al. (1989) or Nataf et al. (2015) changes H_0 by 0.18 and 0.38 km s^{-1} Mpc^{-1} for m_H^W, respectively. These same variants change H_0 by -2.15 and 3.82 km s^{-1} Mpc^{-1} for the m_I^W data. This increased sensitivity to the reddening law is a natural consequence of the larger value of R. Changing the two-slope P–L formulation to a single slope or restricting the period range to $P > 10$ or $P < 60$ days changes H_0 by -1.64, -1.24, and 1.79 km s^{-1} Mpc^{-1}, respectively, for the optical formulation. These changes are generally smaller for the NIR Wesenheit at 0.25, -1.57, and 0.01 km s^{-1} Mpc^{-1}, respectively. Finally, changing the outlier clipping from one-at-a-time to a single pass changes H_0 by 0.14 and -0.90 km s^{-1} Mpc^{-1} for the NIR and optical approaches, respectively.

Using the three primary anchors with the optical Wesenheit and including systematic errors, we find $H_0 = 71.19 \pm 2.55$ km s^{-1} Mpc^{-1}, equivalent to an uncertainty of 3.5%. This result is somewhat less precise than the 3.3% total error of R11, which used the NIR Wesenheit but only 8 SN-Cepheid hosts instead of the present 18. Until or unless additional studies can improve our understanding of Cepheid reddening, metallicity sensitivity, and the scale of P–L breaks at optical wavelengths, our analysis shows that improvements in the determination of H_0 via Cepheids must primarily rely on the inclusion of NIR observations.

Similar conclusions are reached when using only NGC 4258 as an anchor: $H_0 = 71.98 \pm 2.26$ km s^{-1} Mpc^{-1} without systematic errors, so the statistical error is slightly better than the equivalent NIR result at 3.1%. However, the systematic error of 2.4% is considerably worse, leading to a combined value of $H_0 = 71.98 \pm 2.87$ km s^{-1} Mpc^{-1}. While the use of strictly optical Wesenheit magnitudes can be informative, our best results for H_0 with lowest systematics consistently come from using the NIR data in concert with optical observations.

4.3. Supernova Systematics

The SALT-II SN light-curve fits, the composition of the Hubble-flow sample, and sources of SN photometry used to determine a_X in Equation 5 are described in Scolnic et al. (2015); Scolnic & Kessler (2016). These take advantage of the "Supercal" procedure (Scolnic et al. 2015) which uses reference stars in the fields of the SNe and the homogeneous set of star photometry over

3π steradians from Pan-STARRS to remove small photometric inconsistencies between SN photometry obtained across multiple observatories and systems. As is common in recent analyses of SN Ia distances (e.g., Betoule et al. (2014)), to determine a_X we use "quality cuts" to include only SN Ia light curves for which the SALT color parameter (c) is within ± 0.3, the light-curve parameter (x_1) is within ± 3.0 (error < 1.5), the χ^2 of the light-curve fit is "good" (fitprob > 0.001), the peak time of the light curve is constrained to better than 2 days, and the uncertainty in the corrected peak magnitude is < 0.2 mag. All of the 18 calibrators pass these quality cuts as well. The SN redshifts are corrected for coherent (peculiar) flows (Scolnic et al. 2015, 2014) which reduces correlated deviations from expansion caused by visible large-scale structure and empirical residuals determined from simulations (Scolnic & Kessler 2016). A residual velocity (peculiar) error of $250\,\mathrm{km\,s^{-1}}$ is assumed. As a final step, we exclude SNe Ia which deviate from the form of Equation 5 by more than 3σ; this excludes 3% of the sample for the primary fit with $0.0233 < z < 0.15$, leaving 231 SNe Ia (or 299 SNe Ia for variants with $0.01 < z < 0.15$). These have a dispersion of 0.128 mag around Equation 5 with a mean error of 0.129 mag, and a χ^2 per degree of freedom of 0.91, and yield $a_B = 0.71271 \pm 0.00170$ for SALT-II ($a_V = 0.7005$ for MLCS2k2). As an alternative to the SALT-II light-curve fitter, we used the MLCS2k2 fitter (Jha et al. 2007) with a value of $R_V = 2.5$ for the SN host galaxy, the same as the primary fits of R11. The resulting value of H_0 is higher by $1.2\,\mathrm{km\,s^{-1}\,Mpc^{-1}}$ or $0.7\,\sigma$ of the total error as given in Table 8.

As in R11, we make use of several studies (Hicken et al. 2009a; Kelly et al. 2010; Lampeitl et al. 2010; Sullivan et al. 2010) which have shown the existence of a small step *brighter* for the corrected SN magnitude for hosts more massive than $\log M_{\mathrm{stellar}} \sim 10$. We use the same value of 0.06 mag used by (Betoule et al. 2014) for the size of the mass step to account for this effect. The net effect on H_0 is a small decrease of 0.7% because of the modest difference in masses of the nearby hosts (mean $\log M_{\mathrm{stellar}} = 9.8$) and of those that define the magnitude-redshift relation (Sullivan et al. 2010, mean $\log M_{\mathrm{stellar}} = 10.5$). We include these corrections based on host-galaxy mass in our present determination of $m_{B,i}^0$ given in Table 5 and for a_x, correcting those with hosts above and below $\log M_{\mathrm{stellar}} \sim 10$ by 0.03 fainter and brighter, respectively.

An alternative host dependence on SN Ia distance has been proposed by Rigault et al. (2013, 2015) based on the local star-formation rate (LSFR) measured at the site of the SN. The results from Rigault et al. (2015) suggested a $\sim 3\sigma$ correlation between SN distance residual and LSFR inferred from ultraviolet photometry measured with *GALEX* for a set of 82 SNe Ia from Hicken et al. (2009b), with somewhat higher significance for distances from MLCS2k2 and somewhat lower for SALT-II. Jones et al. (2015) repeated the LSFR analysis using a larger sample of SNe Ia which better matched the samples and light-curve quality selection used in the cosmological analyses of R11 and Betoule et al. (2014) as well as the more recent version of SALT II. Using 179 *GALEX*-imaged SN Ia hosts from the JLA SN sample (Betoule et al. 2014) and the Pan-STARRS sample (Scolnic et al. 2015), or 157 used by R11, the significance of a LSFR effect diminished to $\lesssim 1\sigma$ due to two differences from Rigault et al. (2015): (1) the increase in the sample statistics, and (2) use of the JLA or R11 quality criteria. Because we employ both the larger local SN sample as well

as the quality cuts used by Jones et al. (2015), we include only the mass-based correction whose significance has remained in cosmological SN samples.

Nevertheless, if we were to assume the existence of a LSFR (despite the preceding lack of significance), we can select a Hubble-flow sample to match the LSF of the calibrator sample and thus nullify the possible impact on H_0. In the calibrator sample, 16 of 18 hosts (or 89%) are above the LSFR threshold adopted by Rigault et al. (2013, 2015), which is a larger fraction than the 50–60% in the Hubble-flow sample (Jones et al. 2015). To determine an upper limit on a LSFR mismatch and thus H_0 across sets, we selected all Hubble-flow SNe significantly above the LSFR threshold (i.e., a purely LSFR sample), requiring these SNe Ia to have good *GALEX* detections. By changing the Hubble flow selection, only the term a_X is affected. For this all-LSFR sample, a_B is higher than for the primary fit by 0.00296 at $z > 0.0233$ and lower by 0.0012 at $z > 0.01$. Thus the Hubble constant from the primary fit increased by 0.7 or decreased by 0.2 $\mathrm{km\,s^{-1}\,Mpc^{-1}}$, respectively (see Table 8). Thus even if a relation existed, we find that a LSFR in SN hosts would have no significant impact on the determination of H_0 here.

However, to address the possibility of host-galaxy dependence that arises from sample selection, we also recalculated the intercept of the Hubble-flow SNe (a_X) using only those found in spiral hosts. Because the 18 hosts selected for Cepheid observations were chosen on the basis of their appearance as spirals (as well as their proximity and modest inclination), this selection would be expected to match the two samples if global star formation or its history had an impact on the measured SN distance (we cannot think of any preference for selection related to the star formation rate at the SN site relative to the whole host). Because the Hubble-flow sample is so much larger than the nearby sample, such a cut has a modest effect on the uncertainty in H_0. Doing so raised H_0 for the SALT-II fitter and lowered H_0 for MLCS2k2 each by $\sim 0.5\,\mathrm{km\,s^{-1}\,Mpc^{-1}}$. We note that the spiral-host sample has a mean LSFR of -2.21 dex, similar to the mean of the 18 calibrators at -2.23 dex and higher than the full Hubble-flow set of -2.58 dex.

We also changed the lower redshift cutoff of the Hubble diagram from $z = 0.023$ to $z = 0.01$, originally adopted to mitigate the impact of a possible local, coherent flow. This raised H_0 by $0.1\,\mathrm{km\,s^{-1}\,Mpc^{-1}}$ for the primary fit. Changing the deceleration parameter used to fit the SNe Ia at $0.0233 < z < 0.15$ from $q_0 = -0.55$ (as expected for $\Omega_M = 0.3$, $\Omega_\Lambda = 0.7$) to -0.60 ($\Omega_M = 0.27$, $\Omega_\Lambda = 0.73$; or $\Omega_M = 0.3$, $\Omega_{DE} = 0.7$, $w = -1.05$) decreases H_0 by 0.2%.

Two of the SNe in the calibrator sample (SN 1981B and SN 1990N) were measured before the Hubble-flow sample was acquired. Relative to the global fit, SN 1990N is faint by 0.15 ± 0.14 mag and SN 1981B is bright by 0.08 ± 0.14 mag, so this older digital photometry does not appear to bias the value of H_0 in a significant way.

A budget for the sources of uncertainty in the determination of H_0 is given in Table 7. These are necessarily marginalized approximations, as they do not show the (small) covariance between terms included in the full global fit. All of the discussed NIR variants, 207 in total including combinations of anchors, are listed in Table 8 and their histogram is plotted in Figure 11. The systematic error

Table 6.   Best Estimates of H_0 Including Systematics

Anchor(s)	Value [km s^{-1} Mpc^{-1}]
One anchor	
NGC 4258: Masers	72.39 ± 2.56
MW: 15 Cepheid Parallaxes	76.09 ± 2.41
LMC: 8 Late-type DEBs	71.93 ± 2.70
M31: 2 Early-type DEBs	74.45 ± 3.34
Two anchors	
NGC 4258 + MW	73.85 ± 1.97
Three anchors (preferred)	
NGC 4258 + MW + LMC	**73.02 ± 1.79 km s^{-1} Mpc^{-1}**
Four anchors	
NGC 4258 + MW + LMC + M31	73.24 ± 1.75
Optical only (no NIR), three anchors	
NGC 4258 + MW + LMC	71.19 ± 2.55

Table 7. H_0 Error Budget for Cepheid and SN Ia Distance Ladders[*]

Term	Description	Prev. LMC	R09 N4258	R11 All 3	This work N4258	This work All 3
σ_{anchor}	Anchor distance	5%	3%	1.3%	2.6%	1.3%
$\sigma_{\mathrm{anchorPL}}^{a}$	Mean of P–L in anchor	2.5%	1.5%	0.8%	1.1%	0.7%
$\sigma_{\mathrm{hostPL}}/\sqrt{n}$	Mean of P–L values in SN Ia hosts	1.5%	1.5%	0.6%	0.4%	0.4%
$\sigma_{\mathrm{SN}}/\sqrt{n}$	Mean of SN Ia calibrators	2.5%	2.5%	1.9%	1.3%	1.3%
σ_{m-z}	SN Ia m–z relation	1%	0.5%	0.5%	0.4%	0.4%
$R\sigma_{\lambda,1,2}$	Cepheid reddening, zeropoints, anchor-to-hosts	4.5%	0.3%	1.4%	0%	0.7%
σ_Z	Cepheid metallicity, anchor-to-hosts	3%	1.1%	1.0%	0.4%	0.8%
σ_{PL}	P–L slope, $\Delta \log P$, anchor-to-hosts	4%	0.5%	0.6%	0.2%	0.5%
σ_{WFPC2}	WFPC2 CTE, long-short	3%	N/A	N/A	N/A	N/A
subtotal, $\sigma_{H_0}^{b}$		10%	4.7%	2.9%	3.4%^{c}	2.2%
Analysis Systematics		N/A	1.3%	1.0%	1.0%	0.9%
Total, σ_{H_0}		10%	4.8%	3.3%	3.5%	2.4%

Note. — (*) Derived from diagonal elements of the covariance matrix propagated via the error matrices associated with Equations 1, 3, 7, and 8. (a) For MW parallax, this term is already included with the term above. (b) For R09, R11, and this work, calculated with covariance included. (c) One anchor not included in R11 estimate of σ_{H_0} to provide a crosscheck.

was estimated based on the variations in H_0 resulting from the reasonable, alternative fits. As shown in this figure, the histogram for the primary-fit anchors (NGC 4258, MW, and LMC) is well fit by a Gaussian distribution with $\sigma = 0.77$ km s^{-1} Mpc^{-1}, a systematic uncertainty that is a little less than half of the statistical error. None of the variants is a noteworthy outlier from this distribution. Including the systematic error, we arrive at a complete result of $H_0 = 73.02 \pm 1.79$ km s^{-1} Mpc^{-1}, corresponding to a total uncertainty, combining statistical and systematic contributions, of 2.4%.

5. Discussion

Our primary fit of $H_0 = 73.02 \pm 1.79$ km s^{-1} Mpc^{-1} is 3.0σ higher than the value of 67.27 ± 0.66 km s^{-1} Mpc^{-1} predicted by Planck Collaboration et al. (2015) based on ΛCDM with 3 neutrino flavors having a mass of 0.06 eV and the *Planck* CMB data (TT,TE,EE+LowP; see their Figure 12). Assuming the 3.0σ difference is not a fluke (99.8% confidence), possible explanations include systematic errors in the local H_0 or CMB measurements, or an unexpected feature in the cosmological model that connects them. Previous indications of $\sim 2\sigma$ tension from the less-precise measurements of H_0 and the CMB (Riess et al. 2011; Planck Collaboration et al. 2014) elicited a number of new studies, many of which were addressed above and helped improve the present analysis.

The analysis of the R11 dataset by Efstathiou (2014) yielded a value of $H_0 = 72.5 \pm 2.5$ km s^{-1} Mpc^{-1}, similar to the primary result of 73.0 ± 2.4 km s^{-1} Mpc^{-1} found by R11 using the same three anchors (MW, LMC, and NGC 4258, including the same H13 distance for NGC 4258 for both) and resulting in a 1.9σ tension with *Planck* and ΛCDM. Efstathiou (2014) also found $H_0 = 70.6 \pm 3.3$ km s^{-1} Mpc^{-1} with NGC 4258 as the *only* anchor, and the *Planck* team adopted this value instead of the three anchor result with its reduced precision and tension. The main difference in the analysis with R11 was the use of a global instead of $P–L$-specific outlier rejection. Our use here of $F814W - F160W$ colors to identify blends as discussed in §4.1 has significantly reduced the need for outlier rejection, and we have adopted a global outlier rejection for the 2% that remain. The internal model constraints on the slope and metallicity parameters have also improved substantially over the R11 dataset with no need for the priors set by R11 or Efstathiou (2014). We find the difference in H_0 between the use of three anchors and just NGC 4258 to be 0.6 km s^{-1} Mpc^{-1}, less than the 1.9 km s^{-1} Mpc^{-1} found by Efstathiou (2014) with the R11 dataset, a consequence of the tightened constraints on the Cepheid relations, and we conclude that use of the three anchors provides our best determination of H_0.

In the previous section we addressed systematic errors related to Cepheids and SNe used in our determination of H_0. A third component comes from our use of geometric distances to calibrate Cepheids. We used four sets: masers in NGC 4258, parallaxes to MW Cepheids, DEBs in the LMC, and DEBs in M31. The four values of H_0 using each as the sole anchor (see Table 6) are in good relative agreement, with none more than 1.5σ from the primary fit considering only their mean geometric distance error of 2.8%. Thus we see no basis for excluding any of these four as outliers.

Among the four, NGC 4258 has the advantage of a Cepheid sample with mean period closer to those in the SN hosts and with all their photometry on the same *HST* system.

However, in our analyses we parameterize the difference in zeropoints for non-*HST* data, and the *a posteriori* result of 0.013 mag for the primary fit is well below the estimated *a priori* constraint of $\sigma = 0.03$ mag, indicating no unexpected inconsistency with zeropoints. Our use of Cepheid samples in M31 and the LMC, which sample the short- and long-period range as well as the allowance in the fits for a P–L break, strictly limits the impact of a difference in sample mean periods on H_0. Our primary fit included offsets in the primary anchor distances of $\Delta\mu_{\rm N4258} = -0.044$, within the range of its 0.0568 mag prior, and $\Delta\mu_{\rm LMC} = -0.041$, within range of its 0.0452 mag prior. To be conservative, we removed M31 from the anchor set of our primary fit for the reasons discussed in §3.1.3 — but we discourage any *additional* winnowing or editing of the anchor set as it is unwarranted by the data and is likely to give a false sense of reducing the tension merely by inflating the present uncertainties.

We may consider whether the local determination of H_0 is different than the global (i.e., cosmological) value. In a homogeneous and isotropic Universe the two have the same expectation value. However, we live in an unusual place (a dark matter halo), and the inhomogeneity of matter on our measurement scale could lead to important variations in H_0. We currently account for flows induced by visible structures using host redshift corrections derived from a map of the matter density field calibrated by the IRAS PSCz catalogue (with a light-to-matter bias parameter of $\beta = 0.5$ and a dipole from Pike & Hudson 2005). This produces a small net increase in H_0 of a few tenths of a percent over the case of uncorrelated velocities at rest with respect to the CMB as discussed by R11. We also account for the cosmological change in expansion rate using q_0 and j_0 as discussed in §4.2. Because the Hubble diagram of SNe Ia is continuously sampled from $z = 0.01$ to $z = 2$, a percent-level change in the local expansion rate at $z > 0.15$ would be empirically evident in the distance residuals. In Figure 13 we show the relative change in H_0 starting at $0.0233 < z < 0.4$ and decreasing the influence of the local volume by gradually increasing the lower redshift cutoff for determining H_0. As shown, the value of H_0 never changes by more than the statistical uncertainty in the primary fit of 0.4% over a range of minimum $z = 0.02$ to 0.2.

Odderskov et al. (2016) *simulated* the effect of inhomogeneities on the local value of H_0 using mock sources in N-body simulations using the GADGET code with a box size of 700 Mpc and 512^3 dark matter particles with cosmological parameters in agreement with Planck Collaboration et al. (2014) from $z = 50$ to the present. In the simulation, halos are resolved using the halo-finder ROCKSTAR and realistic SN sampling is obtained from the redshift distribution of the samples with $0.01 < z < 0.1$. Cosmic variance is taken into account by varying the location of the observer. The uncertainty in the local measurement of H_0 is found to be 0.27% for the case of a typical SN sample, observer in a Local Group halo and the maximum redshift of $z = 0.15$ for our primary fit (Odderskov, priv. comm.). This analysis is in good agreement with our empirical result, which shows that such convergence to the sub-percent level has occurred within the SN sample at $z < 0.15$. We conclude that the uncertainty in H_0 owing to inhomogeneities is adequately taken into account

by the procedure of empirically correcting the redshifts for expected flows, testing for convergence of H_0 on large scales, and comparing the propagated uncertainty to simulations. A difference in H_0 at even the $> 1\%$ level caused by inhomogeneities would be triple the empirical or theoretical uncertainty and thus appears exceedingly unlikely.

Could the difference result from a systematic error in the *Planck* measurement? To explore this possibility, we consider an independent set of CMB data from the combination of WMAP9, ACT, and SPT observations. Based on the analysis by Calabrese et al. (2013) using ΛCDM but including the same neutrino mass of $0.06\,\mathrm{eV}$ used in the *Planck* analysis yields $H_0 = 70.9 \pm 1.6$ $\mathrm{km\,s^{-1}\,Mpc^{-1}}$, a difference from our local measurement of 0.9σ and thus quite consistent. While some of the improved agreement comes from the lower precision of this CMB dataset, most comes from a change in the central value of H_0 itself; the WMAP9+ACT+SPT value, even with the uncertainty of the *Planck* data, would still be consistent at the 1.3σ level. The difference in CMB datasets appears to play an important role in the perceived tension with the local value of H_0. Addison et al. (2015) has reported a parallel 2.5σ tension (size and significance) internally within the *Planck* data based on H_0 parameters determined from multipoles with $l < 1000$ and $l > 1000$, with the two halves of the data producing $H_0 = 69.7 \pm 1.7$ and 64.1 ± 1.7 $\mathrm{km\,s^{-1}\,Mpc^{-1}}$, respectively. Considering the two *Planck* halves with the R11 measurement of H_0, BAO, WMAP9, and SPT, Addison et al. (2015) finds 5 of the 6 consistent with $H_0 \approx 70$ $\mathrm{km\,s^{-1}\,Mpc^{-1}}$, with only the *Planck* $l > 1000$ data pulling toward significantly lower values. Because the SPT and *Planck* $l > 1000$ data cover similar ranges in l, their disagreement should be independent of the cosmological model and thus may indicate the presence of a systematic error and a role in the present tension with local H_0 measurements.

However, some degree of the previous tension remains, even without *Planck*, after including other datasets explicitly to constrain the cosmological model. Bennett et al. (2014) used WMAP9+ACT+SPT with BAO from BOSS DR11 and 6dFGS (their Table 2, column G) and find $H_0 = 69.3 \pm 0.7$ $\mathrm{km\,s^{-1}\,Mpc^{-1}}$, which has a 2.0σ tension with our determination of H_0 (and a 2σ tension with *Planck* in the other direction). A lower value of 68.1 ± 0.7 is given by Aubourg et al. (2015) for WMAP9, BAO, and high-redshift SNe — but this neglects SPT, which pulls toward higher H_0 (Addison et al. 2015; Story et al. 2013). More direct comparisons and analyses of CMB data may be expected to resolve the tensions between them and the local value of H_0.

It is useful to compare our result with recent measurements of the local Hubble constant which are *independent of SNe Ia*[6] and which appear to support a $\sim 5\%$ measurement. To avoid our own biases in identifying these we use current results from the four SN-independent projects shown in Figure 16 of Planck Collaboration et al. (2014): IR Tully-Fisher from Sorce et al. (2012), 2 strong lenses from Suyu et al. (2013), 4 distant maser systems from Gao et al. (2016), and 38 SZ clusters

---

[6]Other measurements of H_0 which also utilize SNe Ia do not provide a very meaningful comparison to ours because they are based on far fewer than the 18 reliable SN Ia calibrators presented here, such as Freedman et al. (2001) and Freedman et al. (2012) who both used 3 such SNe Ia and Sandage et al. (2006) who used 4 (see §1.1).

from Bonamente et al. (2006). These are plotted in Figure 12. A simple weighted average of these SN-independent measurements gives $H_0 = 73.4 \pm 2.6$ km s^{-1} Mpc^{-1}, nearly the same as our primary fit though with a 45% larger uncertainty. The most precise of these is from the analysis of two strong gravitational lenses and yields $H_0 = 75 \pm 4$ km s^{-1} Mpc^{-1} (Suyu et al. 2013), a result that is both independent of ours and has been reaffirmed by an independent lensing analysis (Birrer et al. 2015). Given the breadth of evidence that the local measurement of H_0 is higher than that inferred from the CMB and ΛCDM it is worthwhile to explore possible cosmological origins for the discrepancy.

We may consider the simplest extensions of ΛCDM which could explain a difference between a local and cosmological Hubble constant of $\sim$ 4–6 km s^{-1} Mpc^{-1}. We are not the first to look for such a resolution, though the roster of datasets examined has varied substantially and evolves as measurements improve (Wyman et al. 2014; Leistedt et al. 2014; Aubourg et al. 2015; Cuesta et al. 2015; Dvorkin et al. 2014). The simplest parameterizations of dark energy with $w_0 < -1$ or with $w_0 > -1$ and $w_a < 0$ can alleviate but not fully remove tension with H_0 (see Figure 12) due to support for $w(z) \sim -1$ signal from high-redshift SNe Ia and BAO (Cuesta et al. 2015; Aubourg et al. 2015) (see Figure 14). A very recent ($z < 0.03$) and dramatic decrease in w or an episode of strong dark energy at $3 < z < 1000$ may evade detection and still produce a high value of H_0. Whether such a model creates additional tensions will depend on its prescription and still, if empirically motivated, is likely to suffer from extreme fine-tuning.

A synthesis of the studies cited above indicates a more fruitful avenue is found in the "dark radiation" sector. An increase in the number of relativistic species (dark radiation; e.g., neutrinos) in the early Universe increases the radiation density and expansion rate during the radiation-dominated era, shifting the epoch of matter-radiation equality to earlier times. The resulting reduction in size of the sound horizon (which is used as a standard ruler for the CMB and BAO) by a few percent for one additional species ($N_{eff} = 4$) increases H_0 by about 7 km s^{-1} Mpc^{-1} for a flat Universe, more than enough to bridge the divide between the local and high-redshift scales. A fractional increase (i.e., less than unity) is also quite plausible for neutrinos of differing temperatures or massless bosons decoupling before muon annihilation in the early Universe (e.g., Goldstone bosons; Weinberg 2013), producing $\Delta N_{eff} = 0.39$ or 0.57 depending on the decoupling temperature. An example of such a fit comes from Aubourg et al. (2015) using a comprehensive set of BAO measurements and *Planck* data, finding $N_{eff} = 3.43 \pm 0.26$ and $H_0 = 71 \pm 1.7$ km s^{-1} Mpc^{-1}. A similar result from WMAP9+SPT+ACT+SN+BAO gives $N_{eff} = 3.61 \pm 0.6$ and $H_0 = 71.8 \pm 3.1$ km s^{-1} Mpc^{-1} (Hinshaw et al. 2013). Thus, a value of ΔN_{eff} in the range 0.4–1.0 would relieve some or all of the tension. Although fits to the current *Planck* dataset (Planck Collaboration et al. 2015) do not indicate the presence of such additional radiation, they do not exclude this full range either.

Allowing the N_{eff} degree of freedom triples the uncertainty in the cosmological value of H_0 from Planck Collaboration et al. (2015), BAO and high-redshift SNe and modestly raises its value to $H_0 = 68 \pm 1.6$ km s^{-1} Mpc^{-1}, reducing the tension to 2.1σ and demonstrating that a local measurement of H_0 appears to offer a powerful aid to determining N_{eff}.

Including the present measurement of H_0 with the *Planck* (Planck Collaboration et al. 2015) PLIK+TT+TEB+lensing data, the full BAO set of measurements (including the Lyman-alpha QSO's) and the Betoule et al. (2014) SN sample pulls N_{eff} higher to a value of 3.41 ± 0.22 (and $H_0 = 70.4 \pm 1.2 \mathrm{\ km\,s^{-1}\,Mpc^{-1}}$), a result favoring (though not requiring) additional dark radiation. This fit provides the lowest value of the best-fit log likelihood among standard extensions to ΛCDM we considered (lower than ΛCDM by ~ 2) and the result is shown in Figure 15. If *Planck* CMB, BAO, SN, and H_0 data are taken at face value, this extension of ΛCDM remains an intriguing avenue toward their resolution and highlights the need for additional improvements in local determinations of H_0. More broadly, the present discrepancy in the measured Hubble constant may provide a clue to one of the many enigmas contained in the 95% of the Universe within the dark sector.

Fortunately, the prospects for near-term improvements in the local determination of the Hubble constant are quite promising. We have begun obtaining a new sample of parallax measurements of long-period MW Cepheids using the spatial scanning technique with WFC3 on *HST* (Riess et al. 2014; Casertano et al. 2015). These improvements alone would reduce the total uncertainty in H_0 to $\sim 1.8\%$ based on the terms in Table 7. In a parallel effort, we are obtaining spatial-scan photometry of a larger sample of MW Cepheids slated for even higher-precision *Gaia* parallax determinations in a few years. With additional progress from this route and others, the goal of 1% (Suyu et al. 2012) is not far-fetched and has the potential, in concert with Stage-IV CMB experiments (see Figure 16), to provide new leverage on the dark Universe.

A. Setup of System of Equations

Equations 1 through 8 describe the relationships between the measurements and parameters with additional constraint equations given in §3. To improve clarity we explicitly show the system of equations we solve to derive the value of M_B^0 which together with the independent determinationf of a_B provides the measurement of H$_0$ via Equation 9. Here we refer to the vector of measurements as **y**, the free parameters as **q**, the equation (or design) matrix as **L**, and the error matrix as **C** with $\chi^2 = (y - Lq)^T C^{-1}(y - Lq)$ and maximum likelihood parameters given as $q_{best} = (L^T C^{-1} L)^{-1} L^T C^{-1} y$ and covariance matrix $(L^T C^{01} L)^{-1}$. For the primary fit which uses 3 anchors, NGC 4258, Milky Way parallaxes, and LMC DEBs we arrange **L**, **C** and **q** as given below so that some terms are fully correlated across a set of measurements like the anchor distances for NGC 4258 and the LMC and ground-to-HST zeropoint errors are fully correlated and others like the MW parallax distances are not.

$$
y = \begin{pmatrix}
m_{H,1,j}^W \\
.. \\
m_{H,18,j}^W \\
m_{H,j,N4258}^W - \mu_{0,N4258} \\
m_{H,M31,j}^W \\
m_{H,MW,j}^W - \mu_{\pi,j} \\
m_{H,LMC,j}^W - \mu_{0,LMC} \\
m_{B,1}^0 \\
.. \\
m_{B,18}^0 \\
0 \\
0 \\
0
\end{pmatrix}
$$

$$
l = \begin{pmatrix}
1 & .. & 0 & 0 & 1 & 0 & 0 & \log P_{18,1}^h/0 & 0 & [\text{O/H}]_{18,1} & 0 & \log P_{18,1}^l/0 \\
.. & .. & .. & .. & .. & .. & .. & .. & .. & .. & .. & .. \\
0 & .. & 1 & 0 & 1 & 0 & 0 & \log P_{18,j}^h/0 & 0 & [\text{O/H}]_{18,j} & 0 & \log P_{18,j}^l/0 \\
0 & .. & 0 & 1 & 1 & 0 & 0 & \log P_{N4258,j}^h/0 & 0 & [\text{O/H}]_{N4258,j} & 0 & \log P_{N4258,j}^l/0 \\
0 & .. & 0 & 0 & 1 & 0 & 1 & \log P_{M31,j}^h/0 & 0 & [\text{O/H}]_{M31,j} & 0 & \log P_{M31,j}^l/0 \\
0 & .. & 0 & 0 & 1 & 0 & 0 & \log P_{MW,j}^h/0 & 0 & [\text{O/H}]_{MW,j} & 1 & \log P_{MW,j}^l/0 \\
0 & .. & 0 & 0 & 1 & 1 & 0 & \log P_{LMC,j}^h/0 & 0 & [\text{O/H}]_{MW,j} & 1 & \log P_{LMC,j}^l/0 \\
1 & .. & 0 & 0 & 0 & 0 & 0 & 0 & 1 & 0 & 0 & 0 \\
0 & .. & 1 & 0 & 0 & 0 & 0 & 0 & 1 & 0 & 0 & 0 \\
0 & .. & 0 & 0 & 0 & 0 & 0 & 0 & 0 & 0 & 1 & 0 \\
0 & .. & 0 & 1 & 0 & 0 & 0 & 0 & 0 & 0 & 0 & 0 \\
0 & .. & 0 & 0 & 0 & 1 & 0 & 0 & 0 & 0 & 0 & 0
\end{pmatrix}
$$

$$q = \begin{pmatrix} \mu_{0,1} \\ .. \\ \mu_{0,18} \\ \Delta\mu_{\mathrm{N4258}} \\ M_{H,1}^{W} \\ \Delta\mu_{\mathrm{LMC}} \\ \mu_{M31} \\ b \\ M_{B}^{0} \\ Z_{W} \\ \Delta\mathrm{zp} \\ b_{l} \end{pmatrix}$$

$$C = \begin{pmatrix}
\sigma_{\mathrm{tot},1,j}^2 & .. & 0 & 0 & 0 & 0 & 0 & 0 & .. & 0 & 0 & 0 & 0 \\
.. & .. & .. & .. & .. & .. & .. & .. & .. & .. & .. & .. & .. \\
0 & .. & \sigma_{\mathrm{tot},18,j}^2 & 0 & 0 & 0 & 0 & 0 & .. & 0 & 0 & 0 & 0 \\
0 & .. & 0 & \sigma_{\mathrm{tot},N4258,j}^2 & 0 & 0 & 0 & 0 & .. & 0 & 0 & 0 & 0 \\
0 & .. & 0 & 0 & \sigma_{\mathrm{tot},M31,j}^2 & 0 & 0 & 0 & .. & 0 & 0 & 0 & 0 \\
0 & .. & 0 & 0 & 0 & \sigma_{\mathrm{tot},MW,j}^2+\sigma_{\pi,j}^2 & 0 & 0 & .. & 0 & 0 & 0 & 0 \\
0 & .. & 0 & 0 & 0 & 0 & \sigma_{\mathrm{tot},LMC,j}^2 & 0 & .. & 0 & 0 & 0 & 0 \\
0 & .. & 0 & 0 & 0 & 0 & 0 & \sigma_{m_B,1}^2 & .. & 0 & 0 & 0 & 0 \\
.. & .. & .. & .. & .. & .. & .. & .. & .. & .. & .. & .. & .. \\
0 & .. & 0 & 0 & 0 & 0 & 0 & 0 & .. & \sigma_{m_B,18}^2 & 0 & 0 & 0 \\
0 & .. & 0 & 0 & 0 & 0 & 0 & 0 & .. & 0 & \sigma_{\mathrm{zp}}^2 & 0 & 0 \\
0 & .. & 0 & 0 & 0 & 0 & 0 & 0 & .. & 0 & 0 & \sigma_{\mu,N4258}^2 & 0 \\
0 & .. & 0 & 0 & 0 & 0 & 0 & 0 & .. & 0 & 0 & 0 & \sigma_{\mu,\mathrm{LMC}}^2
\end{pmatrix}$$

Note: The term $\log P_{18,1}^{h}/0$ equals $\log P_{18,1}$ if $P > 10$ d or 0 if $P < 10$ d. The term $\log P_{18,1}^{l}/0$ equals $\log P_{18,1}$ if $P < 10$ d or 0 if $P > 10$ d.
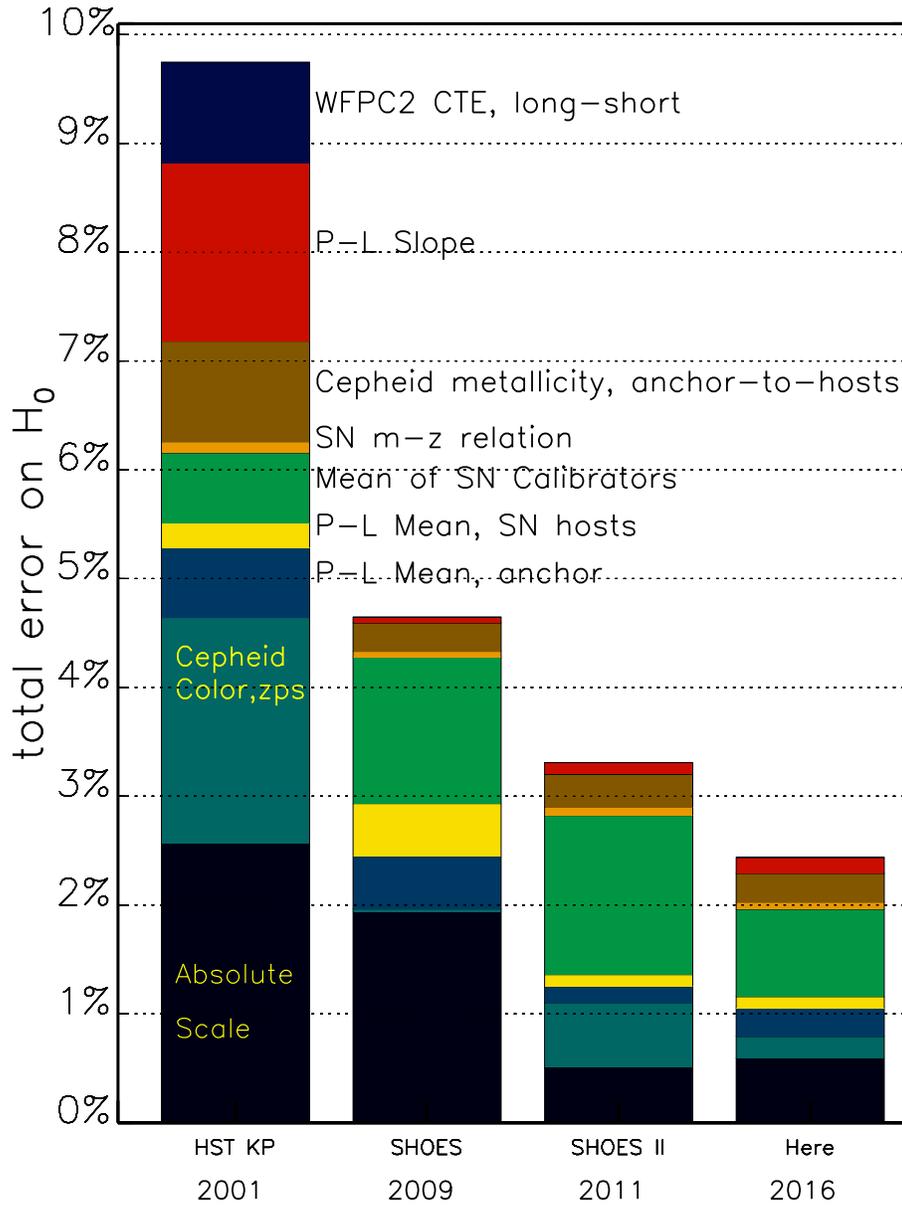
Fig. 1.— Uncertainties in the determination of H_0. Uncertainties are squared to show their individual contribution to the quadrature sum. These terms are given in Table 7.
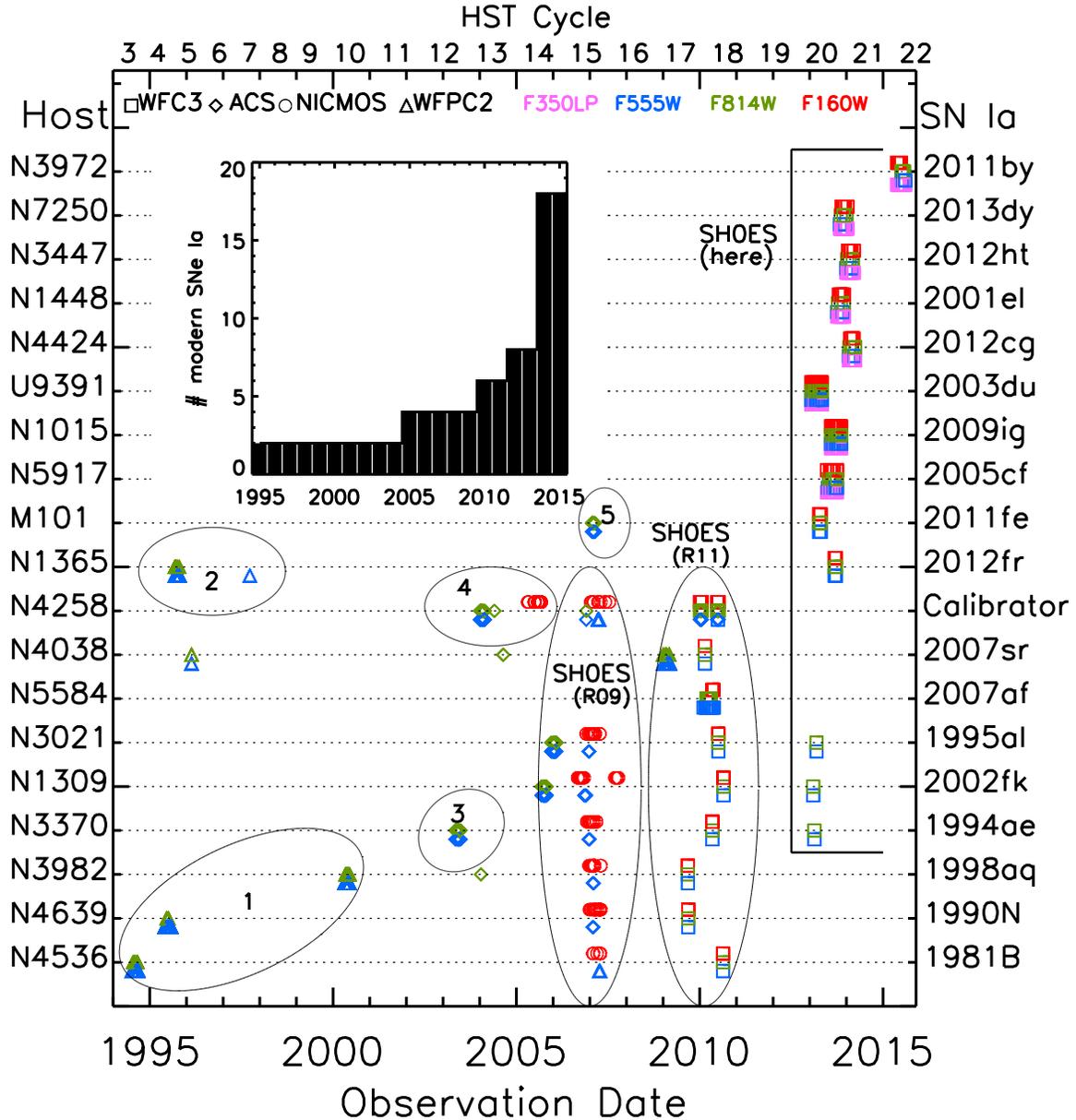
Fig. 2.— *HST* observations of the host galaxies of ideal SNe Ia. The data used to observe Cepheids in 18 SN Ia hosts and NGC 4258 have been collected over 20 years with 4 cameras and over 600 orbits of *HST* time. Sixty 90-day campaigns in *F555W* and *F814W* or in *F350LP* were used to identify Cepheids from their light curves with occasional reobservations years later to identify Cepheids with $P > 60$ days. Near-IR follow-up observations in *F160W* are used to reduce the effects of host-galaxy extinction, sensitivity to metallicity, and breaks in the *P–L* relation. Data sources: (1) *HST* Key Project, Freedman et al. (2001); (2) *HST* SN Ia Calibration Project, Sandage et al. (2006); (3) Riess et al. (2005); (4) Macri et al. (2006); and (5) Mager et al. (2013).
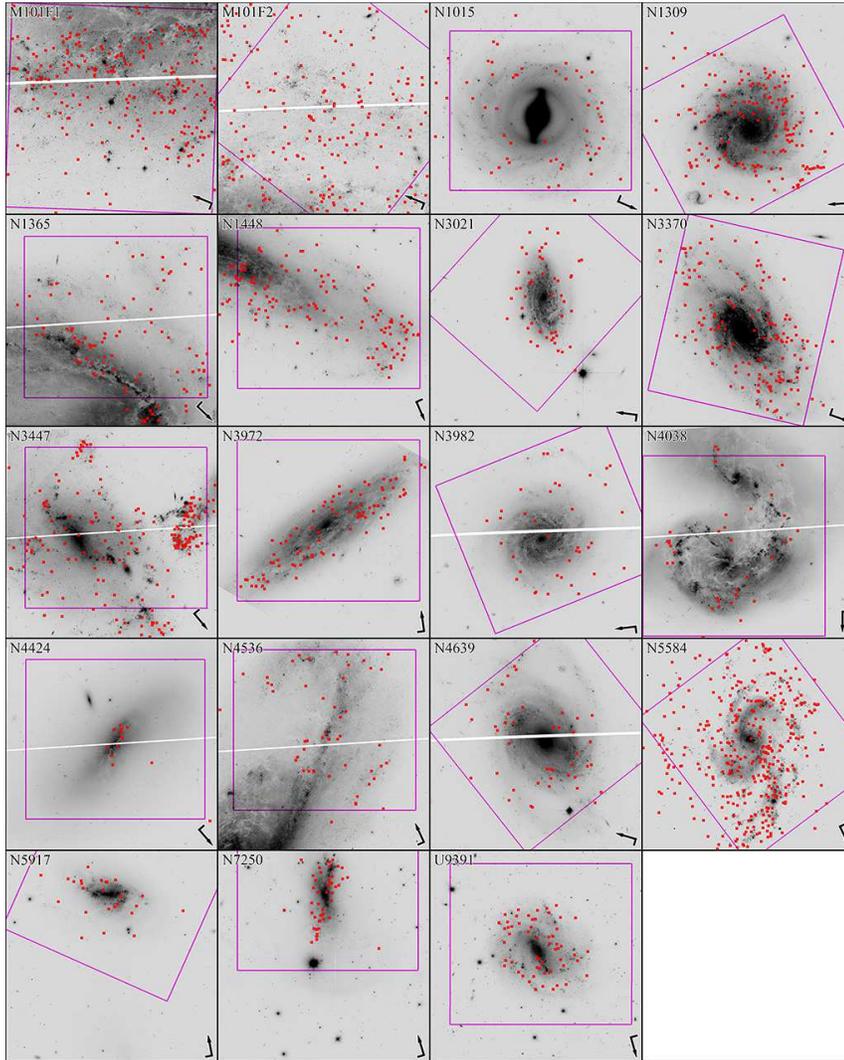
Fig. 3.— Images of Cepheid hosts. Each image is of the Cepheid host indicated. The magenta outline shows the $2.7' \times 2.7'$ field of the WFC3/IR observations. Red dots indicate the positions of the Cepheids. Compass indicates North (long axis) and East (short axis).
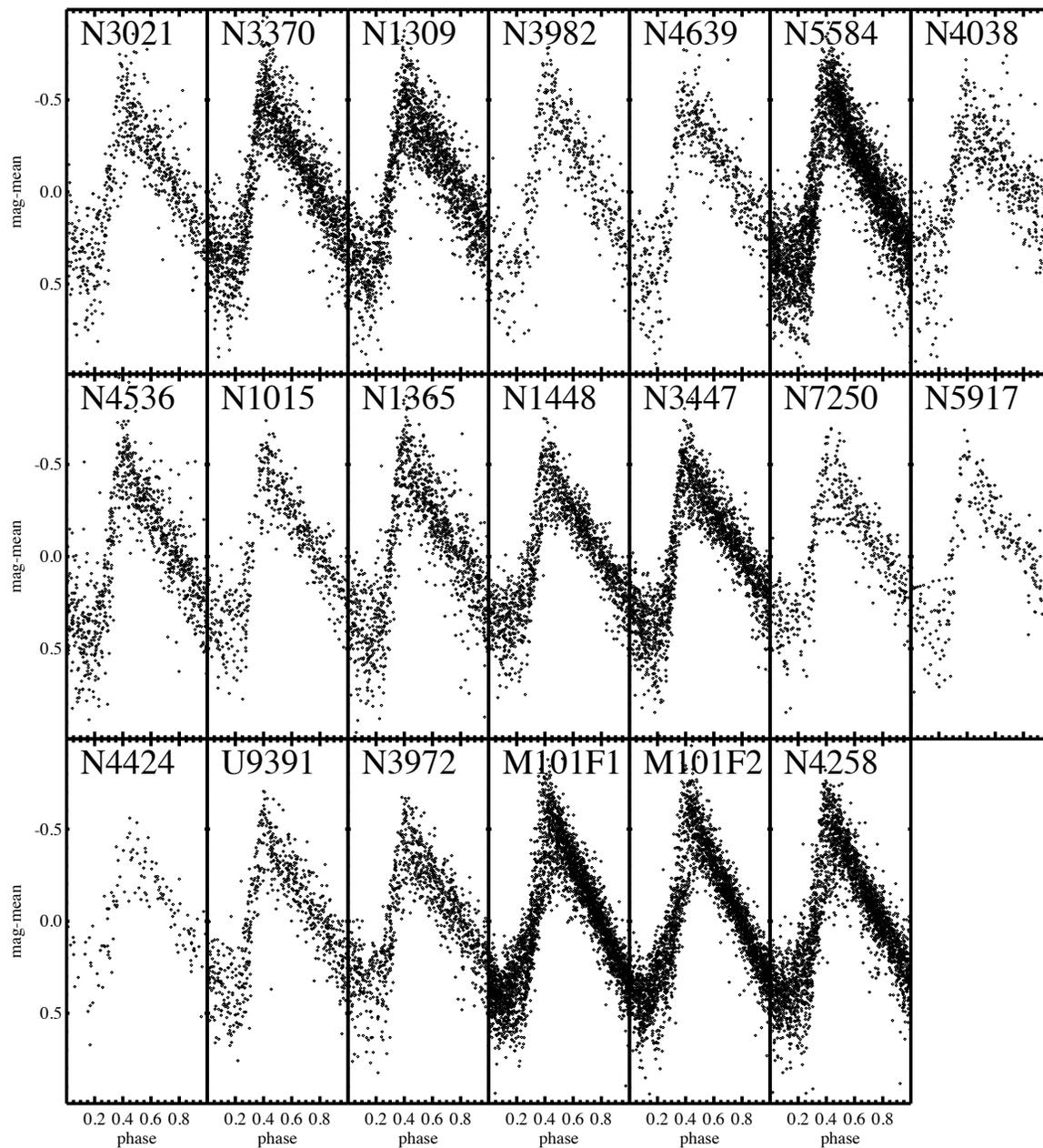
Fig. 4.— Composite visual ($F555W$) or white-light ($F350LP$) Cepheid light curves. Each *HST* Cepheid light curve with $10 < P < 80$ days is plotted after subtracting the mean magnitude and determining the phase of the observation. Two fields (F1 and F2) are shown for M101.
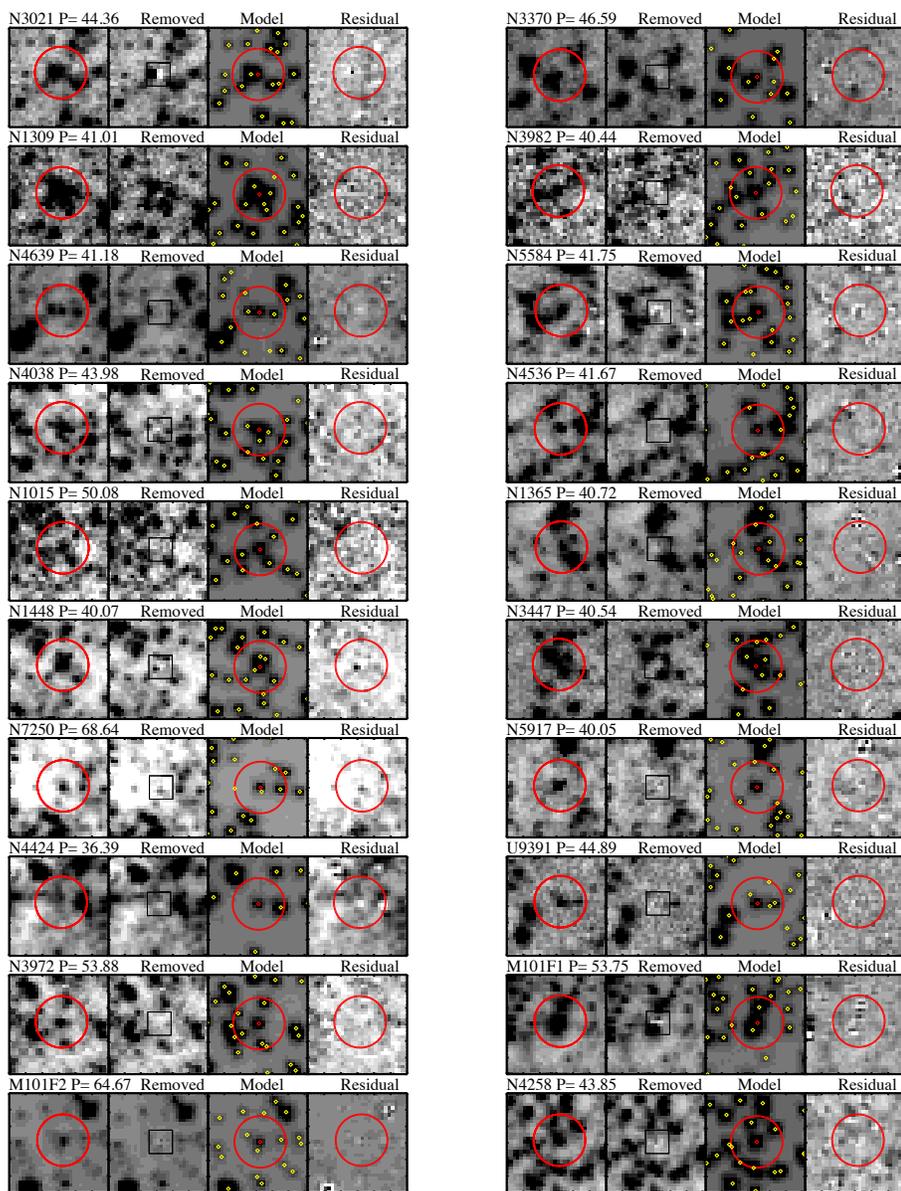
Fig. 5.— Example WFC3 $F160W$ Cepheid scene model for each host. A random Cepheid in the period range of $30 < P < 70$ days was selected. The four panels of each host show a $1''$ region of the scene around each known Cepheid, the region after the Cepheid is fit and subtracted, the model of all detected sources, and the model residuals.
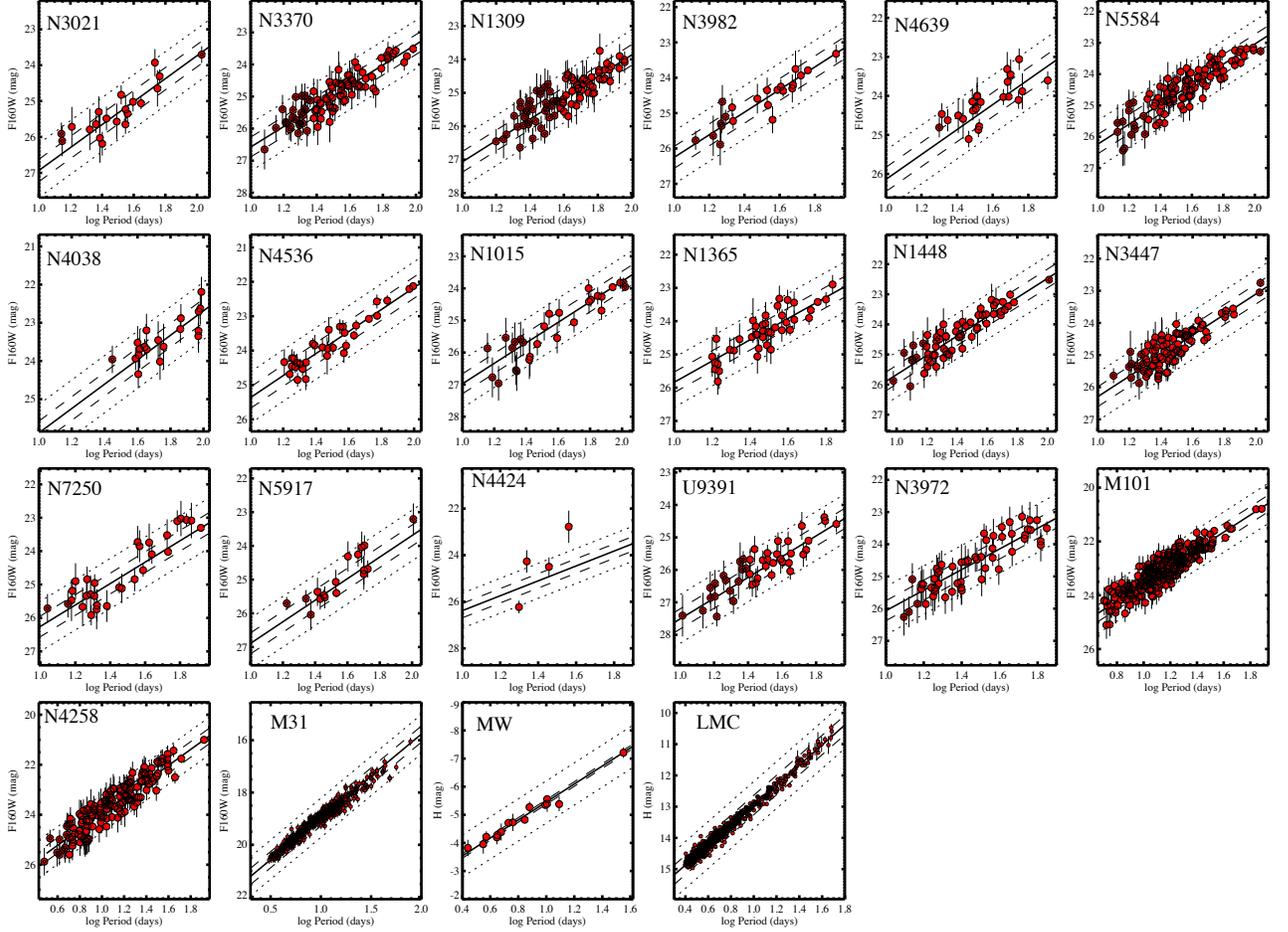
Fig. 6.— Near-infrared Cepheid P–L relations. The Cepheid magnitudes are shown for the 18 SN hosts and the 4 distance-scale anchors. Magnitudes labeled as $F160W$ are all from the same instrument and camera, WFC3 $F160W$. The uniformity of the photometry and metallicity reduces systematic errors along the distance ladder. A single slope is shown to illustrate the relations, but we also allow for a break (two slopes) as well as limited period ranges.
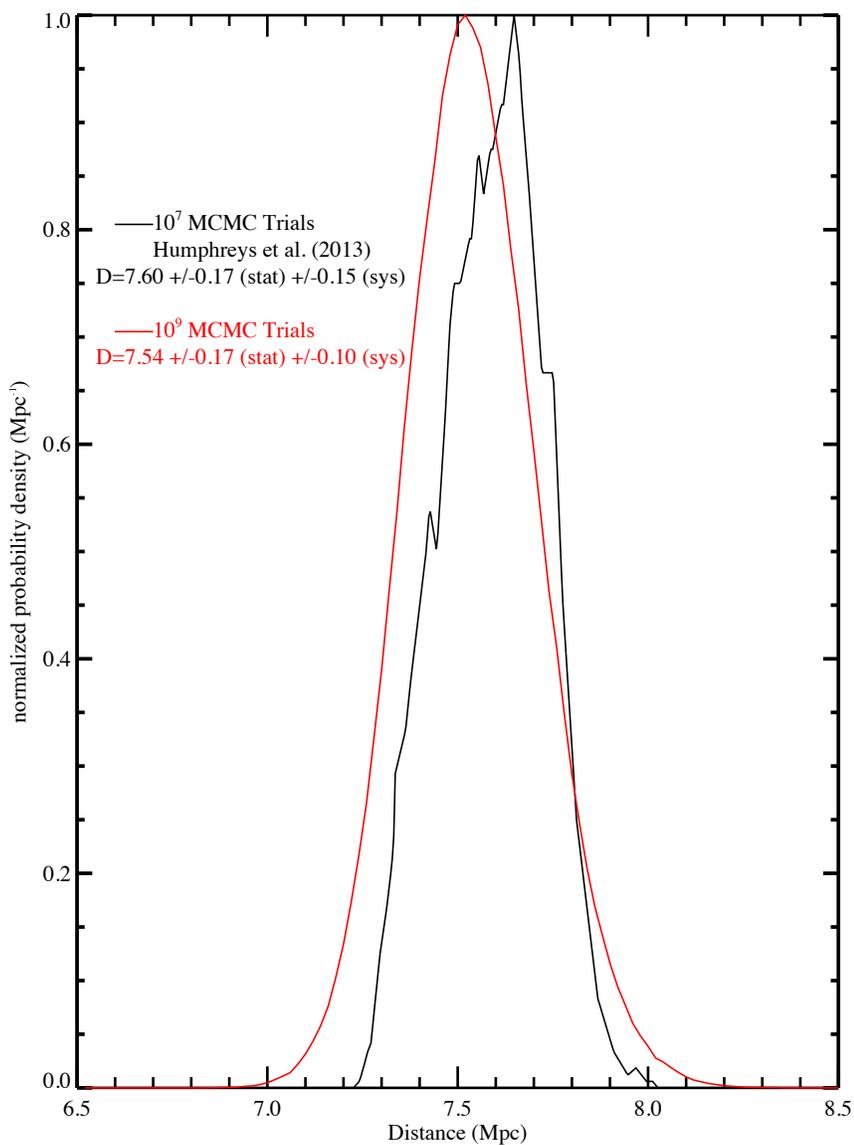
Fig. 7.— Normalized probability density function (PDF) for the maser-based distance to NGC 4258. The curve in black shows the PDF for the distance to NGC 4258 based on the same multiparameter fit of the maser data in NGC 4258 from Humphreys et al. (2013). With a 100-fold increase (red curve) in the MCMC sampling, we have reduced the 1.5% systematic error in distance from Humphreys et al. (2013), which reflected different results with differing initial conditions using more-limited MCMC sampling of the parameter space.
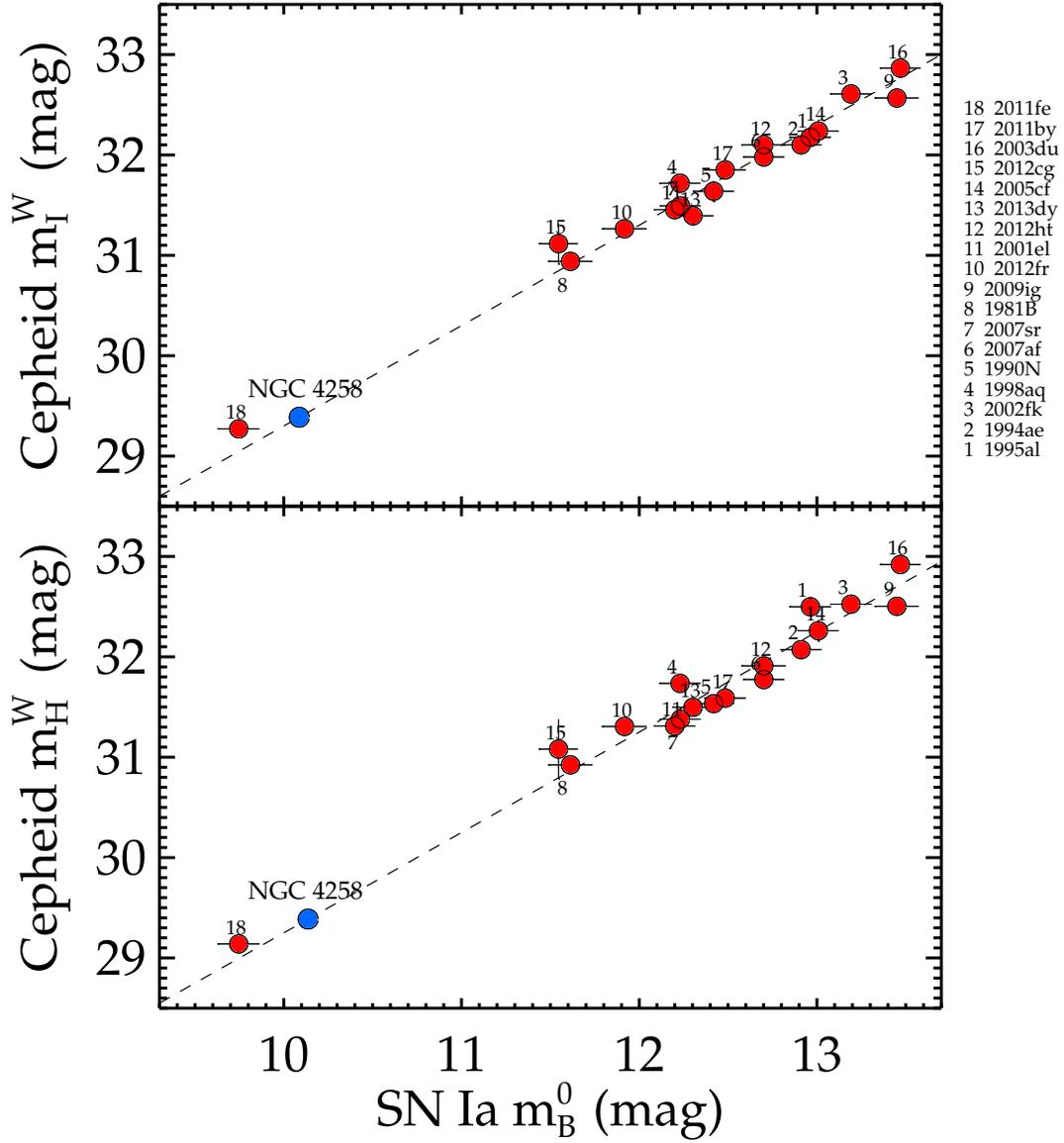
Fig. 8.— Relative distances from Cepheids and SNe Ia. The top and bottom panels show relative distances for 18 hosts determined from their SNe Ia and Cepheid Wesenheit optical and NIR magnitudes, respectively. The Cepheid result for each host is an approximated distance derived after removing that host's SN Ia data from the full global fit for H_0. The relative dispersions are 0.11 mag (top) and 0.15 mag (bottom). The maser-calibrated Cepheid distance to NGC 4258 is indicated as well as the model-fit SN Ia magnitude it would host.
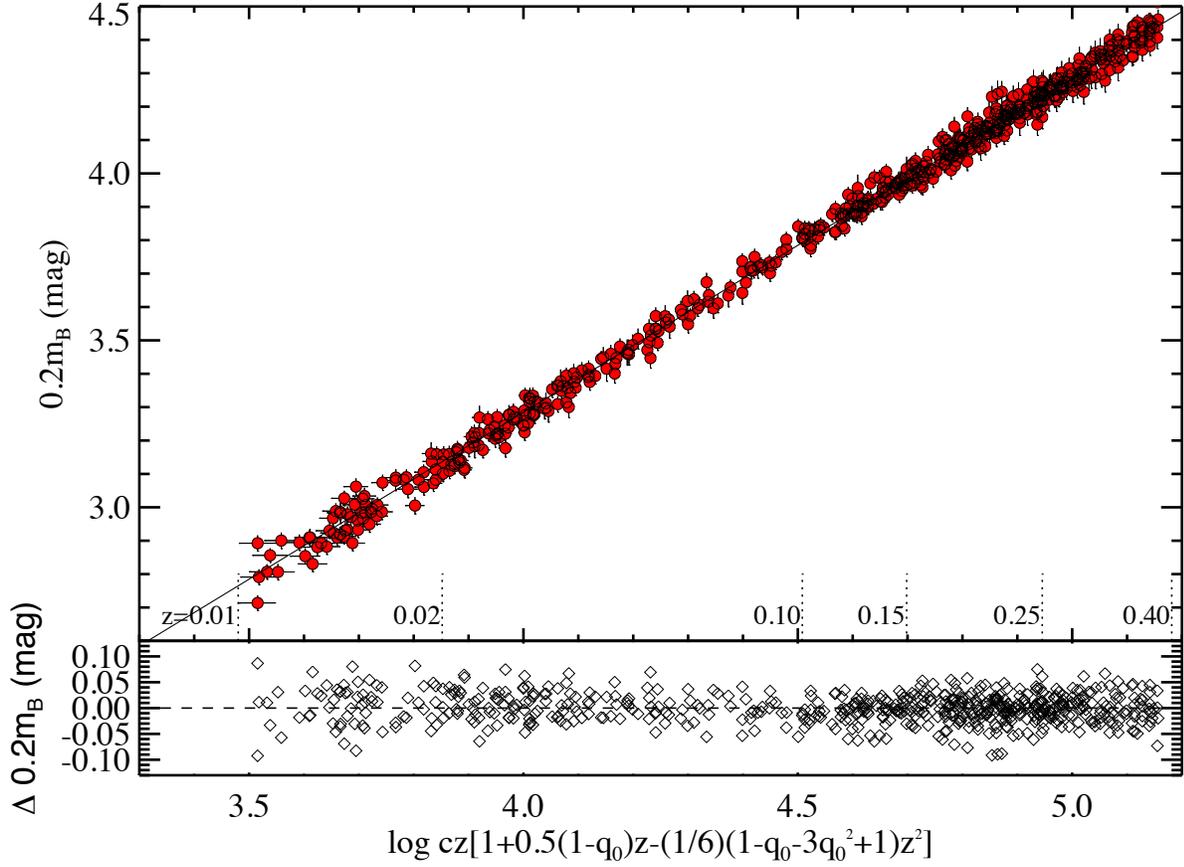
Fig. 9.— Hubble diagram of more than 600 SNe Ia at $0.01 < z < 0.4$ in units of $logcz$. Measurements of distance and redshift for a compilation of SN Ia data as described by Scolnic et al. (2015). These data are used to determine the intercept, a_X (see Equation 5) where $logcz=0$, which helps measure the value of the Hubble constant as given in Equation 9). We account for changes in the cosmological parameters empirically by including the kinematic terms, q_0 and j_0, measured between high- and low-redshift SNe Ia. The intercept is measured using variants of this redshift range, as discussed in the text, with the primary fit at $0.0233 < z < 0.15$.
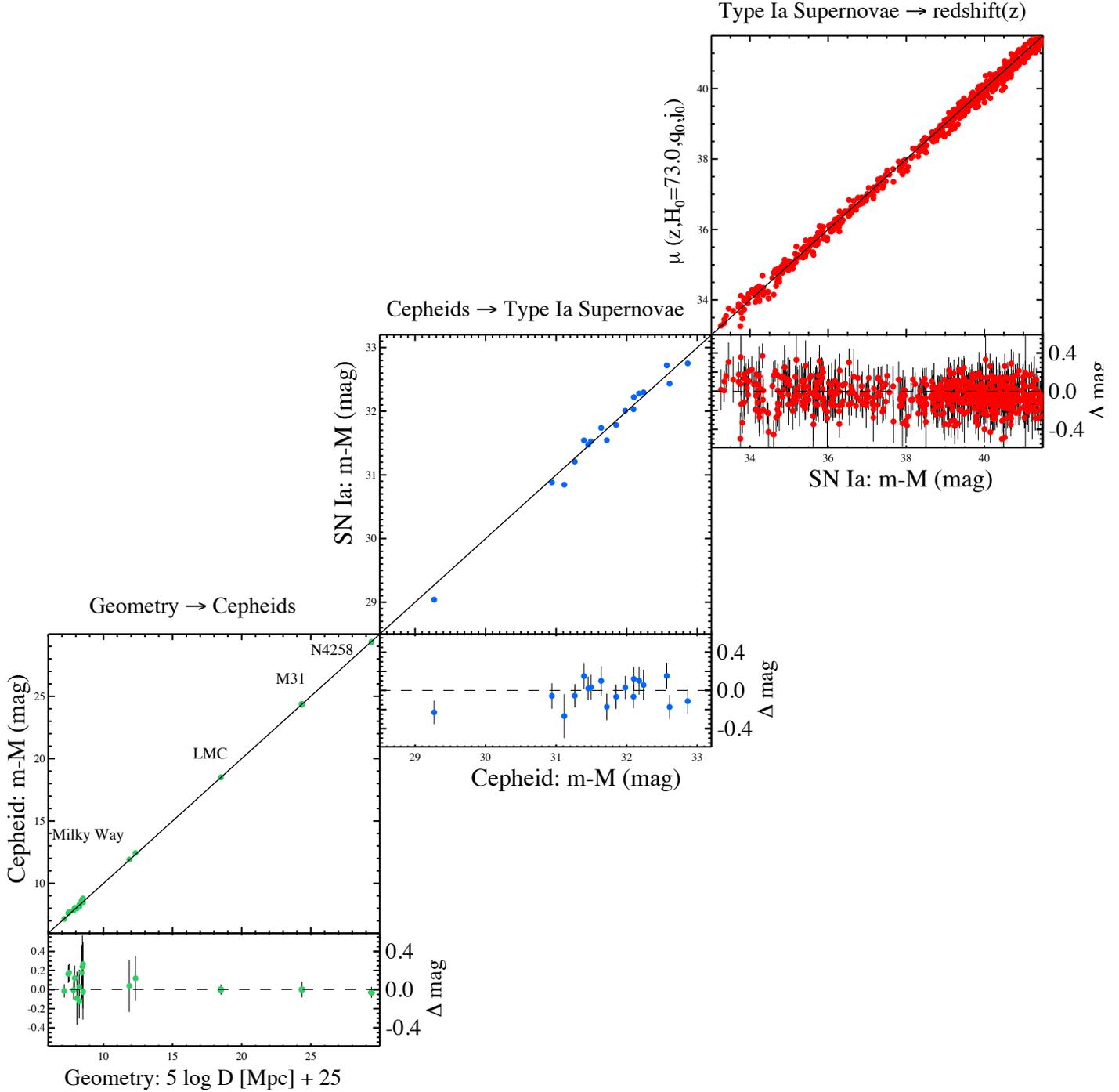
Fig. 10.— Complete distance ladder. The simultaneous agreement of pairs of geometric and Cepheid-based distances (lower left), Cepheid and SN Ia-based distances (middle panel) and SN and redshift-based distances provides the measurement of the Hubble constant. For each step, geometric or calibrated distances on the X-axis serve to calibrate a relative distance indicator on the Y-axis through the determination of M or H_0. Results shown are an approximation to the global fit as discussed in the text.
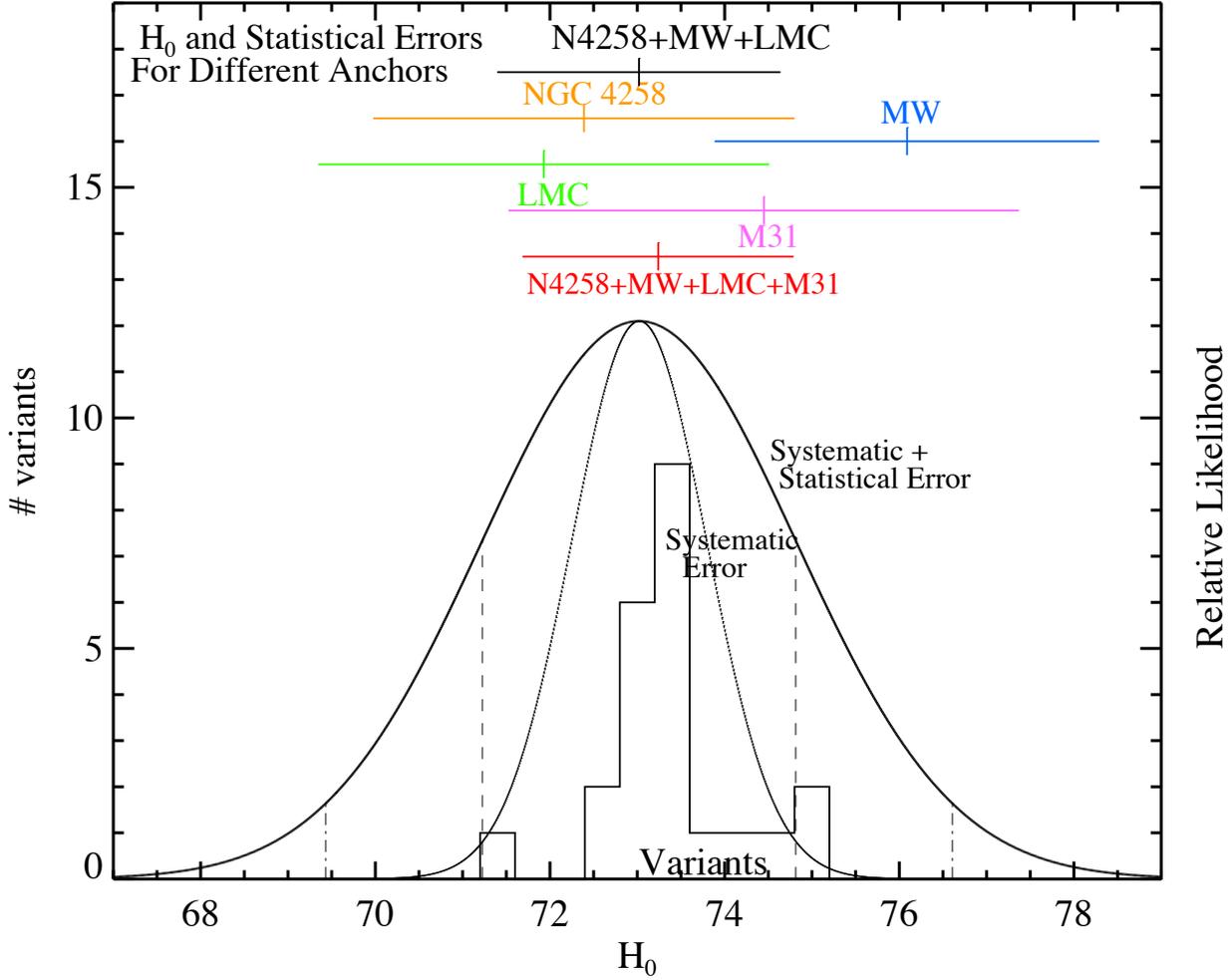
Fig. 11.— Determination of systematic errors in H_0 for the primary fit anchor set (N4258,MW,LMC). By varying factors outside the global fit and its parameters such as the assumed reddening law, its parameters, the presence of a metallicity dependence, the presence of breaks in the P–L relations, selection of SN light curve fitter, morphology or local star formation rate of hosts, etc. We derive a systematic error from a Gaussian fit to the variants. This error is smaller than the indicated statistical errors.
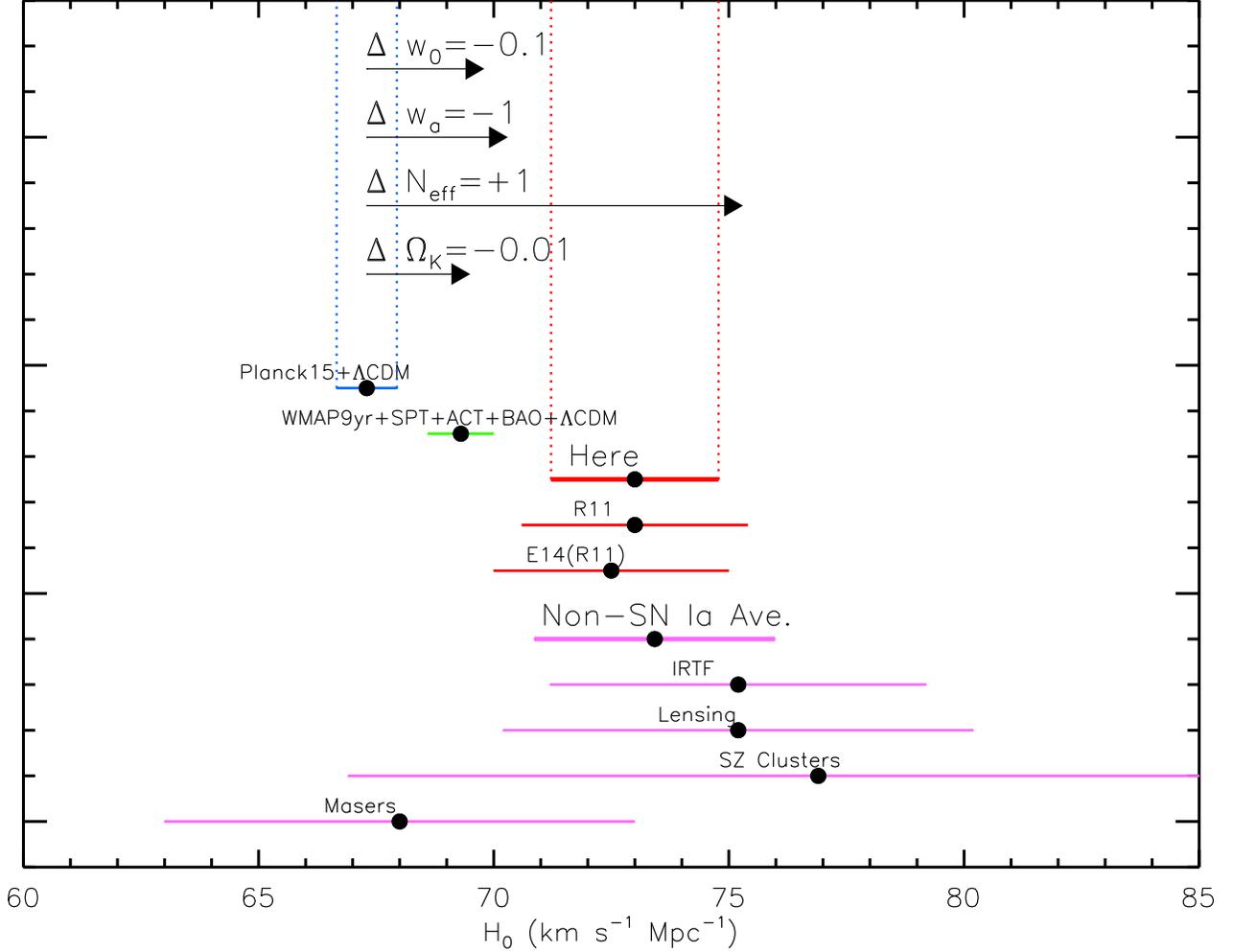
Fig. 12.— Local measurements of H_0 compared to values predicted by CMB data in conjunction with ΛCDM. We show 4 SN Ia-independent values selected for comparison by Planck Collaboration et al. (2014) and their average, the primary fit from R11, its reanalysis by Efstathiou (2014) and the results presented here. The 3.0σ difference between *Planck*+ΛCDM and our result motivates the exploration of extensions to ΛCDM.
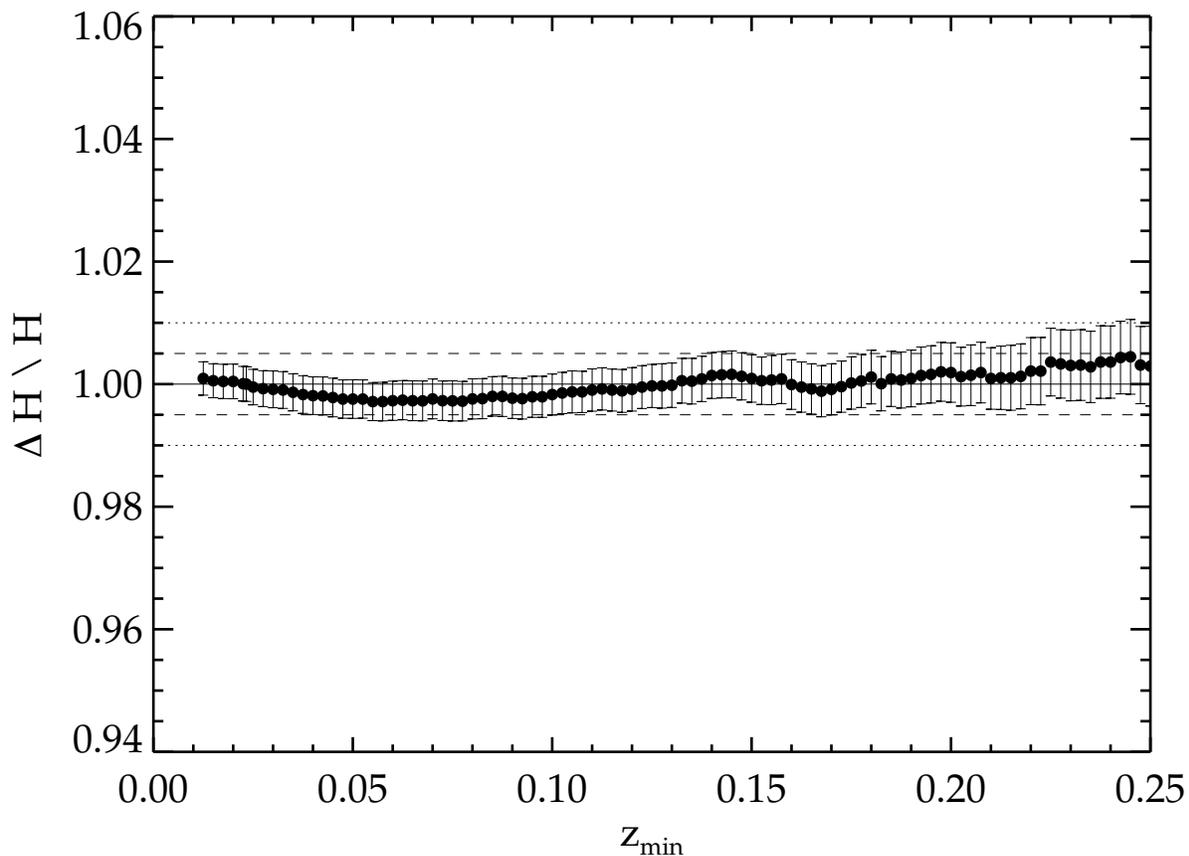
Fig. 13.— Fractional variation in H_0 resulting from a progressively higher redshift (lower cosmic variance) range used to measure the Hubble expansion, $z_{min} < z < 0.4$. Empirically increasing z_{min} from 0.0233 (primary fit) to 0.25 produces variations consistent with the measurement uncertainty of ± 0.004 and the simulated uncertanty of ± 0.0027 from Odderskov et al. (2016). Thus a difference between the local and global H_0 of even $\sim 1\%$ is exceedingly unlikely.
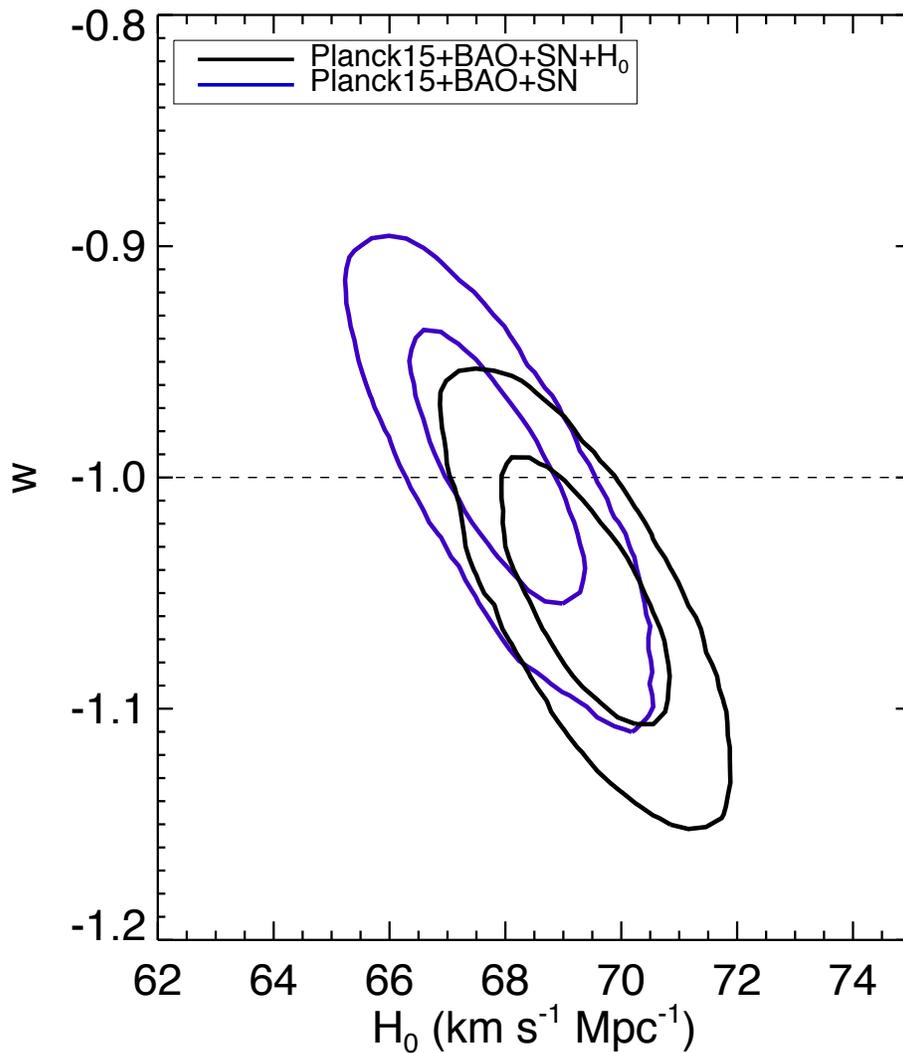
Fig. 14.— Confidence regions determined with CosmoMC based on the data from Planck (TT+TEB+lensing), BAO including Lyα QSOs, the JLA SN sample (Betoule et al. 2014) and with and without our determination of H_0 for the wCDM cosmological model. As shown there is a degeneracy between w and H_0 and the local measurement of H_0 pulls the solution to a lower value of w though it is still consistent with -1.
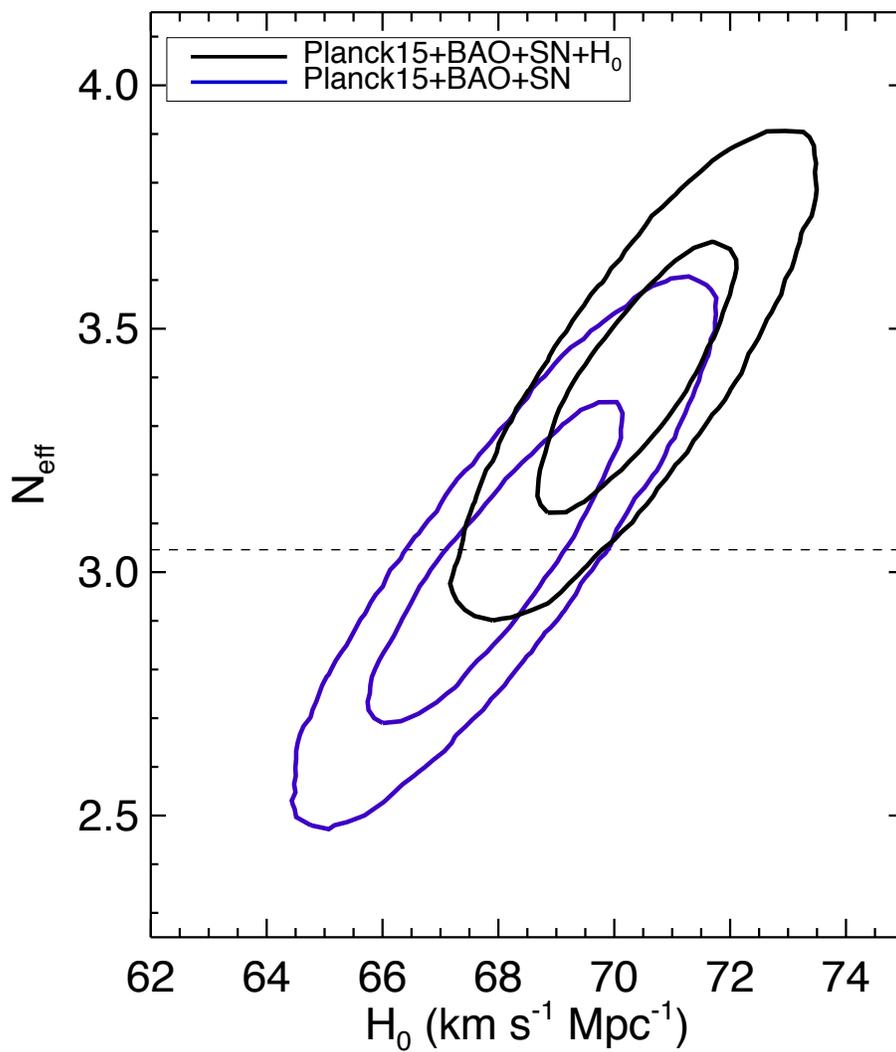
Fig. 15.— Same as Figure 14 but for the N_{eff}CDM model. The local measurement of H_0 pulls the solution towards $N_{eff} > 3.046$ which also provides a marginally better fit to the full data set than ΛCDM.
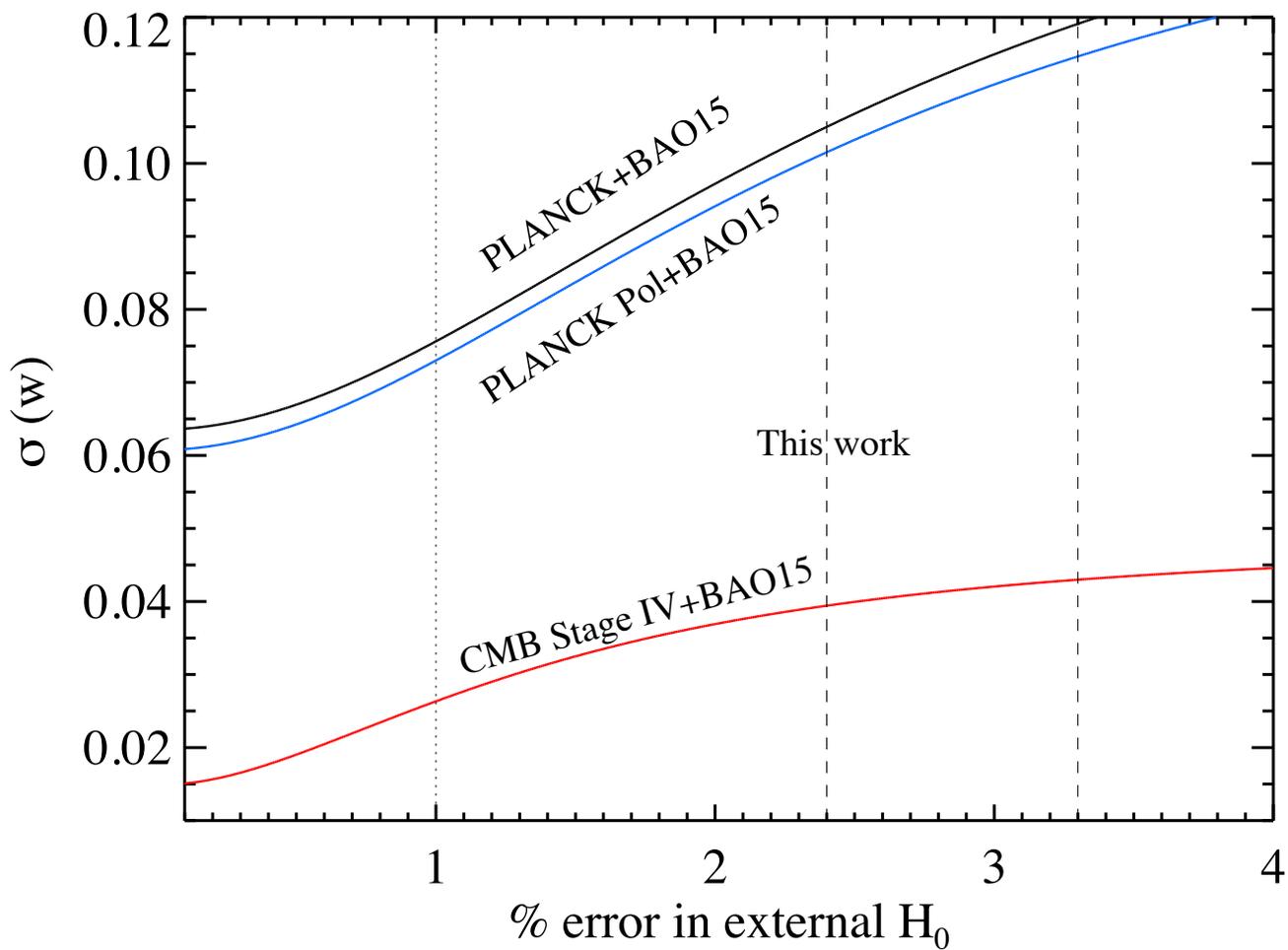
Fig. 16.— Constraint in the dark energy equation of state as a function of the precision of the local determination of the Hubble constant. Past and current precision is indicated as well as a future goal of 1%.

Table 8. Fits for H$_0$

| χ^2_{dof}	H_0	Anc	Brk	Clp	σ	Opt	PL	R	R_V	N	Z	γ	b	bl	SN	z_m	M_V^0	a_v	Gal
0.94	73.24 1.55	All	Y	1	2.7	Y	W_H	F	3.3	2158	Z	-0.13 0.07	-3.26 0.02	-3.24 0.01	S	0.02	-19.25	0.712	A
0.95	73.36 1.56	All	Y	G	2.7	Y	W_H	F	3.3	2160	Z	-0.11 0.07	-3.26 0.02	-3.24 0.01	S	0.02	-19.24	0.712	A
0.90	72.61 1.52	All	Y	I	2.7	Y	W_H	F	3.3	2160	Z	-0.08 0.07	-3.31 0.02	-3.21 0.01	S	0.02	-19.26	0.712	A
1.31	73.58 1.82	All	Y	G	No	Y	W_H	F	3.3	2224	Z	-0.08 0.08	-3.26 0.02	-3.23 0.02	S	0.02	-19.24	0.712	A
1.12	73.57 1.69	All	Y	G	3.5	Y	W_H	F	3.3	2200	Z	-0.13 0.07	-3.25 0.02	-3.24 0.01	S	0.02	-19.24	0.712	A
1.11	73.54 1.68	All	Y	1	3.5	Y	W_H	F	3.3	2199	Z	-0.13 0.07	-3.25 0.02	-3.24 0.01	S	0.02	-19.24	0.712	A
0.95	72.53 1.55	All	Y	I	3.5	Y	W_H	F	3.3	2199	Z	-0.08 0.07	-3.30 0.02	-3.22 0.01	S	0.02	-19.27	0.712	A
1.13	73.12 1.69	All	Y	G	3.5	Y	W_H	F	2.5	2201	Z	-0.13 0.07	-3.25 0.02	-3.24 0.01	S	0.02	-19.25	0.712	A
0.94	73.92 1.56	All	Y	G	2.7	Y	W_H	C	3.3	2158	Z	-0.10 0.07	-3.27 0.02	-3.26 0.01	S	0.02	-19.23	0.712	A
0.97	73.13 1.57	All	Y	G	2.7	Y	W_H	N	3.3	2159	Z	-0.10 0.07	-3.24 0.02	-3.23 0.01	S	0.02	-19.25	0.712	A
0.95	73.47 1.55	All	N	G	2.7	Y	W_H	F	3.3	2161	Z	-0.11 0.07	-3.25 0.01	. . .	S	0.02	-19.24	0.712	A
1.19	72.00 1.77	All	10	G	2.7	Y	W_H	F	3.3	1183	Z	-0.16 0.08	-3.26 0.03	. . .	S	0.02	-19.28	0.712	A
0.93	73.31 1.54	All	60	G	2.7	Y	W_H	F	3.3	2069	Z	-0.16 0.07	-3.25 0.01	. . .	S	0.02	-19.24	0.712	A
1.09	75.69 1.70	All	Y	G	2.7	Y	H	F	3.3	2121	Z	-0.07 0.07	-3.07 0.02	-3.16 0.01	S	0.02	-19.17	0.712	A
0.95	73.34 1.56	All	Y	G	2.7	Y	W_H	F	3.3	2159	Z	. . .	-3.26 0.02	-3.24 0.01	S	0.02	-19.24	0.712	A
0.95	73.52 1.56	All	Y	G	2.7	Y	W_H	F	3.3	2160	Z	-0.11 0.07	-3.26 0.02	-3.24 0.01	S	0.01	-19.24	0.713	A
0.95	75.20 1.69	All	Y	G	2.7	Y	W_H	F	3.3	2160	Z	-0.06 0.07	-3.26 0.02	-3.24 0.01	M	0.02	-19.12	0.698	A
0.96	74.59 1.58	All	Y	G	2.7	N	W_H	F	3.3	2295	Z	-0.14 0.07	-3.21 0.02	-3.25 0.01	S	0.02	-19.21	0.712	A
0.95	73.63 1.61	All	Y	G	2.7	Y	W_H	F	3.3	2160	B	-0.07 0.09	-3.26 0.02	-3.24 0.01	S	0.02	-19.23	0.712	A
0.95	73.76 1.63	All	Y	G	2.7	Y	W_H	F	3.3	2160	Z	-0.11 0.07	-3.26 0.02	-3.24 0.01	S	0.02	-19.24	0.715	S
0.95	74.62 1.72	All	Y	G	2.7	Y	W_H	F	3.3	2160	Z	-0.06 0.07	-3.26 0.02	-3.24 0.01	M	0.02	-19.12	0.695	S
0.95	73.42 1.68	All	Y	G	2.7	Y	W_H	F	3.3	2160	Z	-0.11 0.07	-3.26 0.02	-3.24 0.01	S	0.01	-19.24	0.713	L
0.95	74.05 1.72	All	Y	G	2.7	Y	W_H	F	3.3	2160	Z	-0.11 0.07	-3.26 0.02	-3.24 0.01	S	0.02	-19.24	0.716	L
0.94	**73.02 1.62**	NML	Y	1	2.7	Y	W_H	F	3.3	2157	Z	-0.13 0.07	-3.26 0.02	-3.24 0.01	S	0.02	-19.25	0.712	A
0.95	73.14 1.63	NML	Y	G	2.7	Y	W_H	F	3.3	2159	Z	-0.11 0.07	-3.26 0.02	-3.24 0.01	S	0.02	-19.25	0.712	A
0.90	72.56 1.59	NML	Y	I	2.7	Y	W_H	F	3.3	2159	Z	-0.09 0.07	-3.31 0.02	-3.21 0.01	S	0.02	-19.27	0.712	A
1.31	73.40 1.90	NML	Y	G	No	Y	W_H	F	3.3	2223	Z	-0.08 0.08	-3.26 0.02	-3.23 0.02	S	0.02	-19.24	0.712	A
1.12	73.36 1.76	NML	Y	G	3.5	Y	W_H	F	3.3	2199	Z	-0.13 0.07	-3.25 0.02	-3.24 0.01	S	0.02	-19.24	0.712	A
1.11	73.33 1.76	NML	Y	1	3.5	Y	W_H	F	3.3	2198	Z	-0.13 0.07	-3.25 0.02	-3.24 0.01	S	0.02	-19.24	0.712	A
0.95	72.46 1.62	NML	Y	I	3.5	Y	W_H	F	3.3	2198	Z	-0.08 0.07	-3.30 0.02	-3.22 0.01	S	0.02	-19.27	0.712	A
1.13	73.08 1.76	NML	Y	G	3.5	Y	W_H	F	2.5	2200	Z	-0.13 0.07	-3.25 0.02	-3.24 0.01	S	0.02	-19.25	0.712	A
0.94	73.18 1.62	NML	Y	G	2.7	Y	W_H	C	3.3	2158	Z	-0.12 0.07	-3.27 0.02	-3.26 0.01	S	0.02	-19.25	0.712	A
0.97	73.38 1.64	NML	Y	G	2.7	Y	W_H	N	3.3	2158	Z	-0.10 0.07	-3.24 0.02	-3.23 0.01	S	0.02	-19.24	0.712	A
0.95	73.25 1.61	NML	N	G	2.7	Y	W_H	F	3.3	2160	Z	-0.11 0.07	-3.25 0.01	. . .	S	0.02	-19.25	0.712	A
1.19	71.45 1.87	NML	10	G	2.7	Y	W_H	F	3.3	1182	Z	-0.17 0.08	-3.26 0.03	. . .	S	0.02	-19.30	0.712	A
0.93	73.05 1.61	NML	60	G	2.7	Y	W_H	F	3.3	2068	Z	-0.16 0.07	-3.25 0.01	. . .	S	0.02	-19.25	0.712	A
1.08	74.95 1.77	NML	Y	G	2.7	Y	H	F	3.3	2120	Z	-0.08 0.07	-3.07 0.02	-3.16 0.01	S	0.02	-19.20	0.712	A
0.95	73.19 1.62	NML	Y	G	2.7	Y	W_H	F	3.3	2158	Z	. . .	-3.26 0.02	-3.24 0.01	S	0.02	-19.25	0.712	A
0.95	73.31 1.62	NML	Y	G	2.7	Y	W_H	F	3.3	2159	Z	-0.11 0.07	-3.26 0.02	-3.24 0.01	S	0.01	-19.25	0.713	A
0.95	75.01 1.76	NML	Y	G	2.7	Y	W_H	F	3.3	2159	Z	-0.07 0.07	-3.26 0.02	-3.24 0.01	M	0.02	-19.12	0.698	A
0.96	74.32 1.65	NML	Y	G	2.7	N	W_H	F	3.3	2294	Z	-0.14 0.07	-3.21 0.02	-3.25 0.01	S	0.02	-19.21	0.712	A
0.95	73.45 1.66	NML	Y	G	2.7	Y	W_H	F	3.3	2159	B	-0.08 0.10	-3.26 0.02	-3.24 0.01	S	0.02	-19.24	0.712	A
0.95	73.54 1.69	NML	Y	G	2.7	Y	W_H	F	3.3	2159	Z	-0.11 0.07	-3.26 0.02	-3.24 0.01	S	0.02	-19.25	0.715	S
0.95	74.43 1.78	NML	Y	G	2.7	Y	W_H	F	3.3	2159	Z	-0.07 0.07	-3.26 0.02	-3.24 0.01	M	0.02	-19.12	0.695	S
0.95	73.21 1.74	NML	Y	G	2.7	Y	W_H	F	3.3	2159	Z	-0.11 0.07	-3.26 0.02	-3.24 0.01	S	0.01	-19.25	0.713	L

Table 8—Continued

χ^2_{dof}	H_0	Anc	Brk	Clp	σ	Opt	PL	R	R_V	N	Z	γ	b	bl	SN	z_m	M_V^0	a_v	Gal
0.95	73.83 1.78	NML	Y	G	2.7	Y	W_H	F	3.3	2159	Z	-0.11 0.07	-3.26 0.02	-3.24 0.01	S	0.02	-19.25	0.716	L
0.94	73.85 1.77	NM	Y	1	2.7	Y	W_H	F	3.3	2156	Z	-0.16 0.07	-3.26 0.02	-3.24 0.01	S	0.02	-19.23	0.712	A
0.95	73.93 1.78	NM	Y	G	2.7	Y	W_H	F	3.3	2158	Z	-0.14 0.07	-3.26 0.02	-3.24 0.01	S	0.02	-19.23	0.712	A
0.90	73.55 1.75	NM	Y	I	2.7	Y	W_H	F	3.3	2158	Z	-0.13 0.08	-3.31 0.02	-3.21 0.01	S	0.02	-19.24	0.712	A
1.31	74.10 2.08	NM	Y	G	No	Y	W_H	F	3.3	2222	Z	-0.11 0.08	-3.26 0.02	-3.23 0.02	S	0.02	-19.22	0.712	A
1.12	74.21 1.93	NM	Y	G	3.5	Y	W_H	F	3.3	2198	Z	-0.16 0.08	-3.25 0.02	-3.24 0.01	S	0.02	-19.22	0.712	A
1.11	74.17 1.92	NM	Y	1	3.5	Y	W_H	F	3.3	2197	Z	-0.16 0.08	-3.25 0.02	-3.24 0.01	S	0.02	-19.22	0.712	A
0.95	73.40 1.78	NM	Y	I	3.5	Y	W_H	F	3.3	2197	Z	-0.11 0.08	-3.30 0.02	-3.22 0.01	S	0.02	-19.24	0.712	A
1.13	73.98 1.93	NM	Y	G	3.5	Y	W_H	F	2.5	2199	Z	-0.16 0.08	-3.25 0.02	-3.24 0.01	S	0.02	-19.22	0.712	A
0.94	73.94 1.77	NM	Y	G	2.7	Y	W_H	C	3.3	2157	Z	-0.15 0.07	-3.27 0.02	-3.26 0.01	S	0.02	-19.22	0.712	A
0.97	74.16 1.80	NM	Y	G	2.7	Y	W_H	N	3.3	2158	Z	-0.13 0.07	-3.24 0.02	-3.23 0.01	S	0.02	-19.22	0.712	A
0.95	74.04 1.76	NM	N	G	2.7	Y	W_H	F	3.3	2159	Z	-0.14 0.07	-3.25 0.01	. . .	S	0.02	-19.22	0.712	A
1.19	71.24 2.24	NM	10	G	2.7	Y	W_H	F	3.3	1181	Z	-0.17 0.08	-3.26 0.03	. . .	S	0.02	-19.31	0.712	A
0.93	74.00 1.76	NM	60	G	2.7	Y	W_H	F	3.3	2068	Z	-0.23 0.08	-3.25 0.01	. . .	S	0.02	-19.22	0.712	A
1.08	75.84 1.93	NM	Y	G	2.7	Y	H	F	3.3	2118	Z	-0.11 0.07	-3.07 0.02	-3.16 0.01	S	0.02	-19.17	0.712	A
0.95	73.61 1.76	NM	Y	G	2.7	Y	W_H	F	3.3	2157	Z	. . .	-3.26 0.02	-3.24 0.01	S	0.02	-19.23	0.712	A
0.95	74.09 1.78	NM	Y	G	2.7	Y	W_H	F	3.3	2158	Z	-0.14 0.07	-3.26 0.02	-3.24 0.01	S	0.01	-19.23	0.713	A
0.95	75.66 1.90	NM	Y	G	2.7	Y	W_H	F	3.3	2158	Z	-0.09 0.07	-3.26 0.02	-3.24 0.01	M	0.02	-19.11	0.698	A
0.95	75.14 1.80	NM	Y	G	2.7	N	W_H	F	3.3	2292	Z	-0.17 0.07	-3.21 0.02	-3.25 0.01	S	0.02	-19.19	0.712	A
0.95	74.45 1.87	NM	Y	G	2.7	Y	W_H	F	3.3	2158	B	-0.15 0.10	-3.26 0.02	-3.24 0.01	S	0.02	-19.21	0.712	A
0.95	74.33 1.84	NM	Y	G	2.7	Y	W_H	F	3.3	2158	Z	-0.14 0.07	-3.26 0.02	-3.24 0.01	S	0.02	-19.23	0.715	S
0.95	75.08 1.93	NM	Y	G	2.7	Y	W_H	F	3.3	2158	Z	-0.09 0.07	-3.26 0.02	-3.24 0.01	M	0.02	-19.11	0.695	S
0.95	73.99 1.89	NM	Y	G	2.7	Y	W_H	F	3.3	2158	Z	-0.14 0.07	-3.26 0.02	-3.24 0.01	S	0.01	-19.23	0.713	L
0.95	74.62 1.93	NM	Y	G	2.7	Y	W_H	F	3.3	2158	Z	-0.14 0.07	-3.26 0.02	-3.24 0.01	S	0.02	-19.23	0.716	L
0.94	71.56 1.71	NL	Y	1	2.7	Y	W_H	F	3.3	2157	Z	-0.18 0.07	-3.26 0.02	-3.24 0.01	S	0.02	-19.30	0.712	A
0.95	71.77 1.72	NL	Y	G	2.7	Y	W_H	F	3.3	2159	Z	-0.15 0.07	-3.25 0.02	-3.24 0.01	S	0.02	-19.29	0.712	A
0.89	71.49 1.69	NL	Y	I	2.7	Y	W_H	F	3.3	2159	Z	-0.12 0.08	-3.31 0.02	-3.21 0.01	S	0.02	-19.30	0.712	A
1.31	72.09 2.02	NL	Y	G	No	Y	W_H	F	3.3	2223	Z	-0.12 0.08	-3.25 0.02	-3.23 0.02	S	0.02	-19.28	0.712	A
1.12	71.93 1.87	NL	Y	G	3.5	Y	W_H	F	3.3	2199	Z	-0.17 0.08	-3.25 0.02	-3.24 0.01	S	0.02	-19.28	0.712	A
1.11	71.90 1.86	NL	Y	1	3.5	Y	W_H	F	3.3	2198	Z	-0.17 0.08	-3.25 0.02	-3.24 0.01	S	0.02	-19.29	0.712	A
0.94	71.38 1.73	NL	Y	I	3.5	Y	W_H	F	3.3	2198	Z	-0.11 0.07	-3.29 0.02	-3.22 0.01	S	0.02	-19.30	0.712	A
1.12	71.71 1.87	NL	Y	G	3.5	Y	W_H	F	2.5	2200	Z	-0.17 0.08	-3.24 0.02	-3.24 0.01	S	0.02	-19.29	0.712	A
0.94	71.75 1.71	NL	Y	G	2.7	Y	W_H	C	3.3	2159	Z	-0.17 0.07	-3.27 0.02	-3.26 0.01	S	0.02	-19.29	0.712	A
0.97	72.01 1.74	NL	Y	G	2.7	Y	W_H	N	3.3	2159	Z	-0.14 0.07	-3.23 0.02	-3.23 0.01	S	0.02	-19.28	0.712	A
0.95	71.83 1.71	NL	N	G	2.7	Y	W_H	F	3.3	2160	Z	-0.15 0.07	-3.25 0.01	. . .	S	0.02	-19.29	0.712	A
1.19	71.07 1.91	NL	10	G	2.7	Y	W_H	F	3.3	1182	Z	-0.18 0.08	-3.26 0.03	. . .	S	0.02	-19.31	0.712	A
0.93	71.30 1.70	NL	60	G	2.7	Y	W_H	F	3.3	2070	Z	-0.26 0.08	-3.25 0.01	. . .	S	0.02	-19.30	0.712	A
1.08	73.66 1.87	NL	Y	G	2.7	Y	H	F	3.3	2120	Z	-0.12 0.07	-3.06 0.02	-3.16 0.01	S	0.02	-19.23	0.712	A
0.94	72.17 1.72	NL	Y	G	2.7	Y	W_H	F	3.3	2158	Z	. . .	-3.26 0.02	-3.24 0.01	S	0.02	-19.28	0.712	A
0.95	71.93 1.72	NL	Y	G	2.7	Y	W_H	F	3.3	2159	Z	-0.15 0.07	-3.25 0.02	-3.24 0.01	S	0.01	-19.29	0.713	A
0.95	73.63 1.85	NL	Y	G	2.7	Y	W_H	F	3.3	2160	Z	-0.12 0.07	-3.26 0.02	-3.24 0.01	M	0.02	-19.16	0.698	A
0.95	72.58 1.73	NL	Y	G	2.7	N	W_H	F	3.3	2293	Z	-0.20 0.07	-3.21 0.02	-3.25 0.01	S	0.02	-19.27	0.712	A
0.95	72.16 1.72	NL	Y	G	2.7	Y	W_H	F	3.3	2159	B	-0.22 0.11	-3.25 0.02	-3.24 0.01	S	0.02	-19.28	0.712	A
0.95	72.16 1.78	NL	Y	G	2.7	Y	W_H	F	3.3	2159	Z	-0.15 0.07	-3.25 0.02	-3.24 0.01	S	0.02	-19.29	0.715	S
0.95	73.06 1.87	NL	Y	G	2.7	Y	W_H	F	3.3	2160	Z	-0.12 0.07	-3.26 0.02	-3.24 0.01	M	0.02	-19.16	0.695	S
0.95	71.83 1.83	NL	Y	G	2.7	Y	W_H	F	3.3	2159	Z	-0.15 0.07	-3.25 0.02	-3.24 0.01	S	0.01	-19.29	0.713	L

Table 8—Continued

χ^2_{dof}	H_0	Anc	Brk	Clp	σ	Opt	PL	R	R_V	N	Z	γ	b	bl	SN	z_m	M_V^0	a_v	Gal
0.95	72.44 1.87	NL	Y	G	2.7	Y	W_H	F	3.3	2159	Z	-0.15 0.07	-3.25 0.02	-3.24 0.01	S	0.02	-19.29	0.716	L
0.94	74.05 1.85	M+L	Y	1	2.7	Y	W_H	F	3.3	2156	Z	-0.13 0.07	-3.26 0.02	-3.24 0.01	S	0.02	-19.22	0.712	A
0.95	74.11 1.86	M+L	Y	G	2.7	Y	W_H	F	3.3	2158	Z	-0.11 0.07	-3.26 0.02	-3.24 0.01	S	0.02	-19.22	0.712	A
0.90	72.72 1.78	M+L	Y	I	2.7	Y	W_H	F	3.3	2158	Z	-0.08 0.07	-3.31 0.02	-3.21 0.01	S	0.02	-19.26	0.712	A
1.31	74.39 2.18	M+L	Y	G	No	Y	W_H	F	3.3	2222	Z	-0.08 0.08	-3.26 0.02	-3.23 0.02	S	0.02	-19.21	0.712	A
1.12	74.30 2.02	M+L	Y	G	3.5	Y	W_H	F	3.3	2198	Z	-0.13 0.07	-3.25 0.02	-3.24 0.01	S	0.02	-19.21	0.712	A
1.11	74.28 2.01	M+L	Y	1	3.5	Y	W_H	F	3.3	2197	Z	-0.13 0.07	-3.25 0.02	-3.24 0.01	S	0.02	-19.22	0.712	A
0.95	72.77 1.83	M+L	Y	I	3.5	Y	W_H	F	3.3	2197	Z	-0.07 0.07	-3.30 0.02	-3.22 0.01	S	0.02	-19.26	0.712	A
1.13	73.85 2.01	M+L	Y	G	3.5	Y	W_H	F	2.5	2199	Z	-0.13 0.07	-3.25 0.02	-3.24 0.01	S	0.02	-19.23	0.712	A
0.93	74.31 1.85	M+L	Y	G	2.7	Y	W_H	C	3.3	2156	Z	-0.10 0.07	-3.27 0.02	-3.26 0.01	S	0.02	-19.21	0.712	A
0.96	74.30 1.88	M+L	Y	G	2.7	Y	W_H	N	3.3	2156	Z	-0.09 0.07	-3.24 0.02	-3.23 0.01	S	0.02	-19.21	0.712	A
0.95	74.23 1.85	M+L	N	G	2.7	Y	W_H	F	3.3	2159	Z	-0.11 0.07	-3.25 0.01	. . .	S	0.02	-19.22	0.712	A
1.19	72.45 2.25	M+L	10	G	2.7	Y	W_H	F	3.3	1181	Z	-0.16 0.08	-3.26 0.03	. . .	S	0.02	-19.27	0.712	A
0.92	74.20 1.83	M+L	60	G	2.7	Y	W_H	F	3.3	2066	Z	-0.15 0.07	-3.24 0.01	. . .	S	0.02	-19.22	0.712	A
1.09	76.03 2.03	M+L	Y	G	2.7	Y	H	F	3.3	2120	Z	-0.08 0.07	-3.06 0.02	-3.16 0.01	S	0.02	-19.16	0.712	A
0.94	74.26 1.86	M+L	Y	G	2.7	Y	W_H	F	3.3	2156	Z	. . .	-3.26 0.02	-3.24 0.01	S	0.02	-19.22	0.712	A
0.95	74.28 1.86	M+L	Y	G	2.7	Y	W_H	F	3.3	2158	Z	-0.11 0.07	-3.26 0.02	-3.24 0.01	S	0.01	-19.22	0.713	A
0.95	76.03 1.99	M+L	Y	G	2.7	Y	W_H	F	3.3	2158	Z	-0.06 0.07	-3.26 0.02	-3.24 0.01	M	0.02	-19.10	0.698	A
0.95	75.58 1.89	M+L	Y	G	2.7	N	W_H	F	3.3	2292	Z	-0.13 0.07	-3.21 0.02	-3.25 0.01	S	0.02	-19.18	0.712	A
0.95	74.68 1.92	M+L	Y	G	2.7	Y	W_H	F	3.3	2159	B	-0.10 0.10	-3.26 0.02	-3.24 0.01	S	0.02	-19.20	0.712	A
0.95	74.52 1.92	M+L	Y	G	2.7	Y	W_H	F	3.3	2158	Z	-0.11 0.07	-3.26 0.02	-3.24 0.01	S	0.02	-19.22	0.715	S
0.95	75.45 2.01	M+L	Y	G	2.7	Y	W_H	F	3.3	2158	Z	-0.06 0.07	-3.26 0.02	-3.24 0.01	M	0.02	-19.10	0.695	S
0.95	74.18 1.97	M+L	Y	G	2.7	Y	W_H	F	3.3	2158	Z	-0.11 0.07	-3.26 0.02	-3.24 0.01	S	0.01	-19.22	0.713	L
0.95	74.81 2.01	M+L	Y	G	2.7	Y	W_H	F	3.3	2158	Z	-0.11 0.07	-3.26 0.02	-3.24 0.01	S	0.02	-19.22	0.716	L
1.09	72.39 2.41	N	Y	1	2.7	Y	W_H	F	3.3	1366	Z	-0.19 0.08	-3.11 0.03	-3.43 0.05	S	0.02	-19.27	0.712	A
1.09	72.55 2.42	N	Y	G	2.7	Y	W_H	F	3.3	1366	Z	-0.13 0.08	-3.10 0.03	-3.43 0.05	S	0.02	-19.27	0.712	A
0.93	73.19 2.45	N	Y	I	2.7	Y	W_H	F	3.3	1366	Z	-0.14 0.08	-3.22 0.03	-3.39 0.05	S	0.02	-19.25	0.712	A
1.56	72.76 2.60	N	Y	G	No	Y	W_H	F	3.3	1419	Z	-0.13 0.09	-3.12 0.04	-3.44 0.06	S	0.02	-19.26	0.712	A
1.31	72.93 2.51	N	Y	G	3.5	Y	W_H	F	3.3	1400	Z	-0.18 0.08	-3.09 0.03	-3.45 0.06	S	0.02	-19.25	0.712	A
1.29	72.95 2.51	N	Y	1	3.5	Y	W_H	F	3.3	1398	Z	-0.19 0.08	-3.09 0.03	-3.45 0.06	S	0.02	-19.25	0.712	A
1.01	72.95 2.47	N	Y	I	3.5	Y	W_H	F	3.3	1398	Z	-0.13 0.08	-3.19 0.03	-3.40 0.05	S	0.02	-19.25	0.712	A
1.30	73.05 2.52	N	Y	G	3.5	Y	W_H	F	2.5	1400	Z	-0.18 0.08	-3.09 0.03	-3.45 0.06	S	0.02	-19.25	0.712	A
1.10	72.35 2.41	N	Y	G	2.7	Y	W_H	C	3.3	1365	Z	-0.16 0.08	-3.12 0.03	-3.42 0.05	S	0.02	-19.27	0.712	A
1.09	72.66 2.42	N	Y	G	2.7	Y	W_H	N	3.3	1366	Z	-0.14 0.08	-3.09 0.03	-3.43 0.05	S	0.02	-19.26	0.712	A
1.10	71.62 2.38	N	N	G	2.7	Y	W_H	F	3.3	1366	Z	-0.15 0.08	-3.22 0.02	. . .	S	0.02	-19.29	0.712	A
1.18	70.83 2.41	N	10	G	2.7	Y	W_H	F	3.3	1065	Z	-0.15 0.08	-3.12 0.04	. . .	S	0.02	-19.32	0.712	A
1.09	71.07 2.38	N	60	G	2.7	Y	W_H	F	3.3	1278	Z	-0.26 0.08	-3.24 0.02	. . .	S	0.02	-19.31	0.712	A
1.15	74.69 2.48	N	Y	G	2.7	Y	H	F	3.3	1351	Z	-0.12 0.07	-2.90 0.03	-3.12 0.05	S	0.02	-19.20	0.712	A
1.10	72.40 2.41	N	Y	G	2.7	Y	W_H	F	3.3	1367	Z	. . .	-3.10 0.03	-3.43 0.05	S	0.02	-19.27	0.712	A
1.09	72.72 2.42	N	Y	G	2.7	Y	W_H	F	3.3	1366	Z	-0.13 0.08	-3.10 0.03	-3.43 0.05	S	0.01	-19.27	0.713	A
1.11	74.41 2.55	N	Y	G	2.7	Y	W_H	F	3.3	1368	Z	-0.12 0.08	-3.11 0.03	-3.43 0.05	M	0.02	-19.14	0.698	A
1.09	72.84 2.41	N	Y	G	2.7	N	W_H	F	3.3	1504	Z	-0.17 0.07	-3.05 0.03	-3.44 0.05	S	0.02	-19.26	0.712	A
1.09	72.55 2.42	N	Y	G	2.7	Y	W_H	F	3.3	1366	B	-0.20 0.12	-3.10 0.03	-3.43 0.05	S	0.02	-19.27	0.712	A
1.09	72.95 2.47	N	Y	G	2.7	Y	W_H	F	3.3	1366	Z	-0.13 0.08	-3.10 0.03	-3.43 0.05	S	0.02	-19.27	0.715	S
1.11	73.84 2.56	N	Y	G	2.7	Y	W_H	F	3.3	1368	Z	-0.12 0.08	-3.11 0.03	-3.43 0.05	M	0.02	-19.14	0.695	S
1.09	72.62 2.50	N	Y	G	2.7	Y	W_H	F	3.3	1366	Z	-0.13 0.08	-3.10 0.03	-3.43 0.05	S	0.01	-19.27	0.713	L

Table 8—Continued

χ^2_{dof}	H_0	Anc	Brk	Clp	σ	Opt	PL	R	R_V	N	Z	γ	b	bl	SN	z_m	M_V^0	a_v	Gal
1.09	73.24 2.54	N	Y	G	2.7	Y	W_H	F	3.3	1366	Z	-0.13 0.08	-3.10 0.03	-3.43 0.05	S	0.02	-19.27	0.716	L
0.94	76.09 2.20	M	Y	1	2.7	Y	W_H	F	3.3	2155	Z	-0.18 0.07	-3.26 0.02	-3.24 0.01	S	0.02	-19.16	0.712	A
0.95	75.97 2.21	M	Y	G	2.7	Y	W_H	F	3.3	2157	Z	-0.15 0.07	-3.25 0.02	-3.24 0.01	S	0.02	-19.17	0.712	A
0.90	74.48 2.11	M	Y	I	2.7	Y	W_H	F	3.3	2157	Z	-0.13 0.08	-3.31 0.02	-3.21 0.01	S	0.02	-19.21	0.712	A
1.31	76.17 2.59	M	Y	G	No	Y	W_H	F	3.3	2221	Z	-0.11 0.08	-3.25 0.02	-3.23 0.02	S	0.02	-19.16	0.712	A
1.12	76.30 2.40	M	Y	G	3.5	Y	W_H	F	3.3	2197	Z	-0.17 0.08	-3.25 0.02	-3.24 0.01	S	0.02	-19.16	0.712	A
1.11	76.27 2.39	M	Y	1	3.5	Y	W_H	F	3.3	2196	Z	-0.17 0.08	-3.25 0.02	-3.24 0.01	S	0.02	-19.16	0.712	A
0.95	74.50 2.17	M	Y	I	3.5	Y	W_H	F	3.3	2196	Z	-0.11 0.08	-3.29 0.02	-3.22 0.01	S	0.02	-19.21	0.712	A
1.13	75.80 2.40	M	Y	G	3.5	Y	W_H	F	2.5	2198	Z	-0.17 0.08	-3.24 0.02	-3.24 0.01	S	0.02	-19.17	0.712	A
0.94	76.14 2.20	M	Y	G	2.7	Y	W_H	C	3.3	2157	Z	-0.16 0.07	-3.27 0.02	-3.26 0.01	S	0.02	-19.16	0.712	A
0.96	76.20 2.23	M	Y	G	2.7	Y	W_H	N	3.3	2156	Z	-0.14 0.07	-3.23 0.02	-3.23 0.01	S	0.02	-19.16	0.712	A
0.95	76.09 2.19	M	N	G	2.7	Y	W_H	F	3.3	2158	Z	-0.15 0.07	-3.25 0.01	. . .	S	0.02	-19.16	0.712	A
1.19	74.24 3.82	M	10	G	2.7	Y	W_H	F	3.3	1180	Z	-0.17 0.08	-3.26 0.03	. . .	S	0.02	-19.22	0.712	A
0.93	76.31 2.19	M	60	G	2.7	Y	W_H	F	3.3	2067	Z	-0.26 0.08	-3.25 0.01	. . .	S	0.02	-19.16	0.712	A
1.08	78.10 2.42	M	Y	G	2.7	Y	H	F	3.3	2118	Z	-0.12 0.07	-3.06 0.02	-3.16 0.01	S	0.02	-19.11	0.712	A
0.95	75.52 2.18	M	Y	G	2.7	Y	W_H	F	3.3	2157	Z	. . .	-3.26 0.02	-3.24 0.01	S	0.02	-19.18	0.712	A
0.95	76.14 2.21	M	Y	G	2.7	Y	W_H	F	3.3	2157	Z	-0.15 0.07	-3.25 0.02	-3.24 0.01	S	0.01	-19.17	0.713	A
0.95	77.75 2.34	M	Y	G	2.7	Y	W_H	F	3.3	2157	Z	-0.10 0.07	-3.26 0.02	-3.24 0.01	M	0.02	-19.05	0.698	A
0.95	77.67 2.25	M	Y	G	2.7	N	W_H	F	3.3	2290	Z	-0.18 0.07	-3.21 0.02	-3.25 0.01	S	0.02	-19.12	0.712	A
0.95	77.70 2.48	M	Y	G	2.7	Y	W_H	F	3.3	2157	B	-0.23 0.11	-3.25 0.02	-3.24 0.01	S	0.02	-19.12	0.712	A
0.95	76.39 2.26	M	Y	G	2.7	Y	W_H	F	3.3	2157	Z	-0.15 0.07	-3.25 0.02	-3.24 0.01	S	0.02	-19.17	0.715	S
0.95	77.15 2.35	M	Y	G	2.7	Y	W_H	F	3.3	2157	Z	-0.10 0.07	-3.26 0.02	-3.24 0.01	M	0.02	-19.05	0.695	S
0.95	76.04 2.30	M	Y	G	2.7	Y	W_H	F	3.3	2157	Z	-0.15 0.07	-3.25 0.02	-3.24 0.01	S	0.01	-19.17	0.713	L
0.95	76.69 2.34	M	Y	G	2.7	Y	W_H	F	3.3	2157	Z	-0.15 0.07	-3.25 0.02	-3.24 0.01	S	0.02	-19.17	0.716	L
0.94	71.93 2.58	L	Y	1	2.7	Y	W_H	F	3.3	2156	Z	-0.18 0.07	-3.26 0.02	-3.24 0.01	S	0.02	-19.28	0.712	A
0.95	72.11 2.60	L	Y	G	2.7	Y	W_H	F	3.3	2158	Z	-0.15 0.07	-3.25 0.02	-3.24 0.01	S	0.02	-19.28	0.712	A
0.89	70.88 2.52	L	Y	I	2.7	Y	W_H	F	3.3	2158	Z	-0.13 0.08	-3.31 0.02	-3.21 0.01	S	0.02	-19.32	0.712	A
1.31	72.49 2.91	L	Y	G	No	Y	W_H	F	3.3	2222	Z	-0.12 0.08	-3.25 0.02	-3.23 0.02	S	0.02	-19.27	0.712	A
1.12	72.18 2.75	L	Y	G	3.5	Y	W_H	F	3.3	2198	Z	-0.17 0.08	-3.25 0.02	-3.24 0.01	S	0.02	-19.28	0.712	A
1.11	72.15 2.74	L	Y	1	3.5	Y	W_H	F	3.3	2197	Z	-0.17 0.08	-3.25 0.02	-3.24 0.01	S	0.02	-19.28	0.712	A
0.94	70.95 2.56	L	Y	I	3.5	Y	W_H	F	3.3	2197	Z	-0.12 0.08	-3.29 0.02	-3.22 0.01	S	0.02	-19.31	0.712	A
1.12	71.73 2.74	L	Y	G	3.5	Y	W_H	F	2.5	2199	Z	-0.17 0.08	-3.24 0.02	-3.24 0.01	S	0.02	-19.29	0.712	A
0.93	72.24 2.59	L	Y	G	2.7	Y	W_H	C	3.3	2157	Z	-0.16 0.07	-3.27 0.02	-3.26 0.01	S	0.02	-19.28	0.712	A
0.96	72.28 2.62	L	Y	G	2.7	Y	W_H	N	3.3	2157	Z	-0.14 0.07	-3.23 0.02	-3.23 0.01	S	0.02	-19.27	0.712	A
0.95	72.19 2.60	L	N	G	2.7	Y	W_H	F	3.3	2159	Z	-0.15 0.07	-3.25 0.01	. . .	S	0.02	-19.28	0.712	A
1.19	71.91 2.81	L	10	G	2.7	Y	W_H	F	3.3	1181	Z	-0.17 0.08	-3.26 0.03	. . .	S	0.02	-19.29	0.712	A
0.92	71.61 2.56	L	60	G	2.7	Y	W_H	F	3.3	2067	Z	-0.26 0.08	-3.24 0.01	. . .	S	0.02	-19.29	0.712	A
1.08	73.99 2.78	L	Y	G	2.7	Y	H	F	3.3	2119	Z	-0.12 0.07	-3.06 0.02	-3.16 0.01	S	0.02	-19.22	0.712	A
0.94	72.95 2.60	L	Y	G	2.7	Y	W_H	F	3.3	2157	Z	. . .	-3.26 0.02	-3.24 0.01	S	0.02	-19.25	0.712	A
0.95	72.27 2.60	L	Y	G	2.7	Y	W_H	F	3.3	2158	Z	-0.15 0.07	-3.25 0.02	-3.24 0.01	S	0.01	-19.28	0.713	A
0.95	74.05 2.72	L	Y	G	2.7	Y	W_H	F	3.3	2159	Z	-0.12 0.07	-3.26 0.02	-3.24 0.01	M	0.02	-19.15	0.698	A
0.95	73.29 2.63	L	Y	G	2.7	N	W_H	F	3.3	2292	Z	-0.20 0.07	-3.21 0.02	-3.25 0.01	S	0.02	-19.24	0.712	A
0.95	72.77 2.59	L	Y	G	2.7	Y	W_H	F	3.3	2158	B	-0.22 0.11	-3.25 0.02	-3.24 0.01	S	0.02	-19.26	0.712	A
0.95	72.50 2.65	L	Y	G	2.7	Y	W_H	F	3.3	2158	Z	-0.15 0.07	-3.25 0.02	-3.24 0.01	S	0.02	-19.28	0.715	S
0.95	73.48 2.73	L	Y	G	2.7	Y	W_H	F	3.3	2159	Z	-0.12 0.07	-3.26 0.02	-3.24 0.01	M	0.02	-19.15	0.695	S
0.95	72.17 2.67	L	Y	G	2.7	Y	W_H	F	3.3	2158	Z	-0.15 0.07	-3.25 0.02	-3.24 0.01	S	0.01	-19.28	0.713	L

Table 8—Continued

χ^2_{dof}	H_0	Anc	Brk	Clp	σ	Opt	PL	R	R_V	N	Z	γ	b	bl	SN	z_m	M_V^0	a_v	Gal
0.95	72.79 2.71	L	Y	G	2.7	Y	W_H	F	3.3	2158	Z	-0.15 0.07	-3.25 0.02	-3.24 0.01	S	0.02	-19.28	0.716	L
0.94	74.45 2.92	A	Y	1	2.7	Y	W_H	F	3.3	2156	Z	-0.18 0.07	-3.26 0.02	-3.24 0.01	S	0.02	-19.21	0.712	A
0.95	74.42 2.93	A	Y	G	2.7	Y	W_H	F	3.3	2159	Z	-0.15 0.07	-3.25 0.02	-3.25 0.01	S	0.02	-19.21	0.712	A
0.89	72.88 2.79	A	Y	I	2.7	Y	W_H	F	3.3	2159	Z	-0.13 0.08	-3.31 0.02	-3.21 0.01	S	0.02	-19.26	0.712	A
1.31	74.36 3.43	A	Y	G	No	Y	W_H	F	3.3	2222	Z	-0.11 0.08	-3.25 0.02	-3.23 0.02	S	0.02	-19.21	0.712	A
1.12	74.56 3.18	A	Y	G	3.5	Y	W_H	F	3.3	2198	Z	-0.17 0.08	-3.25 0.02	-3.24 0.01	S	0.02	-19.21	0.712	A
1.11	74.50 3.17	A	Y	1	3.5	Y	W_H	F	3.3	2197	Z	-0.17 0.08	-3.25 0.02	-3.24 0.01	S	0.02	-19.21	0.712	A
0.94	72.86 2.87	A	Y	I	3.5	Y	W_H	F	3.3	2197	Z	-0.11 0.08	-3.29 0.02	-3.22 0.01	S	0.02	-19.26	0.712	A
1.12	73.24 3.14	A	Y	G	3.5	Y	W_H	F	2.5	2199	Z	-0.17 0.08	-3.24 0.02	-3.24 0.01	S	0.02	-19.25	0.712	A
0.93	77.45 3.03	A	Y	G	2.7	Y	W_H	C	3.3	2157	Z	-0.16 0.07	-3.27 0.02	-3.26 0.01	S	0.02	-19.12	0.712	A
0.97	71.72 2.85	A	Y	G	2.7	Y	W_H	N	3.3	2158	Z	-0.14 0.07	-3.24 0.02	-3.23 0.01	S	0.02	-19.29	0.712	A
0.95	74.47 2.92	A	N	G	2.7	Y	W_H	F	3.3	2159	Z	-0.15 0.07	-3.25 0.01	. . .	S	0.02	-19.21	0.712	A
1.19	74.23 3.29	A	10	G	2.7	Y	W_H	F	3.3	1181	Z	-0.17 0.08	-3.26 0.03	. . .	S	0.02	-19.22	0.712	A
0.92	74.85 2.90	A	60	G	2.7	Y	W_H	F	3.3	2066	Z	-0.26 0.08	-3.24 0.01	. . .	S	0.02	-19.20	0.712	A
1.08	79.78 3.35	A	Y	G	2.7	Y	H	F	3.3	2119	Z	-0.12 0.07	-3.06 0.02	-3.16 0.01	S	0.02	-19.06	0.712	A
0.94	73.88 2.89	A	Y	G	2.7	Y	W_H	F	3.3	2156	Z	. . .	-3.25 0.02	-3.24 0.01	S	0.02	-19.23	0.712	A
0.95	74.59 2.94	A	Y	G	2.7	Y	W_H	F	3.3	2159	Z	-0.15 0.07	-3.25 0.02	-3.25 0.01	S	0.01	-19.21	0.713	A
0.95	76.08 3.05	A	Y	G	2.7	Y	W_H	F	3.3	2158	Z	-0.10 0.07	-3.26 0.02	-3.24 0.01	M	0.02	-19.09	0.698	A
0.95	75.97 2.98	A	Y	G	2.7	N	W_H	F	3.3	2291	Z	-0.18 0.07	-3.21 0.02	-3.25 0.01	S	0.02	-19.17	0.712	A
0.95	76.15 3.17	A	Y	G	2.7	Y	W_H	F	3.3	2160	B	-0.24 0.11	-3.25 0.02	-3.25 0.01	S	0.02	-19.16	0.712	A
0.95	74.83 2.98	A	Y	G	2.7	Y	W_H	F	3.3	2159	Z	-0.15 0.07	-3.25 0.02	-3.25 0.01	S	0.02	-19.21	0.715	S
0.95	75.50 3.05	A	Y	G	2.7	Y	W_H	F	3.3	2158	Z	-0.10 0.07	-3.26 0.02	-3.24 0.01	M	0.02	-19.09	0.695	S
0.95	74.49 3.00	A	Y	G	2.7	Y	W_H	F	3.3	2159	Z	-0.15 0.07	-3.25 0.02	-3.25 0.01	S	0.01	-19.21	0.713	L
0.95	75.12 3.05	A	Y	G	2.7	Y	W_H	F	3.3	2159	Z	-0.15 0.07	-3.25 0.02	-3.25 0.01	S	0.02	-19.21	0.716	L
0.91	71.30 1.47	All	Y	1	2.7	Y	W_I	F	3.3	2709	Z	-0.27 0.05	-3.20 0.02	-3.38 0.02	S	0.02	-19.30	0.712	A
0.90	71.19 1.53	NML	Y	1	2.7	Y	W_I	F	3.3	2707	Z	-0.27 0.05	-3.19 0.02	-3.38 0.02	S	0.02	-19.31	0.712	A
1.12	71.98 2.26	N	Y	1	2.7	Y	W_I	F	3.3	1930	Z	-0.29 0.06	-3.11 0.02	-4.08 0.05	S	0.02	-19.28	0.712	A

Note. — Anc: Anchors used, N=N4258 Masers, M=MW Parallaxes, L=LMC DEBs, NML is the primary fit from all three, All=NML+M31 DEBs, Brk: Break in P–L, Clp: G is global, I is individual, 1 is global one-by-one; σ is the clipping threshold, Opt: optical completeness is required, PL: Wesenheit magnitude, R: reddening law, F99, CCM or Nataf, N: Number of Cepheids fit, γ: change in Wesenheit mag per dex log[O/H], b:slope of P–Lor with break $P > 10$ days, bl: slope of P–Lat $P < 10$ days, SN: salt or MLCS2k2, z_m minimum z for Hubble diagram where 0.02 is 0.0233, a_x: intercept, Gal: A=All, S=Spiral, L=high LSF

REFERENCES

Addison, G. E., Huang, Y., Watts, D. J., et al. 2015, ArXiv e-prints, arXiv:1511.00055

Argon, A. L., Greenhill, L. J., Reid, M. J., Moran, J. M., & Humphreys, E. M. L. 2007, ApJ, 659, 1040

Aubourg, É., Bailey, S., Bautista, J. E., et al. 2015, Phys. Rev. D, 92, 123516

Becker, M. R., Desmond, H., Rozo, E., Marshall, P., & Rykoff, E. S. 2015, ArXiv e-prints, arXiv:1507.07523

Benedict, G. F., McArthur, B. E., Feast, M. W., et al. 2007, AJ, 133, 1810

Bennett, C. L., Larson, D., Weiland, J. L., & Hinshaw, G. 2014, ApJ, 794, 135

Bennett, C. L., Larson, D., Weiland, J. L., et al. 2013, ApJS, 208, 20

Betoule, M., Kessler, R., Guy, J., et al. 2014, A&A, 568, A22

Bhardwaj, A., Kanbur, S. M., Macri, L. M., et al. 2016, ArXiv e-prints, arXiv:1601.00953

Birrer, S., Amara, A., & Refregier, A. 2015, ArXiv e-prints, arXiv:1511.03662

Bonamente, M., Joy, M. K., LaRoque, S. J., et al. 2006, ApJ, 647, 25

Bonanos, A. Z., & Stanek, K. Z. 2003, ApJ, 591, L111

Bresolin, F. 2011, ApJ, 729, 56

Calabrese, E., Hlozek, R. A., Battaglia, N., et al. 2013, Phys. Rev. D, 87, 103012

Cardelli, J. A., Clayton, G. C., & Mathis, J. S. 1989, ApJ, 345, 245

Casertano, S., Anderson, A. G. R. J., Anderson, R. I., et al. 2015, ArXiv e-prints, arXiv:1512.09371

Cuesta, A. J., Verde, L., Riess, A., & Jimenez, R. 2015, MNRAS, 448, 3463

Dalcanton, J. J., Williams, B. F., Lang, D., et al. 2012, ApJS, 200, 18

Darling, J. 2011, ApJ, 732, L2

Di Benedetto, G. P. 2005, MNRAS, 357, 174

Dvorkin, C., Wyman, M., Rudd, D. H., & Hu, W. 2014, Phys. Rev. D, 90, 083503

Efstathiou, G. 2014, MNRAS, 440, 1138

Ferrarese, L., Silbermann, N. A., Mould, J. R., et al. 2000, PASP, 112, 177

Fitzpatrick, E. L. 1999, PASP, 111, 63

Fitzpatrick, E. L., Ribas, I., Guinan, E. F., et al. 2002, ApJ, 564, 260

Fitzpatrick, E. L., Ribas, I., Guinan, E. F., Maloney, F. P., & Claret, A. 2003, ApJ, 587, 685

Freedman, W. L., & Madore, B. F. 2010, ARA&A, 48, 673

Freedman, W. L., Madore, B. F., Scowcroft, V., et al. 2012, ApJ, 758, 24

Freedman, W. L., Madore, B. F., Gibson, B. K., et al. 2001, ApJ, 553, 47

Gao, F., Braatz, J. A., Reid, M. J., et al. 2016, ApJ, 817, 128

Guinan, E. F., Fitzpatrick, E. L., Dewarf, L. E., et al. 1998, ApJ, 509, L21

Guy, J., Astier, P., Nobili, S., Regnault, N., & Pain, R. 2005, A&A, 443, 781

Guy, J., Sullivan, M., Conley, A., et al. 2010, A&A, 523, A7

Hanson, R. B. 1979, MNRAS, 186, 875

Herrnstein, J. R., Moran, J. M., Greenhill, L. J., et al. 1999, Nature, 400, 539

Hicken, M., Wood-Vasey, W. M., Blondin, S., et al. 2009a, ApJ, 700, 1097

Hicken, M., Challis, P., Jha, S., et al. 2009b, ApJ, 700, 331

Hinshaw, G., Larson, D., Komatsu, E., et al. 2013, ApJS, 208, 19

Hu, W. 2005, in Astronomical Society of the Pacific Conference Series, Vol. 339, Observing Dark Energy, ed. S. C. Wolff & T. R. Lauer, 215

Humphreys, E. M. L., Argon, A. L., Greenhill, L. J., Moran, J. M., & Reid, M. J. 2005, in Astronomical Society of the Pacific Conference Series, Vol. 340, Future Directions in High Resolution Astronomy, ed. J. Romney & M. Reid, 466

Humphreys, E. M. L., Reid, M. J., Greenhill, L. J., Moran, J. M., & Argon, A. L. 2008, ApJ, 672, 800

Humphreys, E. M. L., Reid, M. J., Moran, J. M., Greenhill, L. J., & Argon, A. L. 2013, ApJ, 775, 13

Jha, S., Riess, A. G., & Kirshner, R. P. 2007, ApJ, 659, 122

Jones, D. O., Riess, A. G., & Scolnic, D. M. 2015, ApJ, 812, 31

Kaluzny, J. 1998, A&AS, 133, 25

Kelly, P. L., Hicken, M., Burke, D. L., Mandel, K. S., & Kirshner, R. P. 2010, ApJ, 715, 743

Kodric, M., Riffeser, A., Seitz, S., et al. 2015, ApJ, 799, 144

Laidler, V. 2005, "Synphot User's Guide", Version 5.0 (Baltimore: STScI)

Lampeitl, H., Smith, M., Nichol, R. C., et al. 2010, ApJ, 722, 566

Leavitt, H. S., & Pickering, E. C. 1912, Harvard College Observatory Circular, 173, 1

Leistedt, B., Peiris, H. V., & Verde, L. 2014, Physical Review Letters, 113, 041301

Livio, M., & Riess, A. G. 2013, Physics Today, 66, 41

Macri, L. M., Ngeow, C.-C., Kanbur, S. M., Mahzooni, S., & Smitka, M. T. 2015, AJ, 149, 117

Macri, L. M., Stanek, K. Z., Bersier, D., Greenhill, L. J., & Reid, M. J. 2006, ApJ, 652, 1133

Madore, B. F. 1982, ApJ, 253, 575

Madore, B. F., & Freedman, W. L. 1991, PASP, 103, 933

Mager, V. A., Madore, B. F., & Freedman, W. L. 2013, ApJ, 777, 79

Nataf, D. M., Gonzalez, O. A., Casagrande, L., et al. 2015, ArXiv e-prints, arXiv:1510.01321

Ngeow, C.-C., & Kanbur, S. M. 2005, MNRAS, 360, 1033

Odderskov, I., Koksbang, S. M., & Hannestad, S. 2016, J. Cosmology Astropart. Phys., 2, 001

Paczynski, B., & Sasselov, D. 1997, in Variables Stars and the Astrophysical Returns of the Microlensing Surveys, ed. R. Ferlet, J.-P. Maillard, & B. Raban, 309

Persson, S. E., Madore, B. F., Krzemiński, W., et al. 2004, AJ, 128, 2239

Pietrzyński, G., Graczyk, D., Gieren, W., et al. 2013, Nature, 495, 76

Pike, R. W., & Hudson, M. J. 2005, ApJ, 635, 11

Planck Collaboration, Ade, P. A. R., Aghanim, N., et al. 2014, A&A, 571, A16

—. 2015, ArXiv e-prints, arXiv:1502.01589

Ribas, I., Fitzpatrick, E. L., Maloney, F. P., Guinan, E. F., & Udalski, A. 2002, ApJ, 574, 771

Ribas, I., Jordi, C., Vilardell, F., et al. 2005, ApJ, 635, L37

Riess, A. G. 2010, First On-orbit Measurements of the WFC3-IR Count-rate Non-Linearity, Tech. rep., STScI

—. 2011, An Independent Determination of WFC3-IR Zeropoints and Count Rate Non-Linearity from 2MASS Asterisms, Tech. rep., STScI

Riess, A. G., Casertano, S., Anderson, J., MacKenty, J., & Filippenko, A. V. 2014, ApJ, 785, 161

Riess, A. G., Fliri, J., & Valls-Gabaud, D. 2012, ApJ, 745, 156

Riess, A. G., Li, W., Stetson, P. B., et al. 2005, ApJ, 627, 579

Riess, A. G., Strolger, L., Casertano, S., et al. 2007, ApJ, 659, 98

Riess, A. G., Macri, L., Casertano, S., et al. 2009a, ApJ, 699, 539

Riess, A. G., Macri, L., Li, W., et al. 2009b, ApJS, 183, 109

Riess, A. G., Macri, L., Casertano, S., et al. 2011, ApJ, 730, 119

Rigault, M., Copin, Y., Aldering, G., et al. 2013, A&A, 560, A66

Rigault, M., Aldering, G., Kowalski, M., et al. 2015, ApJ, 802, 20

Romaniello, M., Primas, F., Mottini, M., et al. 2008, A&A, 488, 731

Saha, A., Sandage, A., Labhardt, L., et al. 1996, ApJ, 466, 55

Sakai, S., Ferrarese, L., Kennicutt, Jr., R. C., & Saha, A. 2004, ApJ, 608, 42

Sandage, A., Tammann, G. A., Saha, A., et al. 2006, ApJ, 653, 843

Scolnic, D., & Kessler, R. 2016, ArXiv e-prints, arXiv:1603.01559

Scolnic, D., Rest, A., Riess, A., et al. 2014, ApJ, 795, 45

Scolnic, D., Casertano, S., Riess, A. G., et al. 2015, ArXiv e-prints, arXiv:1508.05361

Senchyna, P., Johnson, L. C., Dalcanton, J. J., et al. 2015, ApJ, 813, 31

Sorce, J. G., Tully, R. B., & Courtois, H. M. 2012, ApJ, 758, L12

Soszynski, I., Poleski, R., Udalski, A., et al. 2008, Acta Astron., 58, 163

Spergel, D. N., Flauger, R., & Hložek, R. 2015, Phys. Rev. D, 91, 023518

Stetson, P. B. 1987, PASP, 99, 191

—. 1996, PASP, 108, 851

Story, K. T., Reichardt, C. L., Hou, Z., et al. 2013, ApJ, 779, 86

Sullivan, M., Conley, A., Howell, D. A., et al. 2010, MNRAS, 406, 782

Suyu, S. H., Treu, T., Blandford, R. D., et al. 2012, ArXiv e-prints, arXiv:1202.4459

Suyu, S. H., Auger, M. W., Hilbert, S., et al. 2013, ApJ, 766, 70

van Leeuwen, F., Feast, M. W., Whitelock, P. A., & Laney, C. D. 2007, MNRAS, 379, 723

Vilardell, F., Ribas, I., Jordi, C., Fitzpatrick, E. L., & Guinan, E. F. 2010, A&A, 509, A70

Wagner-Kaiser, R., Sarajedini, A., Dalcanton, J. J., Williams, B. F., & Dolphin, A. 2015, MNRAS, 451, 724

Weinberg, S. 2013, Physical Review Letters, 110, 241301

Wyman, M., Rudd, D. H., Vanderveld, R. A., & Hu, W. 2014, Physical Review Letters, 112, 051302